

Controlling the Flow of Light Using High-Contrast Metastructures

Thesis by
Yu Horie

In Partial Fulfillment of the Requirements for the
Degree of
Doctor of Philosophy

The logo for the California Institute of Technology (Caltech), featuring the word "Caltech" in a bold, orange, sans-serif font.

CALIFORNIA INSTITUTE OF TECHNOLOGY
Pasadena, California

2018
Defended August 17, 2017

© 2018

Yu Horie

ORCID: 0000-0001-7083-1270

All rights reserved

To Chika and Kei.

ACKNOWLEDGEMENTS

First and foremost, I owe a tremendous debt of gratitude to my advisor, Prof. Andrei Faraon. I am sincerely grateful not only for the support, guidance, and encouragement, but also for the freedom he granted me to explore new ideas at the very beginning. Joining as a first generation student in his research group has been one of my greatest honors in my research career, through which I could gain a lot of knowledge about physics and photonics as well as hands-on experiences. I am also glad to have had the opportunity to serve as a teaching assistance in APh23/24, and I am grateful to Andrei for the breadth of this experience.

I would like to also express my sincere gratitude to all the members of my thesis committee, Professors Azita Emami, Ali Hajimiri, Kerry J. Vahala, and Changhuei Yang for their time and thoughtful advices. Thanks are also due to Professors Amnon Yariv and Hyuck Choo for serving on my candidacy exam committee.

The works presented in this thesis have been accompanied by numerous supports from all the people in the Faraon's group. Particularly, I am extremely grateful to Amir Arbabi. Amir has been a great mentor during my PhD, who has an encyclopaedic knowledge of optics, photonics, fabrication, and measurements. His insightful advice and genuine professional attitude throughout the past 4 years have shaped the way I engage myself in research, and have been very important to my PhD works as well as myself. None of the works in this thesis would have been possible without him. Ehsan Arbabi and Seyedeh Mahsa Kamali have both been instrumental in helping me to solve the issues in my devices and to develop simulation methods and fabrication recipes. The fruitful discussions we had in our sub-group meeting always gave me new insights in understanding the physics and developing new ideas. I also thank Evan Miyazono, Tian Zhong, and Jon Kindem for always answering my random questions very helpfully. I would like to also thank other group members in the group, Ioana Craiciu, Chuting Wang, Jake Rochman, Sadegh Faraji-Dana, John Bartholomew, Philip A. Camayd-Munoz, Conner Ballew, Hyounghan Kwon, and Jiaqi Li. Their progress always made me inspired and their helps I received in many ways made my life in the group much easier. I would especially like to express my gratitude towards Cecilia Gamboa for her tireless support.

I am also appreciative of the numerous supports I received from the technical staffs in Kavli Nanoscience Institute (KNI) at Caltech, especially Guy A. Derosé. I am

also grateful to Max Jones and William S. Fegadolli from Caltech Nanofabrication Group for their generous advice on nanofabrication techniques.

The collaboration with the researchers at Samsung Advanced Institute of Technology has been very fruitful. Especially, I am grateful to Seunghoon Han for his very collaborative and motivated attitude, which enabled our collaborative work on the visible color filters.

Regarding the work presented in Chapter 5 in this thesis, I would like to acknowledge Mooseok Jang and Atsushi Shibukawa, one of my closest collaborators on the disordered metasurface project. I also thank Professor Changhuei Yang for making this project possible as well as the opportunity to work with his brilliant students and postdocs, Yan Liu, Haowen Ruan, and Joshua Brake.

I also want to thank all my friends in the Caltech Japanese community as well as weekly tennis circle, Ryoji Shinya, Kiemi Shinya, Ryo Adachi, Koichiro Kajikawa, Saneyuki Ohno, Masakazu Hamada, Hidehiko Inagaki, Taisuke Imai, Shinsuke Suzuki, Yu Takahashi, Kazuki Maeda, Chuting Wang, Maiko Obana, Mooseok Jang, and Atsushi Shibukawa, who made me feel positive and relaxed in my graduate studies.

I'd also like acknowledge Professors Kazumi Wada and Yasuhiko Ishikawa, who were my advisors during the Master program at the University of Tokyo. They guided me into the field of photonics, and kindly advised and helped me to study abroad.

I'd like to thank my parents and family in Japan. Their unquestioning and generous supports have been crucial to the completion of this thesis. Last but not least, I thank my family, Chika Horie and Kei Horie, for their love and encouragement.

Yu Horie
Pasadena, California
August 17, 2017

Support

I would like to thank Japan Student Services Organization (JASSO) fellowship, which supported the entire 5 years of my graduate studies.

ABSTRACT

A new class of planar optical components and devices has emerged using subwavelength metastructures with a strong contrast in refractive indices. High-contrast metastructures have shown promises to manipulate optical fields in an extraordinary way and to replace conventional bulky optical elements by their low-profile analogs, typically with subwavelength-scale features. We elucidate the underlying principle, how these seemingly low-profile geometries render unique optical responses, using the coupled-mode analysis in a multimode waveguide. Moreover, strong field localization in high-index structures allows us to interpret each single element in the metastructures as a low-quality-factor resonator (or a localized scatterer), permitting us to realize designer surface that shapes phase, amplitude, and polarization of light in free space, also known as an optical metasurface. The remainder of the thesis is devoted to explore novel applications in optics using high-contrast metastructures. One of the particularly interesting applications is to use them in an optical resonator. Specifically, we demonstrate to incorporate high-contrast subwavelength grating reflectors and dielectric metasurfaces in a vertical Fabry–Perot cavity, and show that we can flexibly tune the resonance frequency by the subwavelength patterning. With this technique, we envision the realization of compact, on-chip spectrometers when integrating them on a photodetector array. Secondly, we investigate the use of high-contrast subwavelength gratings in visible wavelengths. We perform the optimization of their geometries and demonstrate a set of RGB color filters, down to near a micrometer in the pixel size. This platform exhibits unique performances such as high efficiency, angular insensitivity, and color tunability by the design. A novel device concept is also explored, where a high-contrast subwavelength grating reflector is integrated on a silicon platform to constitute an active resonant antenna, enabling high-speed, phase-dominant modulation by means of thermo-optic effect of silicon. We demonstrate an array of such active antennas, yielding a beam deflection capability. This justifies the robustness of our device design, enabling a large-scale integration of high-speed, phase-dominant spatial light modulators. Finally, we introduce a disorder-engineered metasurface in the context of wavefront shaping. Recently, wavefront shaping with disordered media has demonstrated optical manipulation capabilities beyond those of conventional optics, but translating this class of technology into a practical use has remained challenging due to enormous amounts of information needed to be characterized as the input-output responses.

As a paradigm shift, we propose the use of disorder-engineered metasurface in wavefront shaping, where the disorder is programmatically designed and makes the system characterization-free prior to use. With this approach, we demonstrate high numerical aperture focusing in an extended volume as well as wide-field fluorescence imaging with unprecedented performances.

Thesis supervisor:

- Andrei Faraon
Assistant Professor of Applied Physics and Materials Science

Thesis committee:

- Andrei Faraon (Chair)
Assistant Professor of Applied Physics and Materials Science
- Azita Emami
Andrew and Peggy Cherng Professor of Electrical Engineering and Medical Engineering
- Ali Hajimiri
Bren Professor of Electrical Engineering and Medical Engineering
- Kerry J. Vahala
Ted and Ginger Jenkins Professor of Information Science and Technology and Applied Physics
- Changhuei Yang
Thomas G. Myers Professor of Electrical Engineering, Bioengineering, and Medical Engineering

PUBLISHED CONTENT AND CONTRIBUTIONS

- [1] Y. Horie, A. Arbabi, S. Han, and A. Faraon, “High resolution on-chip optical filter array based on double subwavelength grating reflectors”, *Opt. Express* **23**, 29848–29854 (2015) DOI: [10.1364/OE.23.029848](https://doi.org/10.1364/OE.23.029848),
Y.H. participated in the conception of the project, fabricated and characterized the devices, gathered and analyzed the data, and wrote the manuscript.
- [2] Y. Horie, A. Arbabi, E. Arbabi, S. M. Kamali, and A. Faraon, “Wide bandwidth and high resolution planar filter array based on DBR-metasurface-DBR structures”, *Opt. Express* **24**, 11677–11682 (2016) DOI: [10.1364/OE.24.011677](https://doi.org/10.1364/OE.24.011677),
Y.H. participated in the conception of the project, fabricated and characterized the devices, gathered and analyzed the data, and wrote the manuscript.
- [3] Y. Horie*, S. Han*, J.-Y. Lee, J. Kim, Y. Kim, A. Arbabi, C. Shin, L. Shi, E. Arbabi, S. M. Kamali, H.-S. Lee, S. W. Hwang, and A. Faraon, “Visible wavelength color filters using dielectric subwavelength gratings for backside-illuminated CMOS image sensor technologies”, *Nano Lett.* **17**, 3159–3164 (2017) DOI: [10.1021/acs.nanolett.7b00636](https://doi.org/10.1021/acs.nanolett.7b00636),
**Y.H. and S.H. contributed equally to this work. Y.H. participated in the conception of the project, fabricated and characterized the devices, gathered and analyzed the data, and wrote the manuscript.*
- [4] Y. Horie, A. Arbabi, E. Arbabi, S. M. Kamali, and A. Faraon, “High-speed, phase-dominant spatial light modulation with silicon-based active resonant antennas”, (under submission),
Y.H. participated in the conception of the project, designed, fabricated and characterized the devices, gathered and analyzed the data, and wrote the manuscript.
- [5] M. Jang*, Y. Horie*, A. Shibukawa*, J. Brake, Y. Liu, S. M. Kamali, A. Arbabi, H. Ruan, A. Faraon, and C. Yang, “Complex wavefront engineering with disorder-engineered metasurfaces”, (2017), [arXiv:1706.08640](https://arxiv.org/abs/1706.08640), URL: <https://arxiv.org/abs/1706.08640>,
**M.J., Y.H. and A.S. contributed equally to this work. Y.H. participated in the conception of the project, developed the theoretical modeling, designed the experiments, and analyzed the experimental data, and participated in the writing of the manuscript.*

OTHER PUBLICATIONS

- [1] A. Arbabi, Y. Horie, A. J. Ball, M. Bagheri, and A. Faraon, “Subwavelength-thick lenses with high numerical apertures and large efficiency based on high contrast transmitarrays”, *Nat. Commun.* **6**, 7069 (2015) DOI: [10.1038/ncomms8069](https://doi.org/10.1038/ncomms8069).
- [2] A. Arbabi, Y. Horie, M. Bagheri, and A. Faraon, “Dielectric metasurfaces for complete control of phase and polarization with subwavelength spatial resolution and high transmission”, *Nat. Nanotechnol.* **10**, 937–943 (2015) DOI: [10.1038/nano.2015.186](https://doi.org/10.1038/nano.2015.186).
- [3] A. Arbabi, R. M. Briggs, Y. Horie, M. Bagheri, and A. Faraon, “Efficient dielectric metasurface collimating lenses for mid-infrared quantum cascade lasers”, *Opt. Express* **23**, 33310–33317 (2015) DOI: [10.1364/OE.23.033310](https://doi.org/10.1364/OE.23.033310).
- [4] S. M. Kamali, A. Arbabi, E. Arbabi, Y. Horie, and A. Faraon, “Decoupling optical function and geometrical form using conformal flexible dielectric metasurfaces”, *Nat. Commun.* **7**, 11618 (2016) DOI: [10.1038/ncomms11618](https://doi.org/10.1038/ncomms11618).
- [5] E. Arbabi, A. Arbabi, S. M. Kamali, Y. Horie, and A. Faraon, “Multiwavelength polarization-insensitive lenses based on dielectric metasurfaces with”, *Optica* **3**, 628–633 (2016) DOI: [10.1364/OPTICA.3.000628](https://doi.org/10.1364/OPTICA.3.000628).
- [6] E. Arbabi, A. Arbabi, S. M. Kamali, Y. Horie, and A. Faraon, “High efficiency double-wavelength dielectric metasurface lenses with dichroic birefringent meta-atoms”, *Opt. Express* **24**, 18468–18477 (2016) DOI: [10.1364/OE.24.018468](https://doi.org/10.1364/OE.24.018468).
- [7] E. Arbabi, A. Arbabi, S. M. Kamali, Y. Horie, and A. Faraon, “Multiwavelength metasurfaces through spatial multiplexing”, *Sci. Rep.* **6**, 32803 (2016) DOI: [10.1038/srep32803](https://doi.org/10.1038/srep32803).
- [8] S. M. Kamali, E. Arbabi, A. Arbabi, Y. Horie, and A. Faraon, “Highly tunable elastic dielectric metasurface lenses”, *Laser Photonics Rev.* **10**, 1002–1008 (2016) DOI: [10.1002/lpor.201600144](https://doi.org/10.1002/lpor.201600144).
- [9] A. Arbabi, E. Arbabi, S. M. Kamali, Y. Horie, S. Han, and A. Faraon, “Miniature optical planar camera based on a wide-angle metasurface doublet corrected for monochromatic aberrations”, *Nat. Commun.* **7**, 13682 (2016) DOI: [10.1038/ncomms13682](https://doi.org/10.1038/ncomms13682).
- [10] E. Arbabi, A. Arbabi, S. M. Kamali, Y. Horie, and A. Faraon, “Controlling the sign of chromatic dispersion in diffractive optics”, *Optica* **4**, 625–632 (2017) DOI: [10.1364/OPTICA.4.000625](https://doi.org/10.1364/OPTICA.4.000625).

- [11] A. Arbabi, E. Arbabi, Y. Horie, S. M. Kamali, and A. Faraon, “Planar metasurface retroreflector”, *Nat. Photon.* **11**, 415–420 (2017) DOI: [10.1038/nphoton.2017.96](https://doi.org/10.1038/nphoton.2017.96).
- [12] H. Emmer, C. T. Chen, R. Saive, D. Friedrich, Y. Horie, A. Arbabi, A. Faraon, and H. A. Atwater, “Fabrication of single crystal gallium phosphide thin films on glass”, *Sci. Rep.* **7**, 4643 (2017) DOI: [10.1038/s41598-017-05012-w](https://doi.org/10.1038/s41598-017-05012-w).

TABLE OF CONTENTS

Acknowledgements	iv
Abstract	vi
Published Content and Contributions	ix
Other Publications	x
Table of Contents	xii
List of Figures	xiv
Abbreviations	xvii
Chapter 1: Introduction	1
1.1 Introduction to High-Contrast Metastructures	1
1.2 Outline of the Thesis	11
Chapter 2: Planar Optical Bandpass Filter Array for On-chip Spectroscopy	12
2.1 Motivation	13
2.2 Planar Filter Array Using Double Subwavelength Grating Reflectors	17
2.3 Characterization of Double Grating band-pass Filters	20
2.4 Planar Filter Array Using DBR-Metasurface-DBR Structures	23
2.5 Fabrication and Characterization of DBR-Metasurface-DBR Band- pass Filters	25
2.6 Summary and Outlook	27
Chapter 3: Visible Wavelength Color Filters Using Silicon Subwave- length Metastructures	28
3.1 Motivation	28
3.2 Design of Visible Wavelength RGB Color Filters	30
3.3 Fabrication and Characterization of Visible Color Filters	32
3.4 Summary and Outlook	37

Chapter 4: High-Speed, Phase-Dominant Spatial Light Modulation with Silicon-Based Active Resonant Antennas	41
4.1 Motivation	41
4.2 Design of an Active Resonant Antenna	43
4.3 Phase-Dominant Modulation with a Single Antenna	48
4.4 Demonstration of Phased Array Beam Deflection	51
4.5 Discussion	53
4.6 Summary and Outlook	54
Chapter 5: Disorder-Engineered Metasurfaces for Wavefront Shaping . .	60
5.1 Background	60
5.2 Principles of Wavefront Shaping	63
5.3 Disorder-Engineered Metasurfaces	67
5.4 High-NA Optical Focusing over an Extended Volume	71
5.5 Wide FOV, High-Resolution Fluorescence Imaging	75
5.6 Summary and Outlook	77
5.A Degrees of Freedom in a Disordered Metasurface Assisted Wavefront Engineering System	79
5.B Conventional Measurement of the Transmission Matrix	82
5.C Immunofluorescence-Labeled Sample Preparation	83
Chapter 6: Conclusion	86
6.1 Summary of Accomplishments	86
6.2 Concluding Remarks	87
Bibliography	88
Appendix A: Fabrication	102
A.1 Lab Procedure	102
A.2 Optical Properties of Materials	104

LIST OF FIGURES

1.1	Generic 1-D grating problem.	2
1.2	Coupled Bloch mode analysis.	4
1.3	Multimode regime in zeroth-order reflectance map.	5
1.4	Example designs of high-contrast subwavelength gratings.	6
1.5	Magnetic energy density profile of high-contrast subwavelength gratings.	8
1.6	Reflective 1-D metasurface design.	9
1.7	Transmissive dielectric metasurface design.	10
2.1	Working principle of compact spectrometers using a wedge filter.	14
2.2	Schematic of bandpass filter array using double subwavelength grating reflectors.	15
2.3	Schematic of the proposed bandpass filter array using a dielectric metasurface.	16
2.4	Design of SWG reflectors.	17
2.5	Simulated transmission spectra of bandpass filter array.	19
2.6	Double subwavelength gratings fabrication.	21
2.7	Fabrication of double SWG reflectors.	22
2.8	Measured transmission spectra of a set of fabricated bandpass filters	22
2.9	Design of DBR-metasurface-DBR bandpass filter.	24
2.10	DBR-metasurface-DBR filter fabrication.	25
2.11	Experimental results of fabricated DBR-metasurface-DBR bandpass filters.	26
3.1	Schematic of visible wavelength on-chip color filters using dielectric subwavelength gratings.	30
3.2	Visible wavelength on-chip color filters using dielectric subwavelength gratings for BSI-CIS applications.	31
3.3	RGB visible color filter fabrication.	32
3.4	Measurement results of visible color filters.	34
3.5	Spectral responses for small pixel sizes of color filters.	35
3.6	Color transmission analysis using plane wave expansion.	36
3.7	RCWA simulations of the angular dependence of the transmission spectra.	38

3.8	RCWA simulations of the angular dependence of the transmission spectra under unpolarized light illumination.	38
3.9	Measured and simulated transmission spectra of each color filter under oblique illuminations.	39
3.10	Refractive index of poly-Si in the visible wavelength.	40
3.11	Measurement setups.	40
4.1	Concept of a phase-dominant spatial light modulator with silicon-based active resonant antennas.	42
4.2	Design of active resonant antenna using the temporal coupled-mode theory.	46
4.3	Graphical representation of the reflection coefficient in a resonator system with one port.	47
4.4	Characterization results of a single active antenna.	50
4.5	Experimental demonstration of phased array beam deflection.	52
4.6	Experimental setup to characterize an optical antenna as well as phased array.	55
4.7	Measured reflectivity spectra for different QWP angles in a cross-polarized setup.	56
4.8	Simulated response times in temperature modulation.	56
4.9	Simulated phased array beam deflection.	57
4.10	CAD layout of the phased array.	58
4.11	SEM images of the fabricated phased array.	59
5.1	Wavefront shaping assisted by a disorder-engineered metasurface.	62
5.2	Disorder-engineered metasurface.	69
5.3	Disordered metasurface fabrication.	70
5.4	Extraordinary stability of a disordered metasurface.	70
5.5	Experimental demonstration of diffraction-limited focusing over an extended volume.	71
5.6	Demonstration of ultra-high number of resolvable spots even with a handful of physically controlled degrees of freedom as inputs.	74
5.7	Demonstration of disordered metasurface assisted microscope.	76
5.8	Measured angular scattering profiles of disordered metasurfaces as well as those of conventional disordered media.	84
5.9	Experimental setup for wavefront shaping with a disordered metasurface.	85
A.1	SEM image of a subwavelength grating reflector.	103

A.2 SEM image of a silicon nitride disordered metasurface. 104

A.3 Measured refractive indices by ellipsometry. 105

ABBREVIATIONS

EMT	effective medium theory.
SWG	subwavelength grating.
RCWA	rigorous coupled-wave analysis.
VCSEL	vertical-cavity surface-emitting laser.
DBR	distributed Bragg reflector.
MEMS	microelectromechanical systems.
SiO₂	silicon dioxide.
<i>Q</i>-factor	quality factor.
LVF	linear variable filter.
α-Si	amorphous silicon.
SEM	scanning electron microscope.
PECVD	plasma-enhanced chemical vapor deposition.
ICP-RIE	inductively coupled plasma reactive ion etching.
SF₆	sulfur hexafluoride.
C₄F₈	octafluorocyclobutane.
Al₂O₃	aluminum oxide.
CMOS	complementary metal oxide transistor.
CIS	CMOS image sensor.
poly-Si	polycrystalline silicon.
BSI	backside-illumination.
YSNR	luminance signal-to-noise ratio.
LPCVD	low-pressure chemical vapor deposition.
PWE	plane wave expansion.
SLM	spatial light modulator.
LiDAR	light detection and ranging.
DMD	digital micro-mirror device.
SiN_x	silicon nitride.
PBS	polarizing beamsplitter.
HWP	half waveplate.
QWP	quarter waveplate.
FEM	finite element method.
TM	transmission matrix.
NA	numerical aperture.
FOV	field of view.

SNR	signal-to-noise ratio.
SVD	singular value decomposition.
NH₄OH	ammonium hydroxide.
H₂O₂	hydrogen peroxide.
TiO₂	titanium dioxide.
FWHM	full width at half maximum.
TIRF	total internal reflection fluorescence.
SAW	surface acoustic wave.
EBL	electron beam lithography.
H₂SO₄	sulfuric acid.
IPA	isopropyl alcohol.
DI water	deionized water.
MIBK	methyl isobutyl ketone.

INTRODUCTION

1.1 Introduction to High-Contrast Metastructures

High-contrast metastructures are a class of planar optical components, typically realized by patterning a single layer of high index material (usually the index contrast $\Delta n > 1$) with an appropriate subwavelength-scale features. In the last decade, they have received considerable interest in the field of optoelectronics and integrated optics [1–6] because they offer unique and unprecedented optical properties, such as broad transmission and reflection features with near unity efficiency [7–9] and the capability to shape the phase, amplitude, and polarization of light [10–16], just by a lithographically definable binary structure. The planar form factor and the potential for low-cost wafer-scale fabrication make them attractive for immediate adoption in consumer products. Also, high-contrast metastructures are promising for realizing complex optical systems with new functionalities when used as a new building block together with other components in integrated optics.

In this chapter, we start with the generic grating problem [17] and use the coupled Bloch mode analysis in a periodic structure to describe the unique optical properties of high-contrast metastructures with an emphasis on the fundamental differences from conventional diffraction gratings or the effective medium theory (EMT) [18–20]. Figure 1.1 defines the parameters of a grating, which will be used to facilitate the discussion. Without much loss of generality, we treat a 1-D grating, which has a periodicity of a in the x -direction and is translationally invariant in the y -direction. The surrounding medium is assumed to be air ($n = 1$) for the sake of simplicity. It is also assumed that a monochromatic plane wave with the wavelength of λ normally impinges on the structure from the $-z$ to the $+z$ -direction.

When the periodicity of the grating is greater than λ , an incident monochromatic plane wave is separated into multiple orders. This can be understood as a constructive interference of specific wavelengths of the light along specific directions. The angles of the diffracted orders, which solely depend on the periodicity of the grating and the wavelength of the light, are governed by the grating equation:

$$\sin \theta_m = \sin \theta_0 + \frac{m\lambda}{a}, \quad (1.1)$$

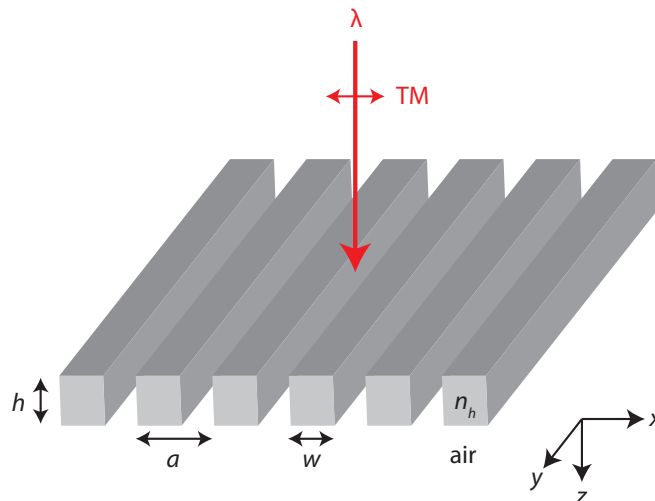


Figure 1.1: **Generic 1-D grating problem.** In this chapter, we deal with a 1-D grating with a periodicity of a , where the light is normally incident, the surrounding medium is air ($n = 1$), the refractive index of the grating is n_h , and w is the width of the grating.

where θ_m is the angle of the m -th order (m as an integer) and θ_0 is the incident angle. This class of structures is commonly used as a diffractive optical element, useful in efficiently dispersing different colors of incident light into different directions. Spectral control over the diffracted orders can be achieved by carefully designing the shape and refractive indices of the unit cell in the periodic structure; one of the most common technologies is an Échelette grating or blazed grating, in which the unit cell is optimized such that most of the power is concentrated in a specific order.

As in the condition of Fig. 1.1, we hereafter consider the case where the light is normally incident ($\theta_0 = 0$). When the periodicity of the grating is smaller than the wavelength of the light, which we call a subwavelength grating (SWG), the right-hand side of Eq. (1.1) becomes greater than one, and therefore there is no real solution for θ_m given any nonzero integer value of m . This indicates that the higher-order diffracted modes do not correspond to a free-space mode in reflection or transmission, but to a guided Bloch mode found in the periodic region. Here, Bloch mode refers to a mode in a waveguide array propagating in the z -direction by virtually extending the periodic region infinitely long in both $\pm z$ -directions. When there exists only a single propagative Bloch mode along the infinitely long grating, typically when $w < \lambda/2n_h$, the EMT provides a good approximation in understanding such periodic structures, allowing treatment of the grating region ($0 < z < h$) as a homogeneous

slab with an anisotropic effective index. This is also known as a deep-subwavelength regime. This regime is particularly useful when one would like to artificially create an anisotropic material with optical birefringence. It has been demonstrated that, by adjusting the height of the grating, the accumulated phases across the grating for the two orthogonal polarizations can be tuned to have a desired phase shift, resulting in the realization of waveplates [21].

There is an interesting regime between the aforementioned two regimes, where the subwavelength periodic structure supports more than one propagative Bloch mode, herein referred to as a “multimode” regime (also see references [1, 22–24]). This multimode nature sets it apart from the regime in the EMT, and most of the unique properties of high-contrast metastructures, such as near unity broad reflection/transmission as well as the capability to manipulate a wavefront by a nonperiodic structure appear in this regime, and can be understood by considering the coupling among those propagative Bloch modes as well as free-space modes (zeroth-order reflection and transmission). Strong index modulation in the periodic region makes such Bloch modes highly dispersive, resulting in pronounced spectral properties, which will be discussed later.

To find Bloch modes in a virtually extended infinite grating, we need to solve the wave equation. From the Maxwell’s equation, the vector potential $\mathbf{A}(\mathbf{r})$ is governed by the following wave equation in a source-free, nonuniform dielectric medium [25, 26]:

$$\nabla^2 \mathbf{A} + \omega^2 \mu_0 \varepsilon \mathbf{A} = 0, \quad (1.2)$$

where ω is the optical frequency, $\varepsilon(\mathbf{r})$ is the dielectric constant, and μ_0 is the magnetic permeability in a vacuum. The relationship between the vector potential $\mathbf{A}(\mathbf{r})$ and scalar potential $\Phi(\mathbf{r})$ is given by

$$\nabla \cdot \mathbf{A} + j\omega \mu_0 \varepsilon \Phi = 0. \quad (1.3)$$

The electric and magnetic fields are given by

$$\mathbf{E} = -j\omega \mathbf{A} - \nabla \Phi \quad (1.4)$$

$$\mu_0 \mathbf{H} = \nabla \times \mathbf{A}. \quad (1.5)$$

Given an axially uniform medium, such as an infinitely long periodic grating in our case, we can write the solution for \mathbf{A} with a particular polarization,

$$\mathbf{A} = \hat{x}u(x)e^{-\beta z}, \quad (1.6)$$

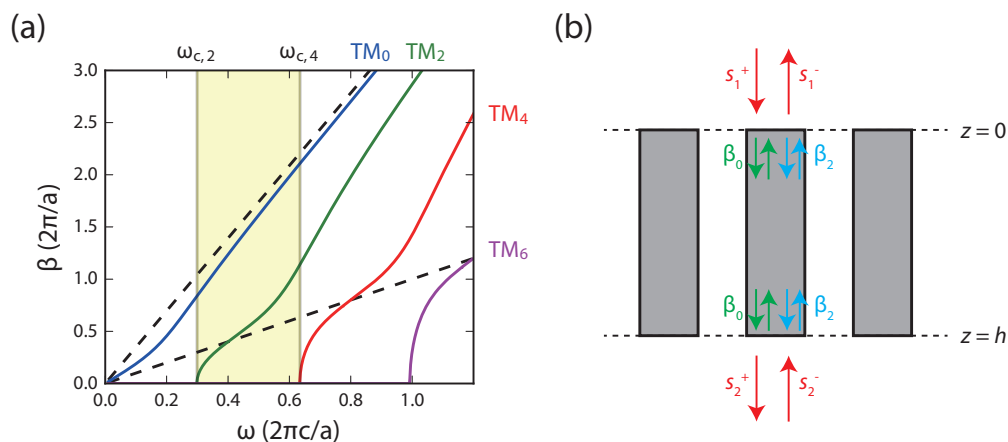


Figure 1.2: **Coupled Bloch mode analysis.** (a) ω - β dispersion diagram of 1-D grating with $n_h = 3.48$ and $w/a = 0.75$. (b) Coupled Bloch modes β_0 and β_2 , propagate along the z -direction with two ports s_1^\pm and s_2^\pm .

where β is the propagation constant and we used the assumption that ε is spatially invariant along the y -axis. The spatial dependence factor $u(x)$ can be derived from Eq. (1.1), by solving the differential equation:

$$\left[\frac{\partial^2}{\partial x^2} + \omega^2 \mu_0 \varepsilon(x) \right] u(x) = \beta^2 u(x). \quad (1.7)$$

Because the dielectric constant is periodic in the x -direction, the spatial dependence $u(x)$ is also periodic. Given ω and $\varepsilon(x)$, we can numerically solve for the eigenfunctions $u_n(x)$ and the corresponding eigenvalues β_n , where n indicates the index of the mode ($n = 0, 1, 2, \dots$). The numerical results of the ω - β dispersion diagram are plotted in Fig. 1.2(a), when $n_h = 3.48$ and $w/a = 0.75$. The yellow-shaded region in Fig. 1.2(a) is the regime of interest, where two propagative Bloch modes can exist in the grating region. It should be noted that we are now interested only in the even symmetric modes (TM_0, TM_2, TM_4, \dots), which can be excited by a normally incident plane wave. The odd symmetric modes (TM_1, TM_3, TM_5, \dots) are orthogonal to the normally incident plane wave, thus cannot be excited. In these situations, it is physically meaningful to interpret the subwavelength system as coupled Bloch modes (β_0 and β_2) with two ports for the input and output waves (s_1^\pm and s_2^\pm) [25, 27] as illustrated in Fig. 1.2(b). Although the set of the Bloch modes is orthogonal, they can be coupled to each other at the interface of $z = 0$ and $z = h$, whereas only the DC components of the coupled Bloch modes can be leaked out into free space as zeroth-order reflection and transmission. In the picture of coupled Bloch modes,

one can completely describe the system by relating the coefficients of the modes using the scattering matrix, for which the coupling coefficients can be numerically calculated by the rigorous coupled-wave analysis (RCWA) technique [28].

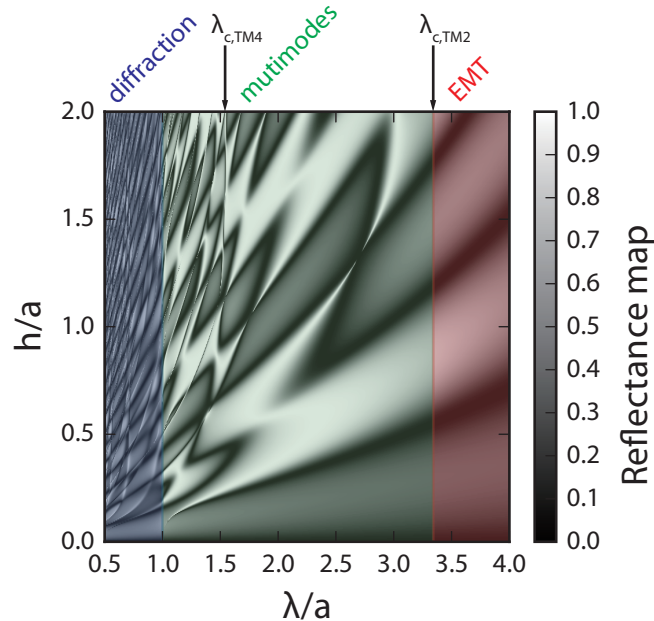


Figure 1.3: **Multimode regime in zeroth-order reflectance map.** The blue-shaded region corresponds to the diffraction grating regime ($\lambda < a$). The red-shaded region corresponds to the EMT regime, in which the grating behaves as a homogeneous slab with an effective index. The green-shaded region corresponds to the “multimode” regime, in which a few propagative Bloch modes can exist.

High-Contrast Subwavelength Gratings

Figure 1.3 shows the RCWA-calculated zeroth-order reflectance for the 1-D grating with $n_h = 3.48$ and $w/a = 0.75$ as a function of wavelength and height of the grating, both normalized by the periodicity. The blue-shaded region in the shorter wavelength side corresponds to the diffraction grating regime ($\lambda < a$). The red-shaded region at longer wavelength corresponds to the EMT regime, in which the periodic modulation of the reflectance is seen, validating the approximation that the structure behaves as a homogeneous slab with an effective index. In the multimode regime, denoted with the green shade, where the grating has a few propagative Bloch modes, albeit inhibiting the high-order diffractions, we can observe a checkerboard-like pattern in the reflectance map, which originates from the couplings among the few Bloch modes in the grating and free-space modes. To further highlight the unique features of high-

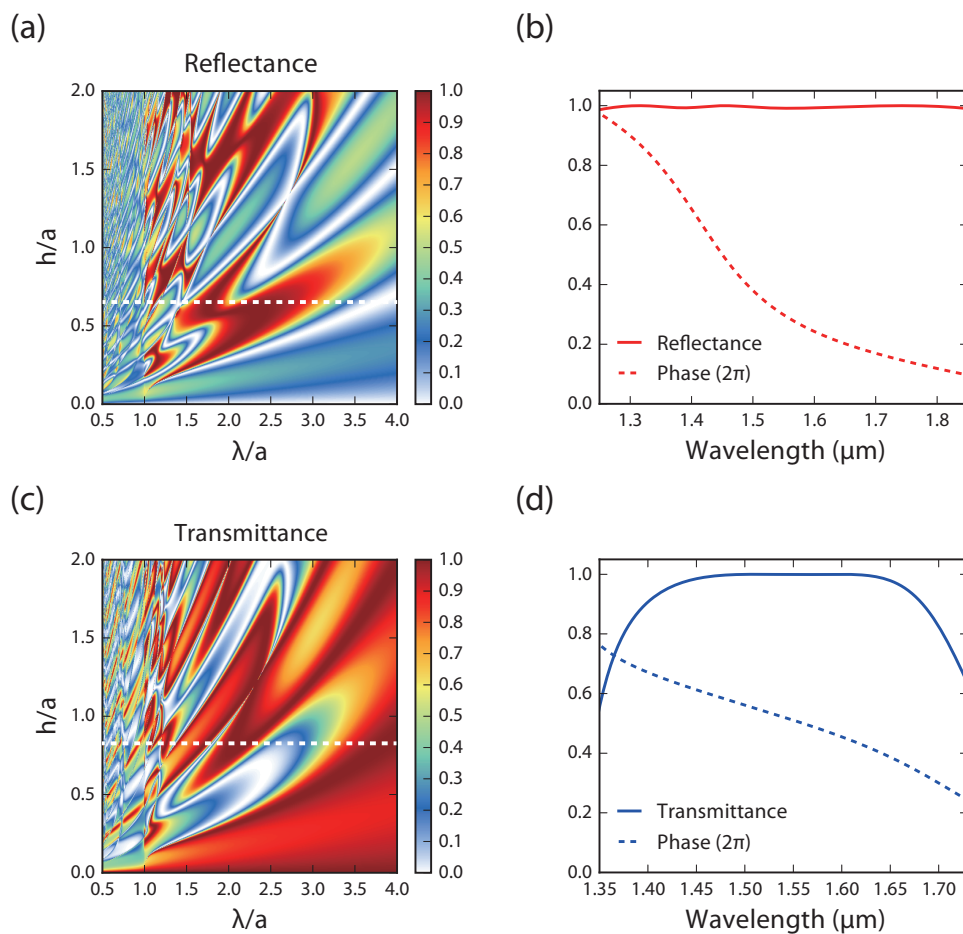


Figure 1.4: **Examples designs of high-contrast SWGs.** (a) Zeroth-order reflectance map for a 1-D grating with $n_h = 3.48$ and $w/a = 0.75$. (b) Broadband, highly reflective design of high-contrast SWG with $a = 0.74 \mu\text{m}$, $h = 0.435 \mu\text{m}$, and $w = 0.555 \mu\text{m}$. (c) Zeroth-order reflectance map for a 1-D grating with $n_h = 3.48$ and $w/a = 0.55$. (d) Broadband, highly transmissive design of high-contrast SWG with $a = 0.74 \mu\text{m}$, $h = 0.6 \mu\text{m}$, and $w = 0.4 \mu\text{m}$.

contrast SWGs, two of the optimized designs for the near unity reflection/transmission in broadband are plotted in Fig. 1.4, showing broadband high reflectivity $R_0 > 0.99$ for $\Delta\lambda/\lambda \sim 39\%$ as well as high transmittance $T_0 > 0.99$ for $\Delta\lambda/\lambda \sim 13\%$. These designs were found by choosing the right height in Fig. 1.4(a,c). These unusual phenomena can be well understood by the above-discussed coupled Bloch modes. Each of the Bloch modes has a different propagation constant β_n , which describes the accumulated phase when they propagate along the z -direction. As they reach the output port $z = h$, the energy transmission to the zeroth order for $z > h$ can

be calculated by the field overlap integral at the interface. Because the allowed free-space mode for $z > h$ has only a DC coefficient, minimizing the DC component of the total field composed of the propagated Bloch modes leads to minimizing the zeroth-order transmission, thus zeroth-order reflection is maximized. One can even find a condition where unit reflectivity is realized by the complete cancellation of the DC component. In addition to this, we can also find that the dispersion curve for the few Bloch modes are roughly parallel, as in Fig. 1.2(a), indicating that the high-reflectivity condition is preserved to some extent when the wavelength of interest is perturbed. Likewise, in the case of high transmission, one can find a condition that zeroth-order reflection is suppressed, and thus realize near unit transmission, as in Fig. 1.4(d). Despite the relatively simple structure, this behavior was first discovered by Mateus *et al.* [7] only in the last decades. Subsequently, high-contrast SWG reflectors have been adopted in vertical-cavity surface-emitting laser (VCSEL) technology to replace one of the distributed Bragg reflectors (DBRs) [29] and in novel microelectromechanical systems (MEMS) devices [30–35]. The broad reflection feature of the high-contrast SWGs can sometimes perform as well as DBRs with > 30 dielectric stacks. As an additional benefit, these structures provide new functionalities, such as polarization control.

Optical Metasurfaces

The high-contrast SWGs provide us another optical manipulation capability when used in nonperiodic fashion. Figure 1.5 shows the magnetic energy density distribution found by the RCWA technique when the structures are optimized to have near unit reflection and transmission. The high-index contrast results in negligible interactions between the grating bars as we can see that the magnetic energy density is concentrated in high-index regions, denoted with dashed lines. In these situations, it can be set apart from the periodic picture where the optical field is infinitely extended along the x -direction, to a different perspective, in which each of high-index blocks behaves as a localized resonator and reflection and transmission can be considered as collective scatterings from an array of resonators. Another important observation in Fig. 1.4(b,d) is that the phases of the reflected and transmitted field rapidly vary across the spectra with near constant amplitudes. Using the scaling properties of Maxwell's equations [36], this property can be qualitatively translated to a reflection response, where local resonators with scaled size reflect with near unity amplitude with a significant change in phase as a function of the structural parameter, for example, period or width of the grating. This concept is quantitatively

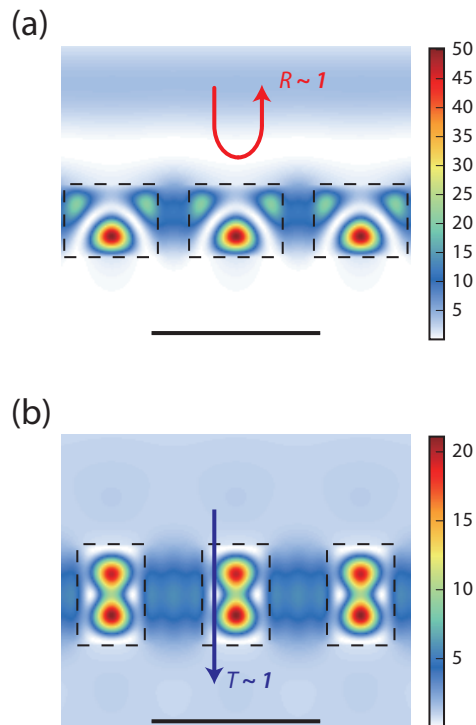


Figure 1.5: **Magnetic energy density profile of high-contrast SWGs.** (a) Highly reflective design the same as Fig. 1.4(b) at $\lambda = 1.55 \mu\text{m}$. (b) Highly transmissive design the same as Fig. 1.4(d) at $\lambda = 1.55 \mu\text{m}$. The magnetic energy density of one is normally incident onto the SWGs from the top. The dashed lines depict the boundaries of the high-index SWGs with $n_h = 3.48$. Scale bar: $1 \mu\text{m}$.

confirmed by the numerical simulation using the RCWA technique, shown in Fig. 1.6. Figure. 1.6(b) can be used as a look-up table to design a reflective metasurface, with which one can create a spatially varying phase profile by locally modifying the period and width of the SWG, as experimentally confirmed by Fattal *et al.* [11].

More ubiquitous classes of optical metasurfaces can be realized by high-index nanoposts acting as a scatterer on a periodic 2-D lattice (Fig. 1.7(a)). With the same concept discussed above, we can find a family of periodic structures that provide large transmission amplitudes, while their phases span the entire 0 to 2π range, just by modifying the diameter of the nanoposts, as shown in Fig. 1.7(b). This design is particularly interesting to implement a desired phase profile $\phi(x, y)$. The local scattering effect is more prominent than in 1-D high-contrast SWGs, as indicated by the magnetic energy density profile in Fig. 1.7(c). This highly localized scattering allows us to implement any arbitrary wavefront manipulation as high as $1/\lambda$ in terms

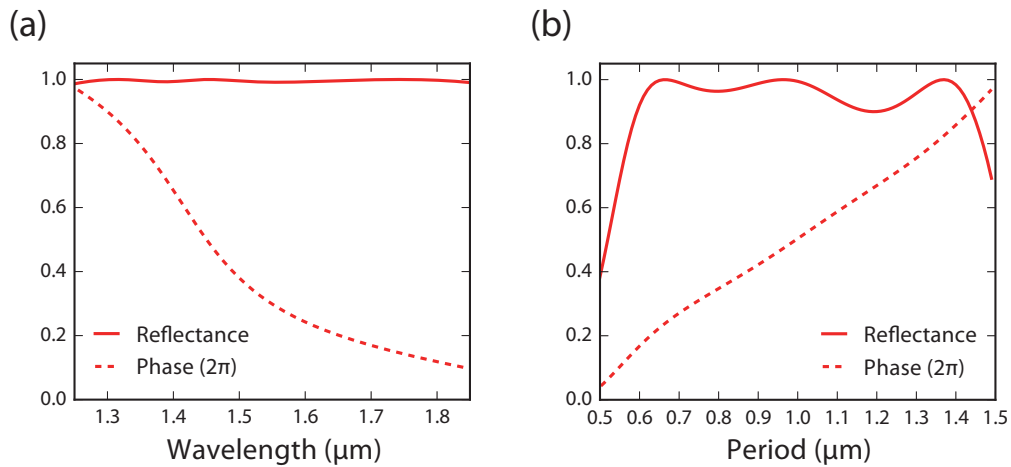


Figure 1.6: **Reflective 1-D metasurface design.** (a) Reflectance spectrum with an SWG design the same as Fig. 1.4(b) at $\lambda = 1.55 \mu\text{m}$. (b) Reflectance spectrum as well as phase as a function of the grating period with $w/a = 0.5$ and $h = 0.465 \mu\text{m}$ at $\lambda = 1.55 \mu\text{m}$.

of spatial frequency. With this class of optical metasurface, we have shown high numerical aperture (as high as 0.9) and wavelength-scale thick microlenses with high efficiencies [15]. Conventional diffractive optical elements, typically realized by precision glass surface molding, can aim at realizing the same functionality but their efficiencies are very low [37]. One can also extend this idea to the more general case, where the metasurfaces are made of high-index nanoposts with elliptical cross section, allowing us simultaneously to shape the polarization and phase of the light [16]. This class of metasurface can realize two categories of diffractive optical components. In the first category, one can implement two independent phase masks of any kind for the two orthogonal polarizations. The second category can allow for any desired vector beam generations. This capability clearly contrasts with conventional diffractive optical elements with very limited polarization control.

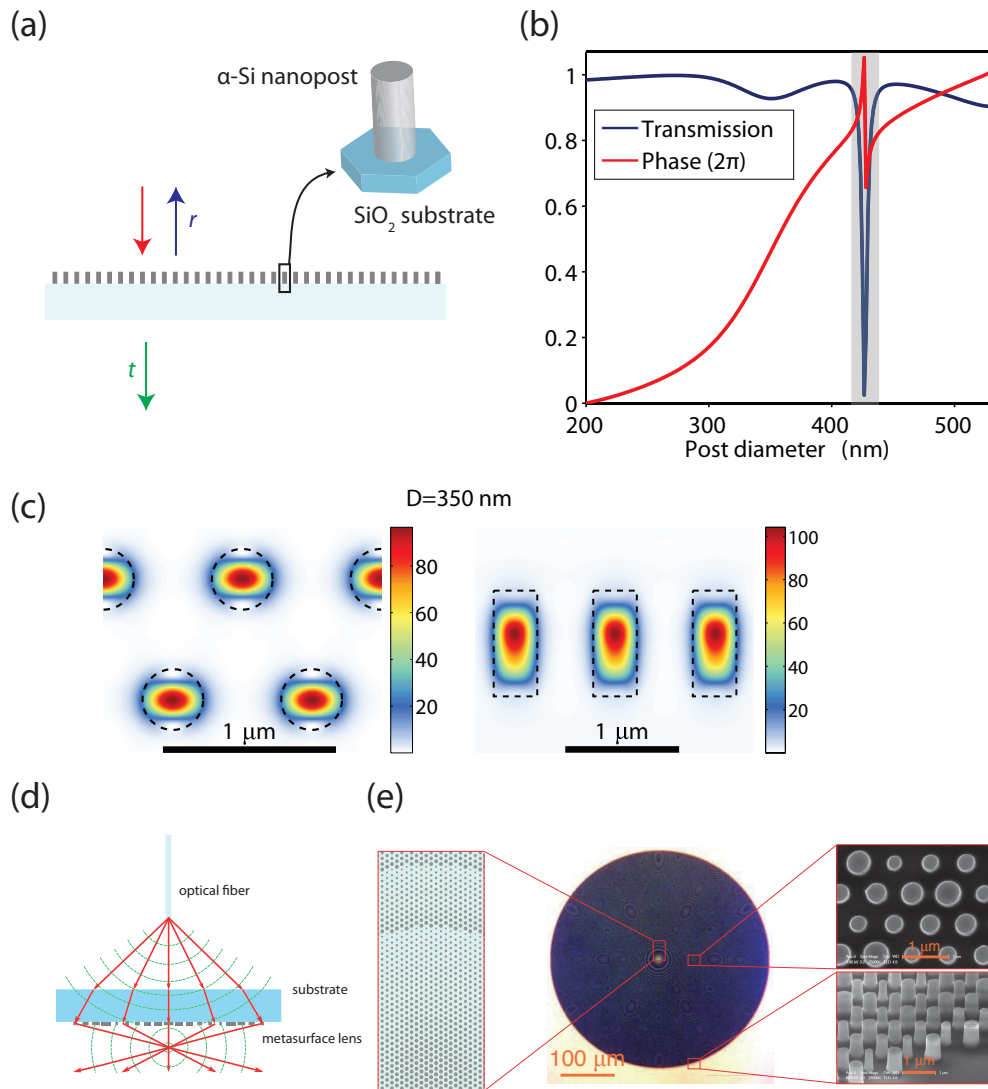


Figure 1.7: **Transmissive dielectric metasurface design.** (a) Schematic of periodic high-index nanosts on a SiO_2 substrate. (b) Transmission and phase responses as a function of high-index nanosts diameter. The nanosts made of $\alpha\text{-Si}$ ($n = 3.43$) have the periodicity of $0.8\ \mu\text{m}$, are $0.94\text{-}\mu\text{m}$ tall and the wavelength is $\lambda = 1.55\ \mu\text{m}$. (c) Magnetic energy densities found by RCWA simulations, indicating each nanost behaves as a highly localized scatterer. (d) Schematic realization of a flat metasurface lens that focuses the light from an optical fiber. (e) Fabricated metasurface lens operating at a wavelength of $1.55\ \mu\text{m}$. The converging wavefront is realized by imparting a space-variant phase profile implemented by locally modifying the diameters of the nanosts.

1.2 Outline of the Thesis

The main goal of this thesis is to demonstrate the potential of high-contrast metas-structures in the realization of unique optical functionalities and new device concepts. The remainder of the thesis describes our works utilizing high-contrast SWG or dielectric metasurfaces. In Chapter 2, we show a novel method for spatially varying the pass-bands of a Fabry–Perot filter set integrated on a single chip by employing the high-contrast metastructures inside relatively high quality factor (Q -factor) resonators. In Chapter 3, we show a transmissive selective color filtering in the visible spectrum, using high-contrast SWG structures, envisioning replacing conventional dye-based color filters toward 1 μm -scale pixel technology. In Chapter 4, we propose a novel device concept of a phase-dominant modulator for free space light. The concept relies on an optical resonance, in which a high-contrast SWG is used to form a compact and highly reflective mirror. We demonstrate a spatial light modulation capability by deploying an array of such phase-dominant modulators on a silicon chip. In Chapter 5, we propose the concept of a disorder-engineered metasurface. The disordered metasurface is used in place of random media in the context of wavefront shaping and to demonstrate unprecedented wavefront manipulation capabilities beyond those of conventional optics.

PLANAR OPTICAL BANDPASS FILTER ARRAY FOR ON-CHIP SPECTROSCOPY

The material in this chapter was presented in part in:

Y. Horie, A. Arbabi, S. Han, and A. Faraon, “High resolution on-chip optical filter array based on double subwavelength grating reflectors”, *Opt. Express* **23**, 29848–29854 (2015) DOI: [10.1364/OE.23.029848](https://doi.org/10.1364/OE.23.029848),

Y. Horie, A. Arbabi, E. Arbabi, S. M. Kamali, and A. Faraon, “Wide bandwidth and high resolution planar filter array based on DBR-metasurface-DBR structures”, *Opt. Express* **24**, 11677–11682 (2016) DOI: [10.1364/OE.24.011677](https://doi.org/10.1364/OE.24.011677),

In this chapter, we show a new method to vary the pass-bands of a Fabry–Perot filter set on a single substrate, as illustrated by two different approaches using high-contrast metastructures. The first approach employs high-contrast subwavelength gratings (SWGs) that exhibit high reflectivity over a very large bandwidth. Two parallel SWGs placed in close proximity can confine Fabry–Perot resonances that act as narrow-band filters, and the filter resonance is controlled by changing the in-plane dimensions of the grating. The second approach uses a transmissive dielectric metasurface sandwiched between two high reflectivity distributed Bragg reflectors (DBRs). Here, the dielectric metasurface is used as a phase shifting element inside a Fabry–Perot cavity without inducing a significant loss. In both approaches, we demonstrate that the pass-bands of high-resolution filters can be precisely controlled by the in-plane dimensions of the SWGs reflectors or the sandwiched metasurfaces, and therefore we can span the resonance over a broad wavelength range as wide as 250 nm around the telecommunication wavelengths ($\Delta\lambda/\lambda = 16\%$) with measured quality factors (Q -factors) greater than 10^3 . The planar geometry and the process compatibility with conventional top-down lithography technique, as well as the large bandwidth that the proposed filter arrays can span, make them ideal for implementation of low-cost miniaturized spectrometers with high resolving powers, as an integral part of equipment for biomedical and environmental sensing.

2.1 Motivation

Spectroscopy is an essential tool in bio-chemical sensing applications, material characterization, and multiple areas of scientific research. Modern spectrometers based on diffraction gratings are widely used because they can achieve a high resolving power and high sensitivity. For multiple applications, including those related to sensors located on handheld devices and low cost portable point-of-care diagnostics [38], there is a continuous interest in miniaturizing spectrometers. However, conventional high-resolution diffraction grating based spectrometers are inevitably bulky as the resolution of the spectrometer scales inversely with optical path length, and thus are not suitable for miniaturization. For this purpose, several integrated optics approaches have been explored [39, 40], such as on-chip frequency filtering based on micro-resonators [41], integrated diffraction gratings [42], and arrayed waveguide gratings [43]. However, in many applications the optical signals of interest are freely propagating, and the low coupling efficiency from free-space to on-chip waveguides limits the sensitivity of this type of spectrometers. An attractive design for a free-space type spectrometer is to use an array of bandpass optical filters in conjunction with a photodetector array [44, 45]. One can obtain the spectral information by measuring intensities of the filtered light within a specific range of wavelengths at each detector, and more importantly the resolving power of the spectrometer is only limited by the resolution of the filters. The most common way to design a high-resolution optical filter is to form a Fabry–Perot resonator using a pair of broadband high reflectivity mirrors [45]. The Fabry–Perot cavity length can be varied in a discrete form through multiple etching steps, or in a continuous form by using an angled surface. The latter creates optical filters with spatially varying center wavelength, named wedge filters or linear variable filters (LVFs), that are manufacturable by linearly varying the cavity thicknesses of the Fabry–Perot resonator [46], and are commercially available [47, 48] (see Fig. 2.1). However, the angle of the wedge eventually limits the Q -factor of the Fabry–Perot cavities and in turn the resolution of the filters due to the non-normal reflection on the angled surface. Alternatively, gray-scale lithography allows a spatially varying cavity thicknesses in a more controlled manner [49], but the technology is expensive and not readily available.

We propose and experimentally demonstrate a novel method to effectively vary the central wavelengths of a Fabry–Perot filter set by two approaches using high-contrast metastructures. We first consider the simple model of a 1-D Fabry–Perot resonator

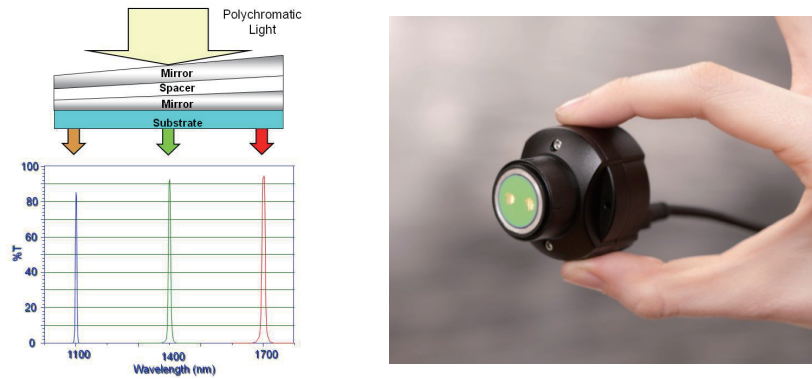


Figure 2.1: **Working principle of compact spectrometers using a wedge filter.** (a) The wedge in the cavity thickness is applied via an intentional tilt between the two mirrors, comprising the set of bandpass filters. (b) The prototype of a compact spectrometer. Figures are adapted from reference [47]. This type of compact spectrometers has been commercialized by Viavi Solutions Inc. [48], formerly known as the part of JDSU.

consisting of two mirrors under a normally incident plane wave illumination. When the mirrors are aligned perfectly parallel, the partial reflections of the two mirrors can constructively interfere each other, constituting a standing wave between the mirrors. This happens when the round-trip phase accumulation is an exact integer multiple of 2π and the condition can be written by

$$\frac{4\pi nL}{\lambda} + 2\angle r_{\text{mirror}} \equiv 0 \pmod{2\pi}, \quad (2.1)$$

where n and L are the refractive index and the thickness of a cavity layer, respectively, $\angle r_{\text{mirror}}$ is the reflection phase of the mirrors, and λ is the resonance wavelength. As is discussed, the only practical way of changing the resonance wavelength λ is to change the cavity thickness L by means of an LVF or gray-scale lithography, whereas the other parameters are fixed. In our first approach, Fabry–Perot resonators are formed by two-layers of highly reflective SWG reflectors [7, 22]. SWG reflectors not only provide broadband reflection spectra comparable to DBRs thus being regarded as the thin-layer alternatives of DBRs, but also, by changing the grating geometry, they allow for engineering the reflection phase while maintaining their reflectivity very high [11]. Replacing conventional mirror made of metals or DBRs with the SWGs adds the control knob to modify the reflection phase $\angle r_{\text{mirror}}$:

$$\frac{4\pi nL}{\lambda} + 2\angle r_{\text{SWG}}(p) \equiv 0 \pmod{2\pi}, \quad (2.2)$$

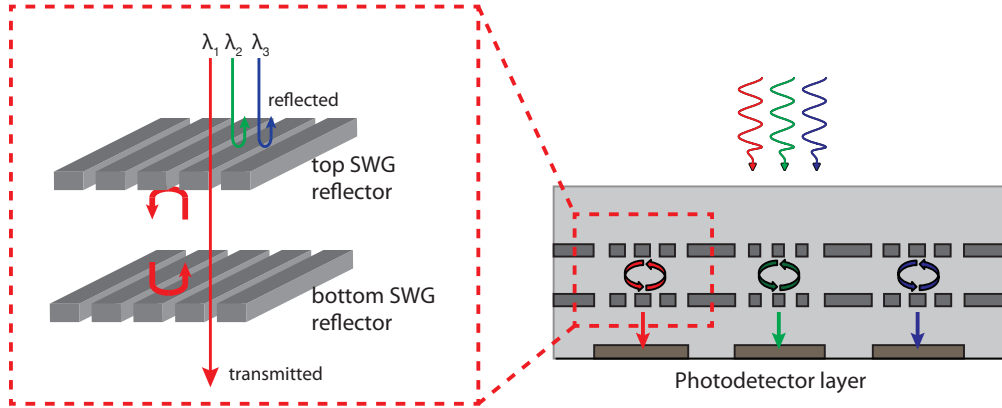


Figure 2.2: **Schematic illustration of bandpass filter array composed of vertical Fabry–Perot resonators realized by two-layers of SWG reflectors separated by a spacer layer.** When broadband input light is illuminated, the spectrum is filtered out by the bandpass filters with different central wavelengths, and the optical powers detected by the underlying photodetector pixels are used to reconstruct the original spectral information.

where $\angle r_{\text{SWG}}(p)$ is the reflection phase of SWGs and the argument p indicates that we have a control knob by the structure. In contrast to the conventional approaches, the resonance wavelengths of the SWG-based Fabry–Perot resonators can be controlled by adjusting in-plane geometries, such as the period or duty cycle, of the SWG reflectors [50]. Therefore, a set of bandpass filters can be easily fabricated using well-established top-down lithographic processes. As schematically shown in Fig. 2.2, each of the bandpass optical filters is made of two identical SWG reflectors separated by a distance on the order of a wavelength of interest, to satisfy the symmetric Fabry–Perot condition. Such symmetric, loss-less Fabry–Perot resonators can be critically coupled, have theoretical transmission of 100% at their resonance wavelength, and reflect back the off-resonance portion of the incident light. In our second approach, a transmissive dielectric metasurface is inserted as an additional phase shifting layer between two high reflectivity mirrors made of DBRs, enabling independent and precise control of the filter’s passbands by controlling the phase shift of the metasurface layer:

$$\frac{4\pi nL}{\lambda} + 2\angle r_{\text{mirror}} + 2\phi_{\text{meta}}(p) \equiv 0 \pmod{2\pi}, \quad (2.3)$$

where $\phi_{\text{meta}}(p)$ is the added phase shift due to the metasurface layer. Metasurfaces are two dimensional arrays of subwavelength scatters capable of controlling the phase, amplitude, and polarization of light [2, 4]. One particularly interesting class of

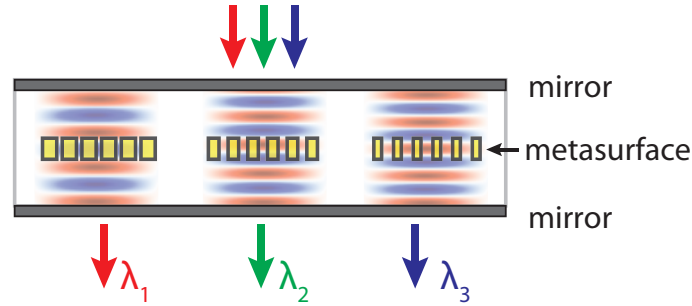


Figure 2.3: **Schematic illustration of the proposed bandpass filter array using a dielectric metasurface.** Each of the filter is composed of vertical DBR-based micro-cavities, in which transmissive dielectric metasurface layers are inserted as phase shifting layers to tune their resonance wavelengths over a broad bandwidth.

metasurfaces is based on high-index nanoposts, which allow both high transmission as well as phase control capability by designing the geometry of the nanoposts. So far, various diffractive optical elements such as high performance flat lenses [13–15] or birefringent optical elements [16] have been demonstrated. Unlike plasmonic metasurfaces, which inevitably suffer from optical loss [51], the loss-less nature of dielectric metasurfaces is suitable for resonant applications. As schematically shown in Fig. 2.3, the dielectric metasurface layers are incorporated in vertical Fabry–Perot resonators with relatively high Q -factors. By incorporating transmissive metasurfaces with different geometries into the cavity of a set of Fabry–Perot filters, the round-trip phase inside the cavity is drastically modified. Thus, the resonance wavelength (i.e., the filter passband) can be tuned without changing the physical distance between the two reflectors. Similar concepts for implementation of an array of Fabry–Perot filters have been previously studied. Walls *et al.* have demonstrated Fabry–Perot filter arrays using metallic mirrors and effective index medium created by subwavelength patterning [52]. Filter arrays composed of dielectric mirrors incorporating 1-D subwavelength gratings as a phase shifting element have also been proposed [53], but, to the best of our knowledge, have not been experimentally demonstrated. Furthermore, compared with 1-D subwavelength gratings, the dielectric metasurfaces provide more control over the phase shifts and are polarization insensitive [13, 15, 16].

2.2 Planar Filter Array Using Double Subwavelength Grating Reflectors

To investigate the performance of the bandpass filters using double SWG reflectors, we first designed an SWG reflector that operates in a wide wavelength range around the telecommunication band ($\lambda = 1550$ nm). The broadband SWG reflector design typically involves a subwavelength periodic structure made of a high-refractive index material surrounded by a low refractive index material. The subwavelength geometry of the grating suppresses higher order diffraction for normally incident light. The high-index contrast system makes waveguide modes in the high index structure highly dispersive, opening up unique properties such as highly reflective [7, 11, 22] or transmissive [13, 15] amplitudes in broadband, which cannot be explained by the traditional effective medium theory (EMT) [18]. The details of the operating principle and design for the SWG reflector are discussed in Chapter 1 or can be found in references [23, 24]. Without loss of generality, the SWG reflectors considered here are 1-D gratings made of high-index α -Si and embedded in low-index SU-8 polymer on a fused silica substrate. We used the rigorous coupled-wave analysis (RCWA) technique [28] to find the optimal SWG reflector designs. The basic reflectors

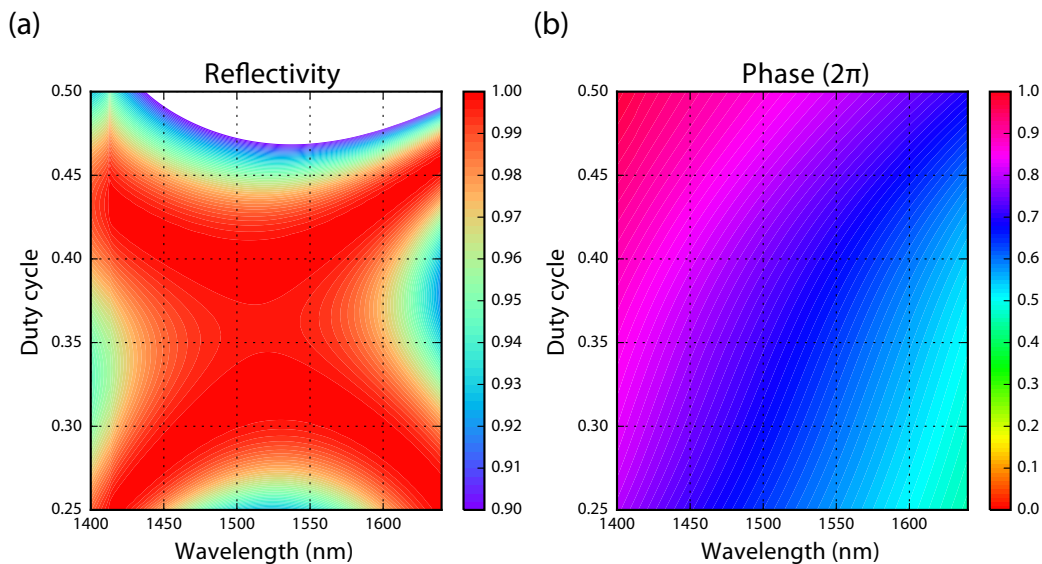


Figure 2.4: **Design of SWG reflectors.** (a) Simulated reflectivity contour map as a function of duty cycle of SWGs and wavelength, for the α -Si on SiO_2 1-D SWGs with 900 nm period and SU-8 polymer cladding for the normally incident TE-polarized light (i.e., electric field parallel to the grating bars) and (b) the corresponding reflection phase contour map.

designed for the normally incident TE-polarized light (i.e., electric field parallel to the grating bars) have a period of 900 nm and a grating thickness of 310 nm. Figure 2.4 shows the reflectivity spectra and the associated reflection phase for the SWG reflectors as a function of the SWG duty cycle and the wavelength.

When two of such SWG reflectors are placed in parallel [54] and separated by a 1.23 μm -thick SU-8 spacer layer, a single Fabry–Perot resonance within the highly reflective stopband is observed. The SU-8 spacer layer thickness between the two SWG layers must be thicker than at least half of the wavelength such that evanescent field coupling between the two SWG layers is avoided. The low near-field coupling between the gratings should reduce the sensitivity of the structure, making it robust against the in-plane translational misalignment of the two gratings. The rotational misalignment of the two gratings should become more sensitive when 1-D gratings are used, but can be tolerated using polarization-independent 2-D SWG designs discussed later. Using the results for the SWG reflectors, the resonance wavelengths of the Fabry–Perot resonators were calculated while varying the in-plane grating parameters such as period and duty cycle, while keeping the thicknesses of the gratings constant. To ensure a proper spectral filtering function, it is crucial to avoid the overlap of the Fabry–Perot resonance with other undesired resonances or the stopband edge of the SWG reflectors. Then, a set of optimum filter designs which provide a wide wavelength range of operation as well as narrow-band transmission was identified. The simulated transmission spectra of these filters are plotted in Fig. 2.5(a). The simulations were performed using RCWA techniques. Filtering operation over a wide range of $\Delta\lambda = 70 \text{ nm}$ ($\Delta\lambda/\lambda = 5\%$) with moderately high Q -factors larger than 1,000 can be achieved in the proposed SU-8/Si/SiO₂ high index contrast system by introducing changes both in the duty cycles and the periods of the SWG reflectors. The variation in the peak transmittance of the filters is caused by the difference in the reflection amplitudes for the top and bottom SWG reflectors, which led to over- or under-coupling condition for some of the Fabry–Perot filters. The wavelength coverage can be further enlarged using higher index contrast gratings such as air-cladded silicon gratings which in general provide a broader SWG reflection reflection band. Since the structure can be scaled with the wavelength, the proposed design is readily customizable to any wavelengths of interest, provided high-index contrast materials in combination with low loss are available. The 1-D SWG reflector we use here shows large reflectivity only for the TE polarization and as a result, the bandpass filters function only for the TE-polarized light; however, polarization-insensitive filters can also be designed by replacing the 1-D SWG

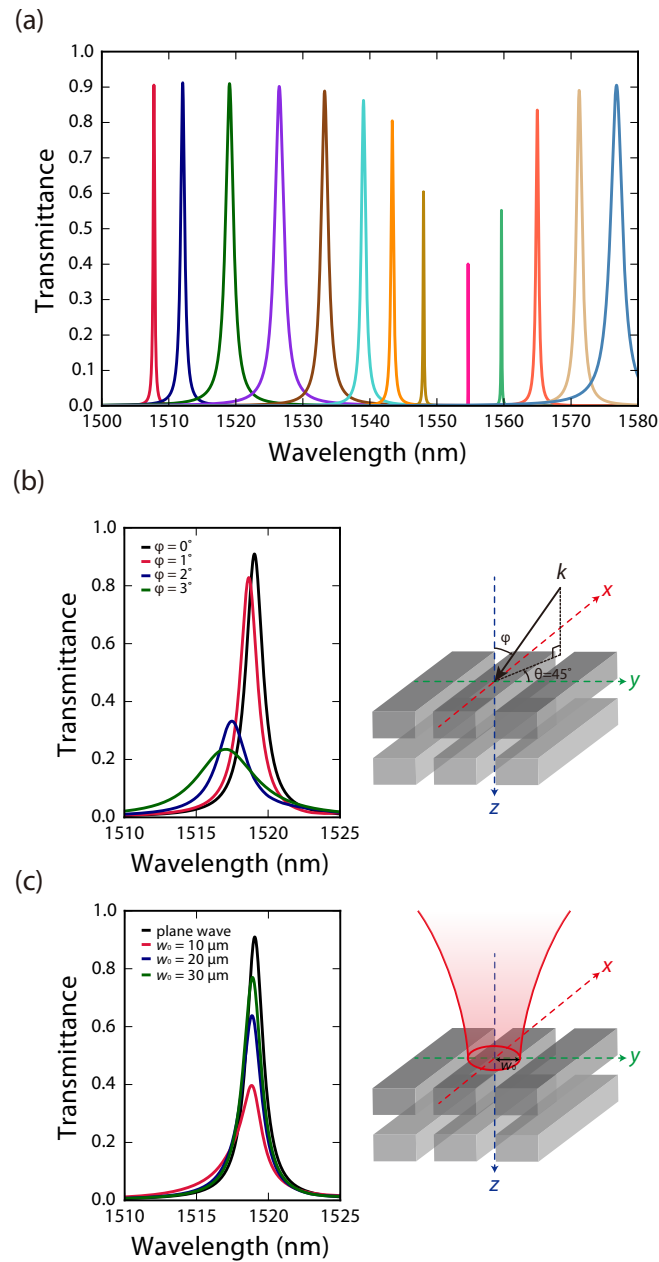


Figure 2.5: **Simulated transmission spectra of bandpass filter array.** (a) Simulated transmission spectra of a normally incident plane wave for a set of bandpass filters. (b) Angular dependence of the simulated transmission spectrum of one of the filters with an azimuthal angle of $\theta = 45^\circ$ and various polar angles φ . (c) Simulated transmission spectra of one of the filters when illuminated with Gaussian beams with different beam waists w_0 .

reflectors with polarization-insensitive 2-D SWG reflectors proposed in references [55–57].

It is also important to analyze the angular sensitivity as well as the dependence on an input beam size of the bandpass filters. Simulated angular dependence of the transmission spectrum of one of the filters is presented in Fig. 2.5(b), indicating that the resonance wavelength is shifted to a shorter wavelength for larger angles of incidence. The maximum transmittance is also decreased as the angle of incidence changes because the reflection amplitudes for the top and bottom SWG reflectors become deviated as the angle of incidence changes. This behavior is unique, compared to the Fabry–Perot resonator formed using a pair of DBRs, as the reflection coefficient for SWG reflectors has more angular dependence than DBRs. From the angular response of the SWG reflectors, one can calculate transmission spectra under Gaussian beam illumination: first, using the Fourier transform, the incident Gaussian beam is expanded in terms of plane waves propagating at different angles, then, the amplitude of each of the transmitted plane waves is found using their amplitude in the expansion and their corresponding transmission coefficient which is computed using RCWA, finally, the transmitted beam is found by adding the contributions from all the plane waves (i.e., by an inverse Fourier transform). Figure 2.5(c) shows the simulated transmission spectra for normally incident Gaussian beams with different beam waists computed using this technique. It is assumed that the beam waist is at the same plane as the top SWG. As the beam waist gets smaller, the maximum transmittance is decreased because Gaussian beams with smaller beam waists have a larger plane wave angular spectrum and, as Fig. 2.5(b) indicates, a coupling condition becomes more deviated from the critical coupling for plane waves with non-normal incidence angles. Thus, one can expect the maximum transmittance as well as a higher Q -factor when the filters are tested using a collimated light rather than the focused light. Several approaches have been reported to achieve the lateral confinement by effective index confinement method [58] or reflector phase gradient approach [59], which could help to design the laterally confined resonator with better transmission efficiencies.

2.3 Characterization of Double Grating band-pass Filters

Fabrication

As a proof of concept, the bandpass filter array using the two-layers of SWG reflectors was fabricated on a fused silica substrate as illustrated in Fig. 2.7(a). First, an α -Si

layer was deposited with a thickness of 310 nm by plasma-enhanced chemical vapor deposition (PECVD) method. The grating pattern was defined by electron beam lithography using a positive resist (ZEP520A) followed by inductively coupled plasma reactive ion etching (ICP-RIE) process using $\text{SF}_6/\text{C}_4\text{F}_8$ mixed plasma chemistry for patterning the first α -Si layer. The patterned α -Si was planarized by spin-coating with SU-8 2002 followed by thermal reflow at 250°C , ending up with a $1.23\ \mu\text{m}$ spacer layer. Subsequently, a second layer of PECVD-grown 310 nm-thick α -Si layer was deposited on top of the planar SU-8 layer. Then, another layer of the SWG pattern was aligned to the first layer and etched using the same lithographic mask and etching processes. Finally, the whole structure was cladded with SU-8, and planarized by reflowing the SU-8 at 250°C . Diagrammatic representation of the double SWGs fabrication process is illustrated in Fig. 2.6. A typical cross-sectional image of the fabricated double layers of SWGs is shown in Fig. 2.7(b).

Characterization

The fabricated bandpass filter array was characterized by measuring the transmission spectra of the filters using a tunable laser and collecting the transmitted light from the filters on an InGaAs photodetector. Using an objective lens, the collimated and

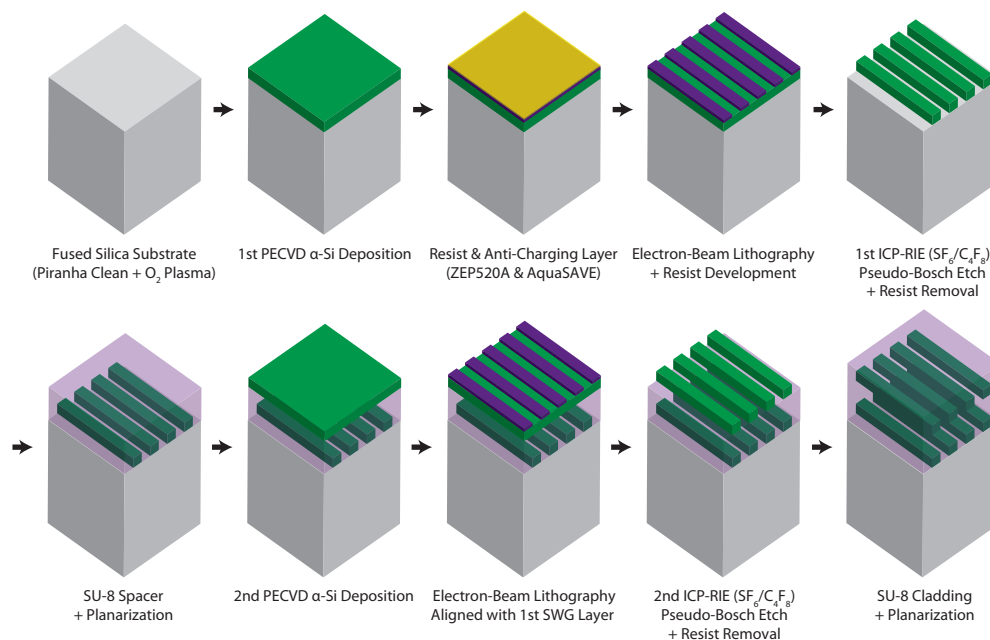


Figure 2.6: **Double SWGs fabrication process.** Diagrammatic representation of the double SWGs fabrication.

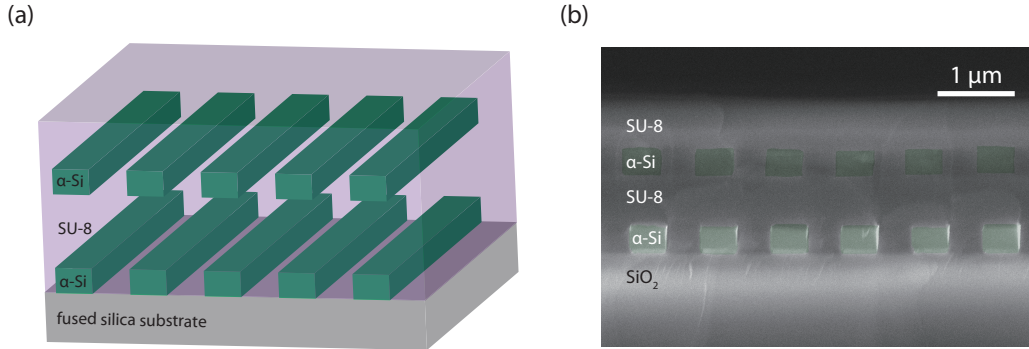


Figure 2.7: **Fabrication of double SWG reflectors.** (a) Schematic of a bandpass filter made of two-layers of SWG reflectors in the SU-8/ α -Si/SiO₂ system. (b) Cross-sectional SEM image of a fabricated bandpass filter.

linearly TE-polarized beam from the laser was focused onto each filter from the normal direction. The beam diameter at focus was about 20 μm. The measured transmission spectra for a set of bandpass filters are shown in Fig. 2.8. The Q -factors of the filters range from 1,100 to 3,000 (the linewidths range from 0.5 nm to 1.4 nm) and the maximum transmission ranges from 40% to 65%, as expected for a Gaussian probe beam (Refer to the simulation of the beam diameter dependence shown in Fig. 2.5(c)). Compared with the simulated transmission spectra under a plane

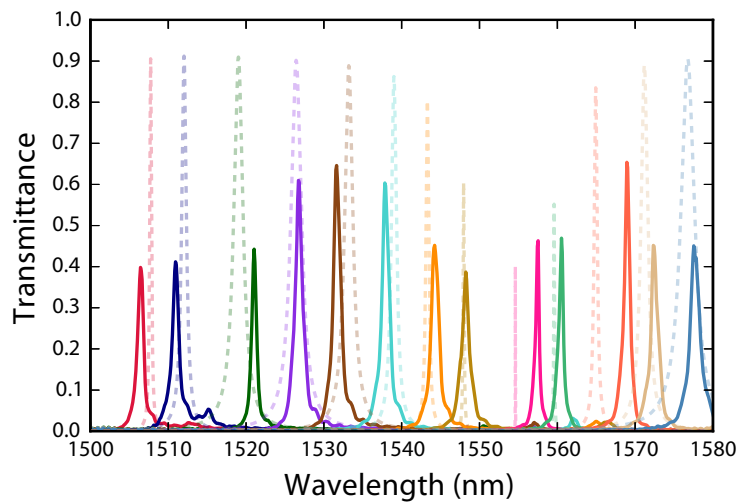


Figure 2.8: **Measured transmission spectra of a set of fabricated bandpass filters.** The grating duty cycle and period are controlled to obtain a sets of bandpass filters with different central wavelengths. The corresponding simulated transmission spectra for a normally incident plane wave illumination for the corresponding sets of bandpass filters are also shown in dotted lines.

wave illumination, the resonance wavelengths in the measured spectra have a good agreement with the numerical simulations and small discrepancies between the measured and simulated values are due to fabrication errors. Outside of the passband, the measured stopband transmittance was less than 1% within the wavelength range of interest, owing to the highly reflective properties of the designed SWGs. It is also worth to note that the system here is not limited by scattering or absorption loss. This was confirmed by checking that the sum of the transmitted and reflected power is constant around the resonances.

2.4 Planar Filter Array Using DBR-Metasurface-DBR Structures

From this section, we describe the second approach that utilizes a layer of dielectric metasurface inserted in a conventional DBR-based Fabry–Perot filter. To design the Fabry–Perot filters, we first simulate and design transmissive dielectric metasurfaces using the RCWA technique. We use transmissive dielectric metasurfaces that consist of α -Si ($n = 3.40$) nanoposts on a square lattice (period: 600 nm, height: 400 nm) embedded in low-index SU-8 ($n = 1.57$). The metasurface parameters are determined for achieving a large variation in the transmission phase by changing the width of the nanoposts, while the transmission is high enough within the wavelength range from 1450 nm to 1700 nm, as plotted in Fig. 2.9(a,b). We use DBRs as the high reflectivity mirrors forming the Fabry–Perot resonator. Each of the DBRs consists of 4 pairs of α -Si and silicon dioxide (SiO_2) ($n = 1.47$) quarter-wavelength stacks. The simulated reflection spectrum of such a DBR is plotted in Fig. 2.9(c), and shows a stop-band in the range of $\Delta\lambda \sim 300$ nm around $\lambda = 1550$ nm with reflectivities $R > 0.99$. When the cavity thickness is a half integer multiple of wavelength divided by the cavity refractive index, the Fabry–Perot resonance is formed inside the cavity and allows a single Lorentzian shaped peak in the transmission spectrum. For this work, we chose the longitudinal mode number of 3 and found a single resonance within the DBR’s stopband when the spacing between the DBR was filled with ~ 1.2 - μm -thick SU-8 polymer. Then, we incorporated the metasurface layers inside the SU-8 cavity layer to introduce the phase shift, and thus shift the resonance wavelengths of the Fabry–Perot resonators without changing the physical distances between the mirrors (Figure 2.9(d)). We used the transfer matrix formalism to calculate the transmission spectra for a set of filters, using the complex transmission/reflection coefficients for the metasurface layers obtained via the RCWA simulations.

In Fig. 2.9(e), the simulated transmission spectra for a set of designed filters are

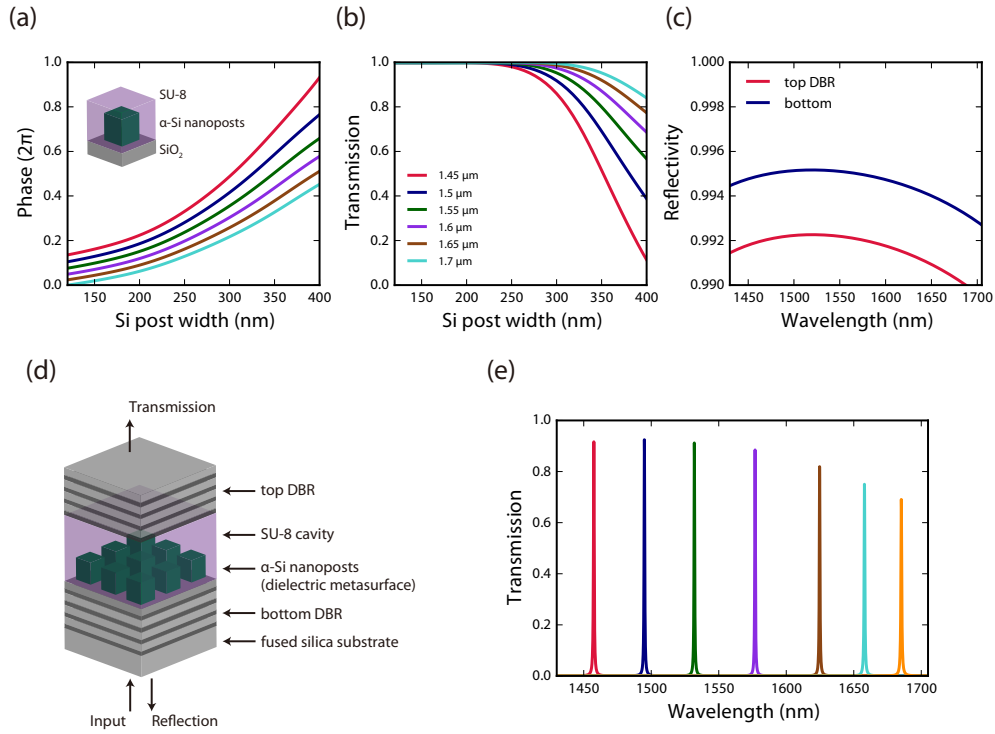


Figure 2.9: **Design of DBR-metasurface-DBR bandpass filter.** (a) Transmission round-trip phase, and (b) transmission intensity induced by α -Si nanoparticles as a function of post width for different wavelengths. The inset figure in (a) represents the refractive index profile of the dielectric metasurface considered. (c) The simulated reflection spectrum of DBRs. (d) Schematic illustration of the proposed filters. The filters are composed of two DBRs and a phase shifting dielectric metasurface layer. The metasurface is made of a uniform array of square cross section nanoparticles. (e) Simulated transmission spectra of a set of filters as shown in (d) with different nanopost widths.

plotted. For this set, the widths of the α -Si nanoparticles range from 120 nm to 430 nm. By changing the widths of nanoparticles array, the resonance wavelengths of the bandpass filters vary from 1450 nm to 1700 nm, spanning a 250 nm bandwidth ($\Delta\lambda/\lambda_c = 16\%$), while the physical distance between the two mirrors in each filter is fixed. The planar form of these filters allows their fabrication using a single binary lithography step. Each of the filters has a high transmission around the passband due to the low-loss materials used in the designed nanopost metasurfaces. The square cross section of the nanoparticles and the square form of the lattice lead to the polarization insensitivity of the metasurface layer and the filters.

2.5 Fabrication and Characterization of DBR-Metasurface-DBR Bandpass Filters

Fabrication

As a proof of concept, the designed set of filters was fabricated on a single fused silica substrate. First, the bottom DBR layers, a 258-nm-thick SiO₂ spacer layer and a 400-nm-thick α -Si layer were deposited by PECVD. The nanopost patterns were defined by electron beam lithography, first transferred into an Al₂O₃ hard mask using a lift-off technique, and then to the α -Si layer by dry etching. Then, SU-8 polymer was spun and hard-baked, planarizing the entire area on the substrate. Subsequently, the top DBR layers were deposited by PECVD over the planar SU-8 layer. Finally, another SU-8 polymer layer was spun to make the index profile along the z -direction symmetric. Diagrammatic representation of the DBR-metasurface-DBR filter process is illustrated in Fig. 2.10. The cross-sectional SEM image of the fabricated structure is shown in Fig. 2.11(a). Two bird's-eye views of the α -Si nanoposts with two different widths before spinning the SU-8 are also shown in Fig. 2.11(a) as insets. Each of the DBRs were composed of 4 alternating pairs of α -Si and SiO₂ layers (α -Si layers: 112 nm, SiO₂ layers: 258 nm).

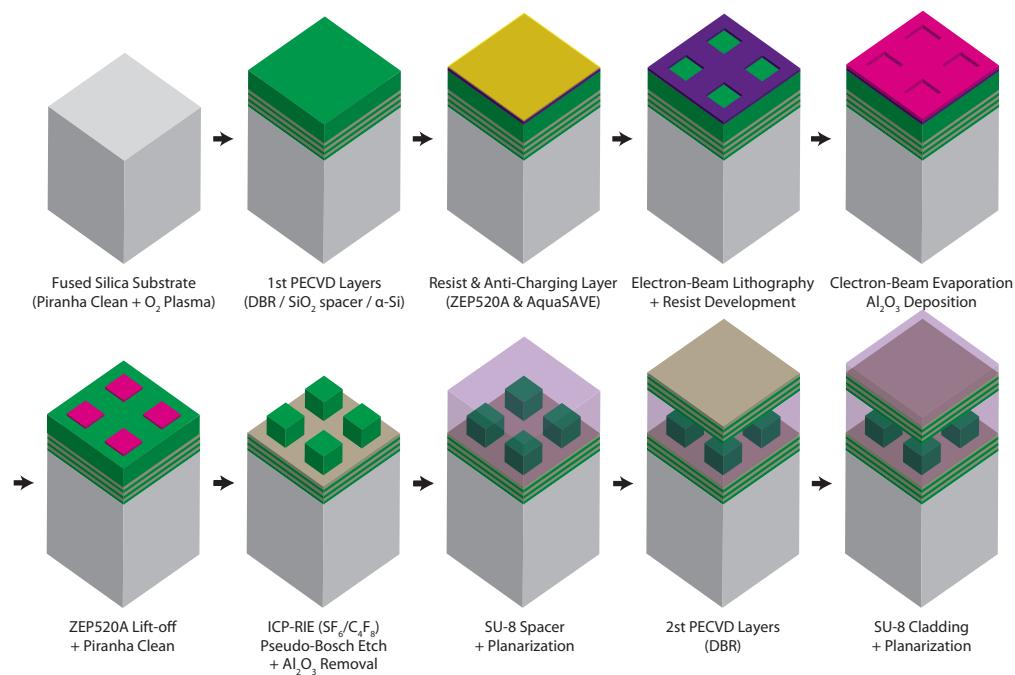


Figure 2.10: **DBR-metasurface-DBR filter fabrication.** Diagrammatic representation of the DBR-metasurface-DBR filter fabrication.

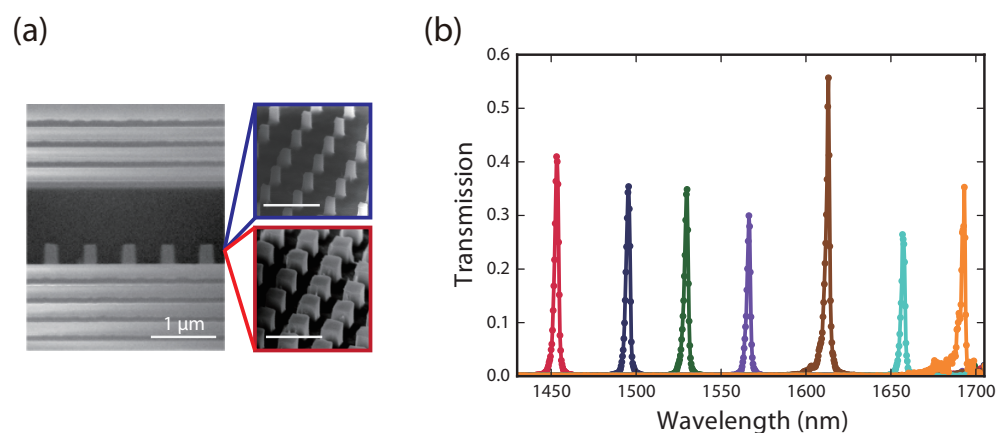


Figure 2.11: **Experimental results of fabricated DBR-metasurface-DBR bandpass filters.** (a) A cross-sectional SEM image of a fabricated filter, and bird's-eye views of two α -Si nanopost arrays with different widths. Scale bars are all 1 μm . (b) Measured transmission spectra for the set of fabricated bandpass filters. The average measured absolute transmission for the filters is $41 \pm 15\%$ and their quality factors are around 700.

Characterization

The fabricated bandpass filter array was characterized by measuring the transmission spectra of the filters. A supercontinuum source was focused onto the fabricated filters using an objective lens, the transmitted light was collected using another objective lens, and its spectrum was measured using an optical spectrum analyzer. The normalized transmission spectra were calculated by measuring the spectrum without the sample. Figure 2.9(e) shows the simulated transmission spectra computed for the fabricated designs, and Fig. 2.11(b) shows the measured transmission spectra for the corresponding set of the filters with normalization. The resonance wavelengths show good agreement between their simulated and measured values. The measured Q -factor was ~ 700 , and the measured absolute transmission power was 16% in average. The transmission measured from the area having no α -Si nanoposts shows similar peak transmission values and Q -factors, indicating that the relatively low transmission and the measured linewidths of the filters are due to the loss from the fabricated DBRs. The deposited DBR layers have significant surface roughness leading to scattering loss. Optimization of the PECVD deposition conditions is expected to reduce the surface roughness of the deposited layers and improve the Q -factors as well as the transmission power of the filters.

2.6 Summary and Outlook

We proposed and experimentally demonstrated a planar bandpass filter array on the same chip, based on vertical Fabry–Perot resonators, where two different approaches were taken; (1) double layers of high-contrast SWGs mirrors were used to form a Fabry–Perot resonator and (2) a dielectric metasurface was inserted in the middle of a DBR-based vertical Fabry–Perot resonator. In both approaches, the geometries of the high-contrast metastructures were precisely controlled by the standard lithographic technique, to induce appropriate phase shifts in the Fabry–Perot filters, allowing to widely span the center wavelengths of the bandpass filters without changing the thicknesses of the devices. The planar geometry and the compatibility with binary lithography process of the demonstrated structures, as well as large wavelength range that the proposed filter array can cover make it ideal for implementation of low-cost compact spectrometers with high resolving powers.

The demonstrated Fabry–Perot resonator containing high-contrast metastructures adds an additional degree of freedom in the design of a resonator. As we already discussed in the context of lateral confinement, it is possible to design a spatially varying phase profile on the mirror by locally changing the high-contrast metastructures [11], which in turn allows us to explore exotic modes such as a resonance that has a specific polarization state [59] and nonzero-order Hermite–Gaussians [26]. Another interesting direction is to look at angular and wavelength dispersion of a Fabry–Perot resonator. One of the well-known properties of a Fabry–Perot resonator is that its resonance wavelength is sensitive to the angle of incidence, due to that the round-trip path length is changed depending on the angle. Wang *et al.* [60] proposed to use high-contrast SWG in a vertical microcavity to engineer the angular dispersion of the resonator. Interestingly, the angular dispersion of the reflection phase of high-contrast SWGs can become either positive or negative. One can make use of this unique property to engineer the angular dispersion of a Fabry–Perot resonator; it is even possible to design an angular-insensitive Fabry–Perot resonator by compensating the angular dependent round-trip phase dispersion by the high-contrast metastructures. The wavelength dispersion of dielectric metasurface is also uniquely engineered by carefully choosing the dispersion of meta-atoms [61]. Lin *et al.* [62] proposed a nontrivial method to couple broadband light into a high Q -factor resonator by devising the use of negative dispersion in a diffractive optical element. The addition of the unique dispersion characteristics of high-contrast metastructures into resonator physics may open up possibilities to design optical resonators with unusual properties.

VISIBLE WAVELENGTH COLOR FILTERS USING SILICON SUBWAVELENGTH METASTRUCTURES

The material in this chapter was presented in part in:

Y. Horie*, S. Han*, J.-Y. Lee, J. Kim, Y. Kim, A. Arbabi, C. Shin, L. Shi, E. Arbabi, S. M. Kamali, H.-S. Lee, S. W. Hwang, and A. Faraon, “Visible wavelength color filters using dielectric subwavelength gratings for backside-illuminated CMOS image sensor technologies”, *Nano Lett.* **17**, 3159–3164 (2017) DOI: [10.1021/acs.nanolett.7b00636](https://doi.org/10.1021/acs.nanolett.7b00636),

State-of-the-art, complementary metal oxide transistor (CMOS) image sensors have pixel sizes that are only a few micrometers in size. The color filtering is achieved by a material absorption using organic dye filters that are not effective for further miniaturization of pixel size and can suffer long-term degradation. Thus, it is imperative to find novel technologies for on-chip filtering. In this chapter, we present highly efficient, visible wavelength RGB color filters based on high-contrast metastructures that may replace conventional organic dye-based color filters used in CMOS image sensor (CIS) technologies. High-contrast metastructures made of low-loss polycrystalline silicon (poly-Si) materials can form relatively strong optical resonances that allow us to engineer unique spectral features across entire visible wavelengths. The set of RGB color filters, specifically optimized for backside-illumination (BSI) CIS technologies using image signal processing pipeline, exhibits highly efficient peak transmittance 60-80%, and more importantly, an almost insensitive angular response over a $\pm 20^\circ$. The effect of finite size pixels, comparable to the pixel sizes used in state-of-the-art CIS technologies, is discussed in conjunction with the angular responses.

3.1 Motivation

Scalability of CMOS technology has improved the performance of CIS in the past decade. One of the trends in the CIS technology, driven mainly by portable devices with small form-factors, is to decrease the pixel size, which will lead to improved spatial resolution for digital imaging [63]. The scalability of CIS technology has

enabled lateral pixel size to be reduced from more than 10 μm to less than 2 μm in the past decade [64, 65]. Along with scaling of the pixel size, there have been considerable efforts to redesign color filters [66–68], microlenses [69], and infrared filters [70] to prevent the degradation of the optical performance. Dye-doped polymers have been conventionally used for RGB color filters in digital color imaging. However, when the pixel size gets smaller, the optical crosstalk among pixels becomes significant because of the small absorption coefficient of the organic dyes. Additionally, the dye-doped polymers are essentially photoresists that degrade under ultraviolet illumination or high temperature environments. To address these issues, plasmonic color filters made of metallic thin films with subwavelength patterning have been studied for CIS technology [67, 71, 72]. The plasmonic color filters have several advantages such as flexible color tunability across the visible spectrum and compatibility with CMOS processes. However, the absolute efficiency of the plasmonic color filters is relatively low (40-50% range) compared to conventional organic dye-doped filters. Here, we show that dielectric subwavelength gratings (SWGs) can be used to achieve highly efficient transmission color filters with close to angular insensitive properties. Furthermore, compared to dye-based filters, our dielectric-based filters possess better reliability under ultraviolet illumination and at high temperature. For the optimized filter designs, we take advantage of BSI-CIS technologies, where the color filter layer can be placed in close proximity to the photodiode device layer.

SWGs provide numerous opportunities to manipulate optical waves especially when the dielectric constant of the grating is high. Owing to the subwavelength size and high-index contrast, the subwavelength structures can be engineered to support relatively strong optical resonances that can enhance the spectral features [3]. Various designs have been studied for various applications, including visible wavelengths structural colors [73–75], RGB color filters for polarization-sensitive transmission filter [76] and polarization-insensitive reflective RGB color filters [77], antireflection coating [78, 79], and reflective-transmission filters for displays [80]. In this chapter, we demonstrate designs for polarization insensitive filters made of poly-Si located on a SiO_2 spacer layer that separates them from the silicon photodiode layer as schematically shown in Fig. 3.1. For ease of scalable fabrication, we also restrict the thicknesses to be equal among the set of red (R), green (G), and blue (B) filters. Our material choice for the gratings is poly-Si that has a high refractive index ($n > 3.5$) as well as sufficiently low absorption ($\kappa < 0.2$) over the entire visible wavelength range (see Fig. 3.10 in Appendix).

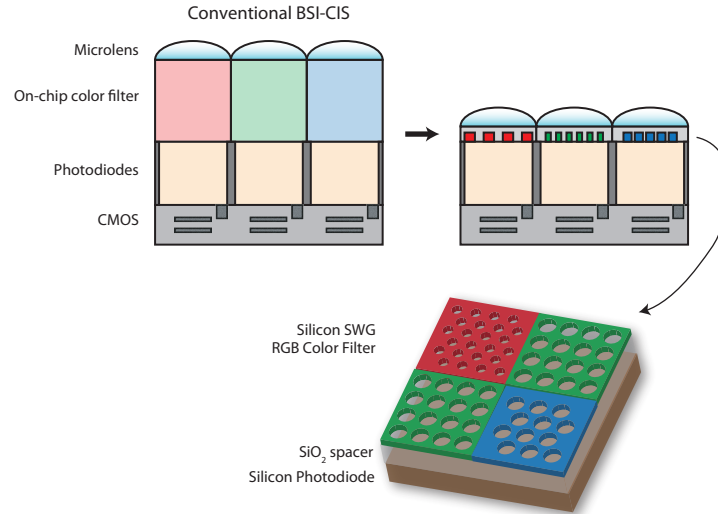


Figure 3.1: **Schematic of visible wavelength on-chip color filters using dielectric SWGs.** Instead of the conventional dye-doped polymers, high-contrast SWGs can be used for efficient RGB filtering. The top-right schematic illustrates the cross-section of a BSI-CIS, which arranges the CMOS wiring layer behind the silicon photodiodes. The bottom panel is a schematic illustration of the realization of the Bayer pattern using dielectric SWG color filters. The design consists of a patterned 80-nm-thick poly-Si slab on a 115-nm-thick SiO_2 spacer layer sitting on BSI silicon photodiodes.

3.2 Design of Visible Wavelength RGB Color Filters

We optimized the shape parameters for the primary set of RGB transmissive color filters based on the similarity to our reference filter spectra and luminance signal-to-noise ratio (YSNR) in color image sensors [81]. The optimum structure is an 80-nm-thick poly-Si slab with air holes, placed on a 115-nm-thick SiO_2 spacer layer sitting on BSI silicon photodiodes. The red design has a period of 250 nm with a 90 nm hole diameter in hexagonal lattice, the green design has a period of 180 nm with a 140 nm hole diameter in a square lattice, and the blue design has a period of 270 nm with a 240 nm hole diameter in a hexagonal lattice. The transmittance spectra of the filters are computed by RCWA technique, shown in Fig. 3.2(a). The simulations include the effect of the SiO_2 spacer layer. The interference between the light passing through the high-index-contrast grating layer and the reflection from the underlying silicon photodiodes layer, results in a color-selective transmission spectrum with peak transmittance of 60-80%. Based on calculations, substantial YSNRs are expected by calculation, when applying the IR-cut filter spectrum of the lens modules and the image signal processing pipeline. For average color error 4, $\text{YSNR} = 28.4$ at

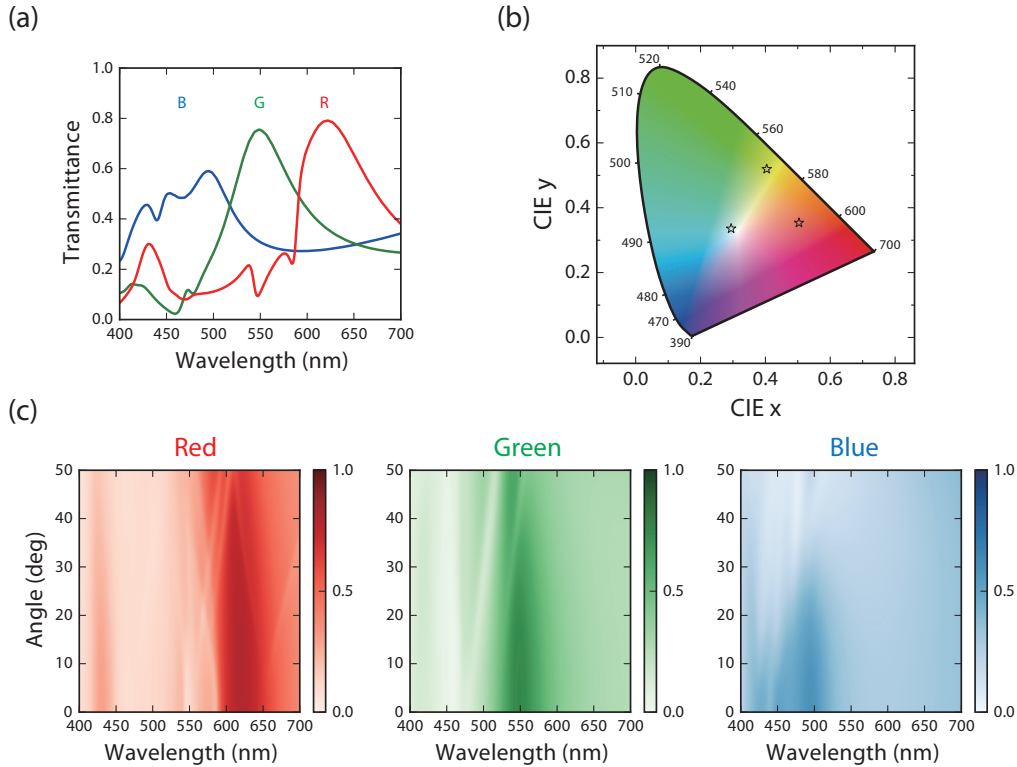


Figure 3.2: **Visible wavelength on-chip color filters using dielectric SWGs for BSI-CIS applications.** (a) RCWA simulation results of the transmission spectra under normal incidence, optimized for the RGB primary colors. (b) Chromaticity coordinates of the optimized color filters in CIE 1931 chromaticity diagram. (c) RCWA simulations of the angular dependence of the corresponding transmission spectra for unpolarized light (see Fig. 3.7 in Appendix for polarization dependence).

low light condition (20 lx) and $YSNR = 39.9$ at high light condition (700 lx) were obtained. We note that using current color filters technology the $YSNR$ values are smaller: $YSNR = 22.0$ at 20 lx and $YSNR = 33.3$ at 700 lx. The chromaticity coordinates of the optimized color filters when a conventional IR-cut filter is applied are shown in the CIE 1931 chromaticity diagram (Figure 3.2(b)). Because of the rotational symmetry of the structures, the spectral response is polarization-insensitive for normal incidence. Also, importantly, the filters exhibit relatively insensitive angular responses for each color as can be seen in Fig. 3.2(c), which is crucial for maintaining the transmitted color when shrinking the pixel size, as further discussed in this chapter later on.

3.3 Fabrication and Characterization of Visible Color Filters

Fabrication

The optimized color filters were fabricated using poly-Si materials prepared by α -Si deposition followed by a high-temperature furnace annealing method [82–85]. An α -Si thin film as well as a thin SiO₂ cap layer was deposited by low-pressure chemical vapor deposition (LPCVD) method[†] on a silicon substrate as well as on a quartz substrate. Then the films were crystallized to poly-Si of low extinction coefficient using furnace annealing at 950°C. Nanohole patterns of ZEP520A resist were defined on the poly-Si surface using electron beam lithography methods. The ZEP520A resist served as a mask for dry etching of the 80-nm-thick silicon layer. A sulfur hexafluoride (SF₆) and octafluorocyclobutane (C₄F₈) mixture gas was used for dry etching of poly-Si and forming pattern profiles with right angle. Residual resist was removed by sulfuric acid. Diagrammatic representation of the RGB visible color filter fabrication is illustrated in Fig. 3.3.

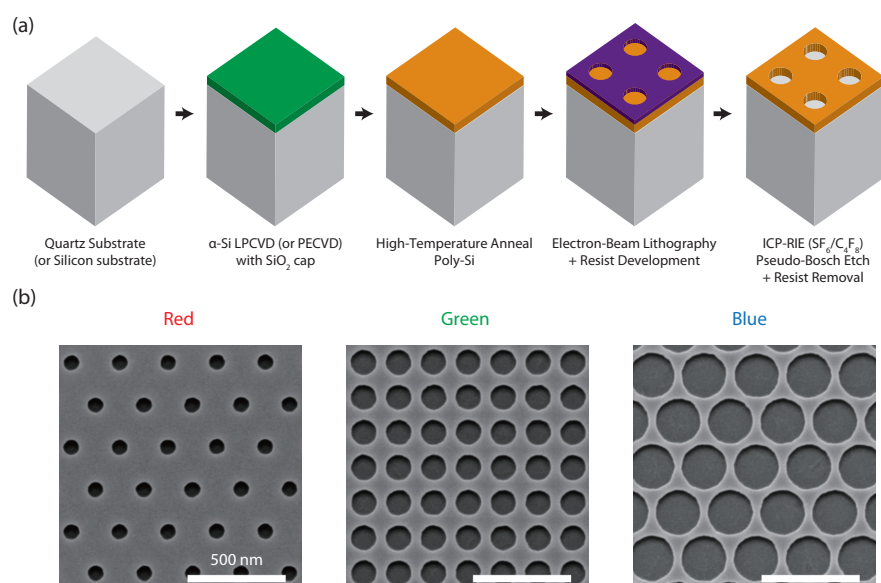


Figure 3.3: **RGB visible color filter fabrication.** (a) Diagrammatic representation of the RGB visible color filter fabrication. (b) SEM images of the fabricated color filters. The scale bars are 500 nm.

[†]Initially, we developed the crystallization recipe for α -Si thin film grown by plasma-enhanced chemical vapor deposition (PECVD) using two-step high-temperature furnace annealing.

Characterization

In our proof-of-concept experiments, instead of directly measuring transmission through the designed filter structures into the photodiode silicon layers, we characterized the reflection from the SWG with a SiO₂ spacer layer fabricated on a silicon substrate, and also the transmission through the SWG layer with the same design fabricated on a transparent quartz substrate. SEM images of the fabricated color filters are shown in Fig. 3.3(b). To characterize the reflection/transmission spectra for the fabricated color filters, we used a custom built confocal microscope setup illustrated in Fig. 3.11 in Appendix. We used a fiber-coupled collimated light from a Tungsten-Halogen lamp (HL-2000-HP, Ocean Optics) as a broad-band light source. The sample was illuminated with the collimated light and imaged by a pair of 20× infinity-corrected objective lens (LMPLFLN20x, Olympus) and a tube lens with a focal length of 150 mm onto a pinhole with diameter of 100 μm to select the region of interest. From the magnification of the relay lens, we effectively collected the reflection/transmission spectrum from 6 μm circular apertures. The spatially filtered light was coupled into a spectrometer (SpectraPro-2500i, Princeton Instruments). The sample was mounted on a rotation mount to measure the transmission spectra for different incident angles. In Fig. 3.4(a,b), reflection and transmission spectra (solid line) are shown along with the RCWA-simulated spectra (dotted line). Both reflection and transmission spectra for each color filter design show good agreement between their simulation and measurement. Note that the reason that the transmission and reflection are not complementary is because the reflectance graphs in Fig. 3.4(a) account for the interference between the light passing through the high-index-contrast grating layer and the reflection from the underlying silicon photodiodes layer.

To investigate the effect of the finite size pixels on the filtering properties, we characterized the transmission microscope color images for the samples fabricated on the quartz substrate. We fabricated several pixels with sizes of 30 μm, 5 μm, 3 μm, and 1 μm. The corresponding optical microscope images are shown in Fig. 3.5(a,b) and the SEM image of the 1 μm-pixel Bayer pattern is shown in Fig. 3.5(c). The optical microscope images were taken by an Axio Observer inverted microscope (Carl Zeiss) equipped with a digital color CCD camera (Infinity 2-3, Lumenera Corp.). The sample was illuminated from the backside of the quartz substrate with a halogen lamp. For the red and green color filters, the transmitted colors of the images appear to be preserved even up to the pixel size of 1 μm (the number of holes is 5 × 4 hole array for red and 6 × 6 hole array for green, Fig. 3.5(c)). For the blue color filter, the transmitted color appears to be preserved up to 3 μm pixel size, but

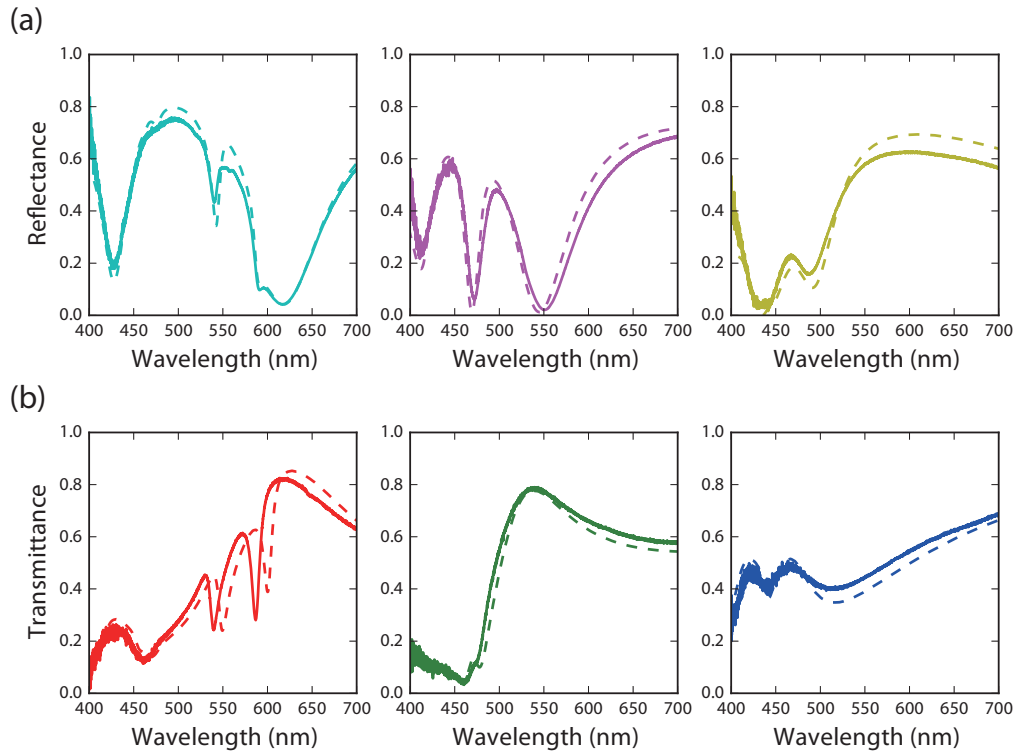


Figure 3.4: **Measurement results of visible color filters on silicon substrates with 115 nm-thick SiO_2 spacer layer or on quartz substrates.** (a) Measured reflection spectra for the designed color filters on silicon substrates with 115 nm-thick SiO_2 spacer layer. The corresponding simulated reflection spectra are also shown in dotted lines. (b) Measured transmission spectra for the designed color filters on quartz substrates. The corresponding simulated transmission spectra are also shown in dotted lines. Note that the reason that the transmission and reflection are not complementary is because the results shown in panel (a) are affected by the interference effect between the light passing through the high-index-contrast grating layer and the reflection from the underlying silicon photodiodes layer, while such interference effect does not happen in devices shown in panel (b).

exhibits a different color for the pixel size of $1 \mu\text{m}$ (the number of holes is 4×3 hole array, Fig. 3.5(c)). To understand the change in the imaged color for different filter designs, we simulated the transmission spectra for the finite size of pixels using the plane wave expansion (PWE) method. From the viewpoint of the diffraction theory, transmission through a finite sized pixel is equivalent to transmission of a set of plane waves incident from different angles through an infinite pixel. The angular distribution of the plane waves is dictated by the size and shape of the finite pixel, and the amplitude of each plane wave is modified by the transmission coefficient

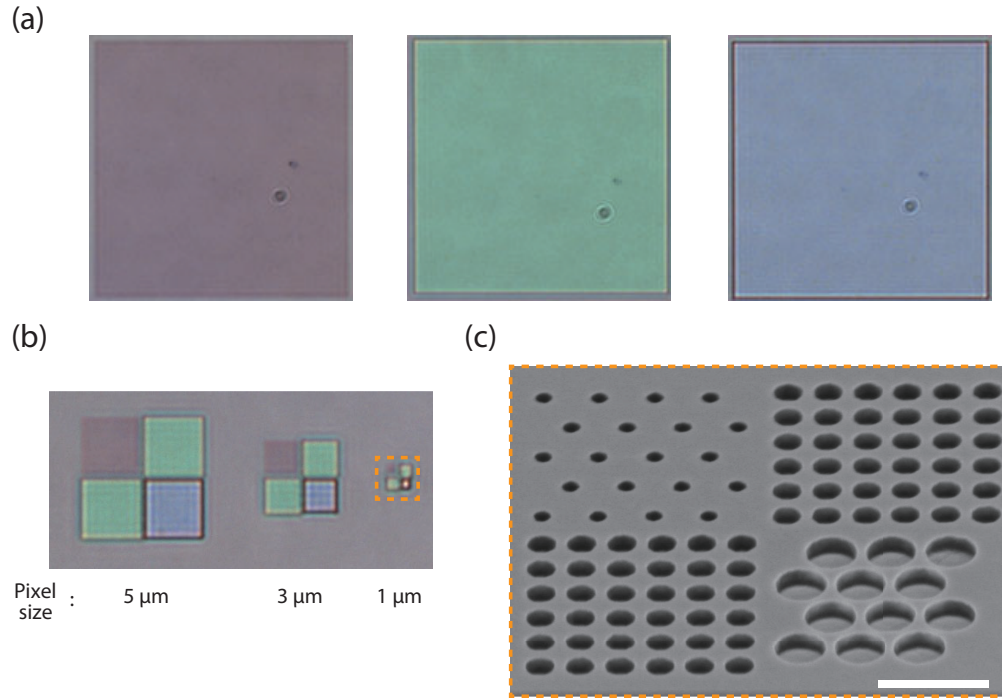


Figure 3.5: **Spectral responses for small pixel sizes of color filters.** (a) Backside-illuminated optical microscope images for the fabricated RGB color filters with large pixel size (30 μm) on quartz substrates. (b) The Bayer pattern demonstrations of small pixel size designs (5 μm , 3 μm , and 1 μm). The transmitted colors are preserved even with smaller pixel sizes. (c) The SEM image of the 1 μm -pixel color filters in the Bayer pattern, corresponding to the smallest Bayer pattern optical microscope image in (b). The scale bar is 500 nm.

of the infinite pixel. Therefore, the smaller the pixel size, the broader the angular distribution of plane waves. In other words, to preserve the color spectrum when the pixel size is w , the transmission coefficient of the periodic arrays should remain constant up to the maximum angle given by $\sin^{-1}(\lambda/w)$, the first zero of the spatial frequency spectrum of a square aperture, where λ is the wavelength of the light. This is shown in Fig. 3.6(a). To verify this, we measured the transmission spectra for the set of color filters fabricated on the quartz substrate under off-axis illuminations for 0° , 10° , 20° , and 30° . The plots are shown in Fig. 3.6(d). The measured spectra show good agreement with the RCWA-simulated spectra (also see Fig. 3.9 in Appendix). As is expected from the results of the color imaging results for the fabricated finite size pixels, the red and green filters are less angularly sensitive than the blue filter. From Fig. 3.2(c) (also see Fig. 3.7 and Fig. 3.8 in Appendix), we can see that the blue filter can be considered angularly insensitive up to $\sim 20^\circ$, indicating the

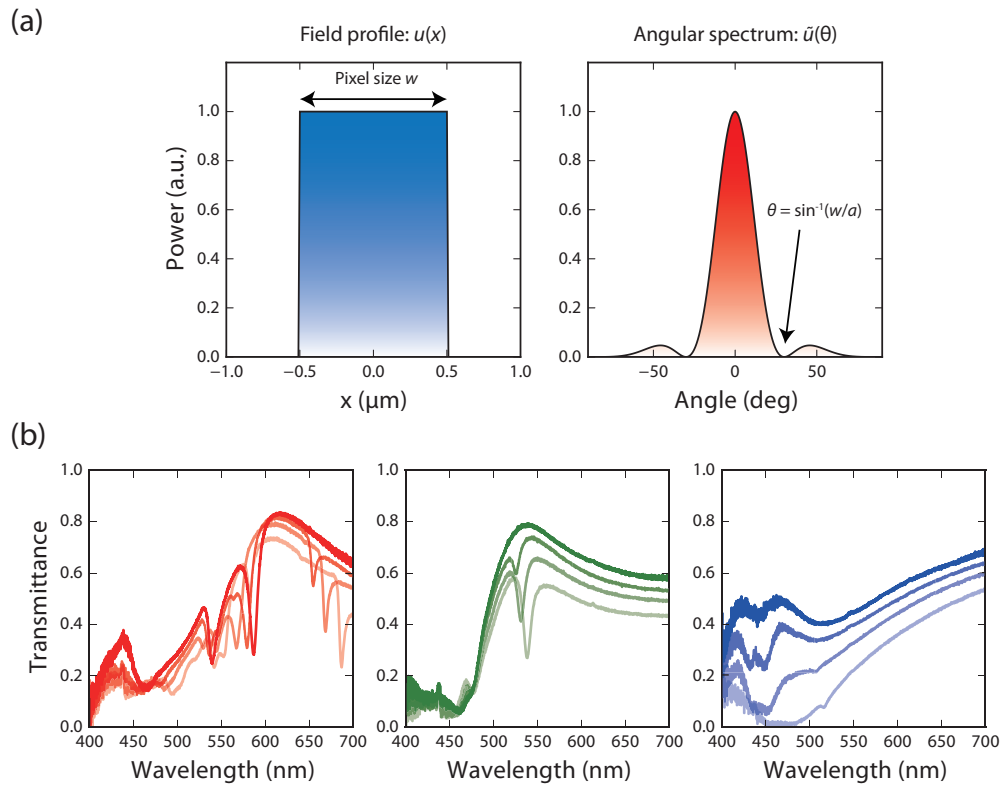


Figure 3.6: Color transmission analysis using plane wave expansion. (a) Fourier transform relation between the finite size of a pixel and its angular spectrum. (b) Measured transmission spectra of each color filter with s -polarized oblique illuminations. For each filter, transmission spectra for incidence angles of 0° , 10° , 20° , and 30° are shown with successively lighter shades (i.e., darkest is 0° , and lightest is 30°). Simulated spectra as well as p -polarized cases are shown in Fig. 3.9 in Appendix.

acceptable pixel size for the presented blue design is $w = \lambda/(\sin \theta) \sim 1.4 \mu\text{m}$ (for $\lambda = 475 \text{ nm}$), which agrees well with the optical microscope color imaging results. Since the measured filters are composed of the SWG sitting on a quartz substrate, the measured angular response for the transmission discussed so far does not include the interference effect between the light passing through the SWG layer and the reflection from the underlying silicon photodiodes layer. However, the effect of such interference on the angular response is not significant, as analyzed in Fig. 3.8 in Appendix. Therefore, the actual angular performance as well as the effect of small pixel size for the designed filter should behave similarly to the measured filters.

3.4 Summary and Outlook

We demonstrated transmissive color filters based on subwavelength dielectric gratings, optimized for the primary RGB colors for BSI-CIS technologies. The optimized set of color filters exhibits efficient peak transmittance of 60-80%, superior to plasmonic color filters, owing to the combination of high refractive index contrast and relatively low loss in poly-Si. We also studied the effect of finite size pixels, comparable to the pixel size available in state-of-the-art CIS technologies, in conjunction with the angular response of the infinite array of the structures and found that the designed filters preserve their colors down to near a micrometer. We note that the proposed dielectric grating color-filters are highly customizable and compatible with micrometer and submicrometer pixel sizes, when considering new image processing methods such as an RWB (red, white, blue) matrix. To make the filter fabrication more compatible with the CMOS backend processes, a pulsed laser annealing process [86] may be used for preparing low-loss poly-Si layers as low temperature alternative methods, instead of the high temperature annealing method. Furthermore, by exploiting the freedom of designing spatially varying phase, amplitude, and polarization of the transmission [4, 11, 12, 15, 16] that SWGs are capable of, not only the conventional dye-doped color filters but also the microlenses on top of CIS pixels could be replaced in one layer of dielectric SWG on top of silicon photodiodes layers.

Appendix

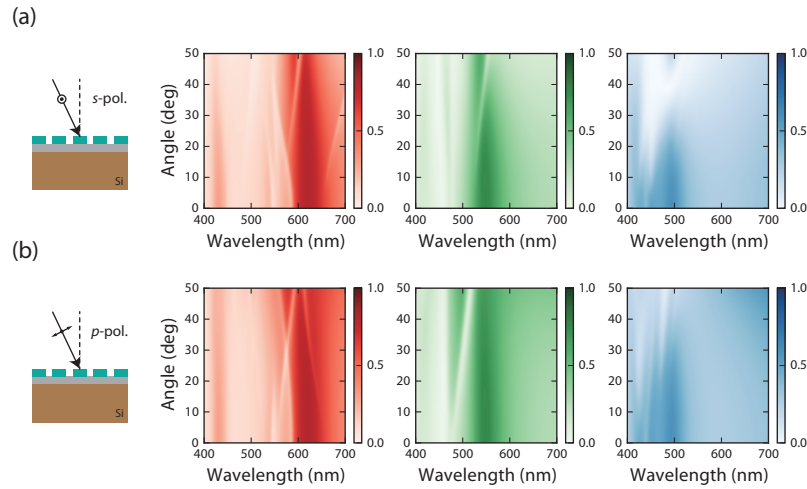


Figure 3.7: **RCWA simulations of the angular dependence of the transmission spectra for (a) *s*- and (b) *p*-polarized light.** See Fig. 3.2(c) for unpolarized light.

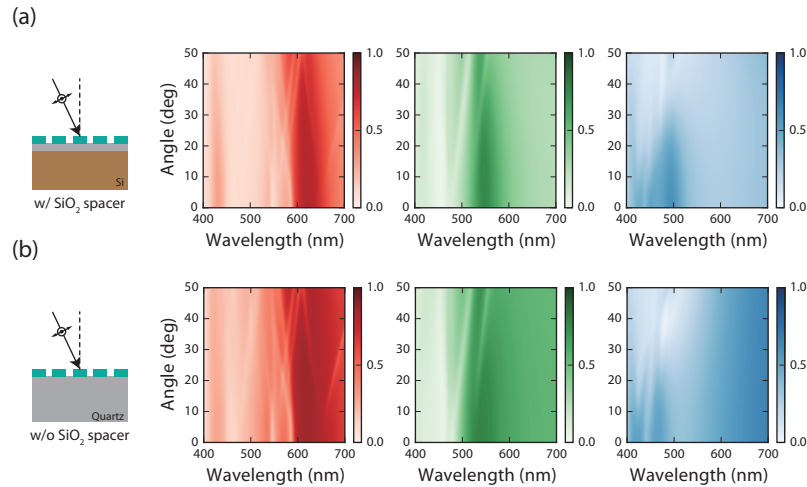


Figure 3.8: **RCWA simulations of the angular dependence of the transmission spectra under unpolarized light illumination for the two cases: (a) with and (b) without SiO₂ spacers.** The figures indicate that the angular dependence mainly arises from the angular response of the SWG layer, and that the effect of interference on the angular response is not significant.

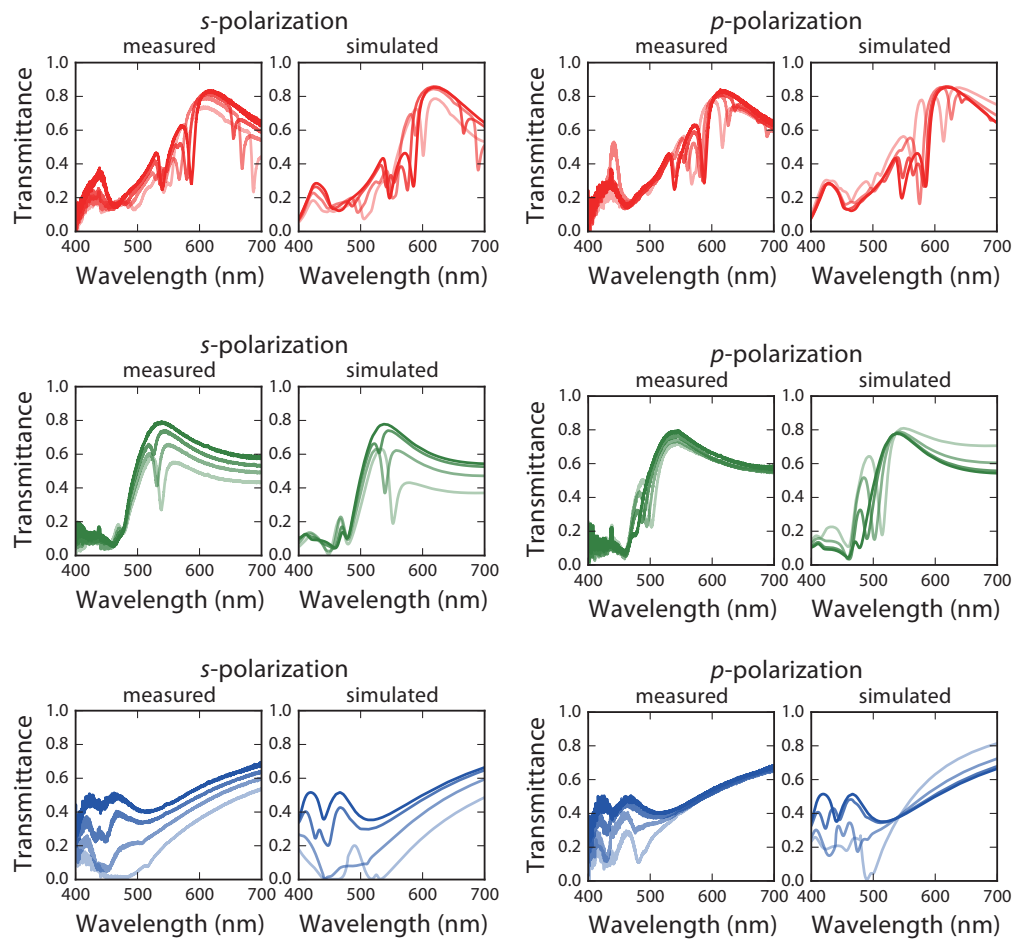


Figure 3.9: **Measured (left) and simulated (right) transmission spectra of each color filter under oblique illuminations with *s*- and *p*-polarized light.** For each filter, transmission spectra for incidence angles of 0° , 10° , 20° , and 30° are shown with successively lighter shades.

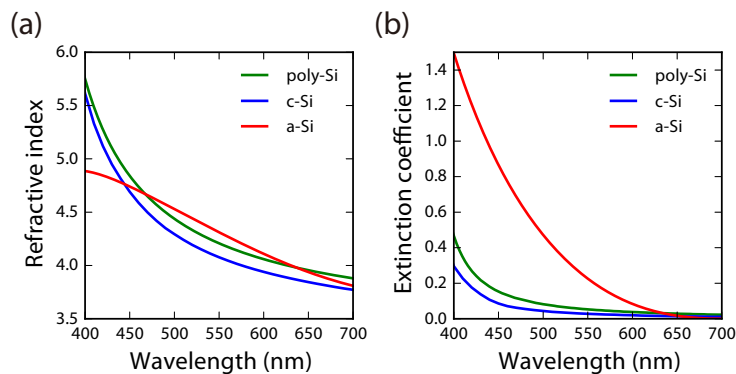


Figure 3.10: **Refractive index of poly-Si in the visible wavelength.** (a) Refractive indices and (b) extinction coefficients of poly-Si (measured), crystalline silicon [87], and α -Si (measured).

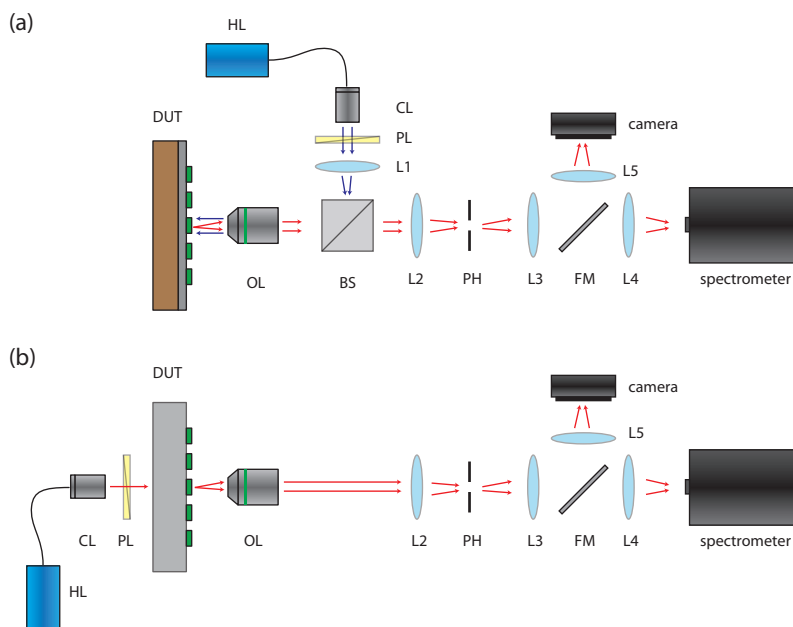


Figure 3.11: **Measurement setups.** (a) The measurement setup used to obtain reflection spectra for the color filters on the silicon wafer. (b) The measurement setup used to obtain transmission spectra for the color filters on the quartz wafer. (HL: Halogen lamp, PL: polarizer, CL: collimator lens, OL: objective lens, DUT: device under test, L: lens, PH: pinhole, BS: beam splitter, and FM: flippable mirror).

HIGH-SPEED, PHASE-DOMINANT SPATIAL LIGHT MODULATION WITH SILICON-BASED ACTIVE RESONANT ANTENNAS

The material in this chapter was presented in part in:

Y. Horie, A. Arbabi, E. Arbabi, S. M. Kamali, and A. Faraon, “High-speed, phase-dominant spatial light modulation with silicon-based active resonant antennas”, (under submission),

Spatiotemporal control of optical wavefronts is of great importance in numerous free-space optical applications including imaging in 3D and through scattering media, remote sensing, and generation of various beam profiles for microscopy. Progress in these applications is currently limited because of lack of compact and high-speed spatial light modulators (SLMs). In this chapter, we report an active antenna comprising a free-space coupled asymmetric Fabry–Perot resonator, that produces a phase-dominant thermo-optic modulation of reflected light at frequencies approaching tens of kilohertz. As proof of concept for spatial light modulation, we demonstrate a 6×6 array of such active antennas with beam deflection capability. The robust design of our silicon-based active antenna will enable large-scale integration of high-speed, phase-dominant SLMs.

4.1 Motivation

An SLM is an optoelectronic device that imposes a spatially varying modulation on a beam of light [88]. Particularly, spatiotemporal control of the wavefront (i.e., phase) of light is of great importance for a wide range of applications including beam steering, imaging, holography, optical tweezers, and remote sensing. However, the absence of compact and inexpensive SLMs that can freely modulate the wavefront of light at a high speed is hindering the widespread adoption of popular technologies such as light detection and ranging (LiDAR) [89] and *in-vivo* wavefront correction in biomedical imaging [90]. The liquid crystal on silicon is the most mature technology used for SLMs that showcases several advantages such as no moving parts, low

power consumption, and established manufacturing processes [91]. Nonetheless, nematic liquid crystals, which are most commonly used, suffer from a slow response time of tens to hundreds of milliseconds. Ferroelectric liquid crystals show sub-milliseconds response time, but operate only in a binary phase modulation owing to the bistable nature of the material [92]. Stressed liquid crystals can provide a sub-millisecond control with continuous phase modulation [93]; however, their mass production is not feasible due to the requirement of delicate mechanical shearing process. On the other hand, microelectromechanical systems (MEMS) based movable micro-mirrors, known as digital micro-mirror device (DMD) technology [94], offer faster spatial light modulation typically at 10 kHz [95]. However, they only operate in a binary amplitude mode resulting from sophisticated device structures, and complex fabrication processes make them less attractive for mass-production. Recently, MEMS-based tunable all-pass filters that use light-weight high-contrast subwavelength grating (SWG) reflectors in a Gires–Tournois interferometer configuration [34] have been demonstrated. The low mass of the SWG reflectors has increased the modulation speed of these devices to over 500 kHz.

In this chapter, we demonstrate a high-speed silicon-based active resonant antenna involving no moving parts, as a basic device element for phase-dominant spatial light modulation. The individual silicon antenna, made of an asymmetric Fabry–

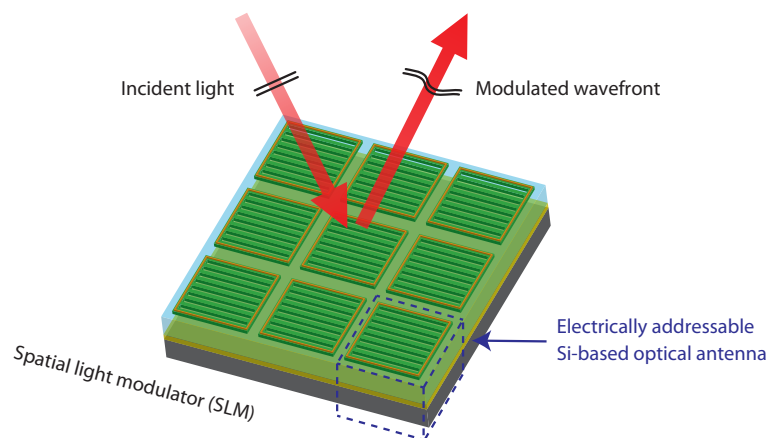


Figure 4.1: **Concept of a phase-dominant spatial light modulator with silicon-based active resonant antennas.** Schematic illustration of the SLM, where the active antenna is made of an optical resonator consisting of a silicon SWG layer and a DBR layer.

Perot resonator formed by a silicon SWG reflector and a DBR exhibits nearly 2π phase-dominant modulation as fast as tens of kHz range by means of the silicon's thermo-optic effect at telecom wavelengths. As a proof of concept for spatial light modulation, a 6×6 array of such antennas is actively controlled, yielding a phased array beam deflection capability.

4.2 Design of an Active Resonant Antenna

The spatial light modulation scheme composed of the silicon-based active antenna array is illustrated in Fig. 4.1, in which each antenna has an independent electrical control over the phase of the reflected light. The individual optical antenna comprises an asymmetric Fabry–Perot resonator [26, 96] as shown in Fig. 4.2(a,c), whose amplitude and phase response with respect to the laser frequency can be described with the temporal coupled-mode theory [25].

Coupled-Mode Theory with One Port

We will first formulate the reflection coefficient through a resonator with one port to analyze the phase response required for phase-dominant modulation. Let us consider a resonator, which has a decay rate $1/\tau_i$ due to the intrinsic loss, excited by an input wave in the form of a waveguide. The presence of the excitation waveguide modifies the decay rate of the resonator because it also allows the energy in the resonator to escape into the waveguide. This can be expressed by another decay rate $1/\tau_e$. The waveguide may carry a wave driving the field in the resonator. In this case, we can write the couple-mode equation,

$$\frac{da_c}{dt} = i\omega_0 a_c - \left(\frac{1}{\tau_i} + \frac{1}{\tau_e} \right) a_c + \sqrt{\kappa_e} s^+, \quad (4.1)$$

where a_c is the normalized energy amplitude of the resonator mode, ω_0 is the resonance frequency, $\sqrt{\kappa_e}$ is the coupling rate from the waveguide into the resonator, and s^+ is the power amplitude of the input waveguide mode that acts as a source. If the source has a frequency ω (i.e., $s^+ \propto \exp(j\omega t)$), then the energy amplitude of the resonator is

$$a_c = \frac{\sqrt{\kappa_e} s^+}{i(\omega - \omega_0) + (1/\tau_i + 1/\tau_e)}. \quad (4.2)$$

Because the decay rate $1/\tau_e$ is due to the coupling between the waveguide, it has something to do with the coupling rate $\sqrt{\kappa_e}$. We will relate these coefficients using the time-reversal property. If we consider no intrinsic loss in the resonator ($1/\tau_i = 0$) and no excitation from the waveguide ($s^+ = 0$), the resonator decays its energy at the

rate $1/\tau_e$ due to the presence of the waveguide:

$$\frac{d}{dt} |a_c|^2 = -\frac{2}{\tau_e} |a_c|^2 = -|s^-|^2. \quad (4.3)$$

When the system is time-reversed, the energy in the resonator will build up due to the excitation from the waveguide:

$$\frac{d}{dt} |\tilde{a}_c|^2 = +\frac{2}{\tau_e} |\tilde{a}_c|^2 = |\tilde{s}^+|^2, \quad (4.4)$$

where \tilde{a}_c denotes the time-reversed solution and has a negative frequency term ($\exp(-j\omega t)$). In the time-reversed case, we can interpret that the incident wave \tilde{s}^+ drives the resonator at a complex frequency:

$$\omega = \omega_0 - \frac{i}{\tau_e}. \quad (4.5)$$

Plugging this into Eq. (4.2) gives us

$$\tilde{a}_c = \frac{\sqrt{\kappa_e}}{2/\tau_e} \tilde{s}^+. \quad (4.6)$$

Comparing Eq. (4.4) and Eq. (4.6) leads to the important relation

$$|\kappa_e| = \frac{2}{\tau_e}, \quad (4.7)$$

where the phase of $\sqrt{\kappa_e}$ can be omitted by absorbing it by s^+ . Therefore, we can rewrite the Eq. (4.1) with the time constants

$$\frac{da_c}{dt} = i\omega_0 a_c - \left(\frac{1}{\tau_i} + \frac{1}{\tau_e} \right) a_c + \sqrt{\frac{2}{\tau_e}} s^+, \quad (4.8)$$

or we can also write it in terms of the decay rates

$$\frac{da_c}{dt} = i\omega_0 a_c - \frac{\kappa}{2} a_c + \sqrt{\kappa_e} s^+, \quad (4.9)$$

where κ is the total decay rate of the resonator defined as $\kappa = \kappa_i + \kappa_e$, and likewise we can define the intrinsic decay rate of the resonator by $\kappa_i = 2/\tau_i$.[†]

We can also develop the equation relating the reflected wave with the excitation waveguide and the resonator, which allows to derive the reflection coefficient:

$$s^- = C_s s^+ + C_a a_c, \quad (4.10)$$

[†]The intrinsic quality factor (Q -factor) can be defined as $Q_i = \omega_0 \tau_i / 2 = \omega_0 / \kappa_i$. The external Q -factor can be defined as $Q_e = \omega_0 \tau_e / 2 = \omega_0 / \kappa_e$. The loaded Q -factor then becomes $Q = (Q_e^{-1} + Q_i^{-1})^{-1}$.

in which we want to determine the coefficients C_s and C_a . From Eq. (4.3), we have $C_a = \sqrt{2/\tau_e}$. The other coefficient C_s can be evaluated by the energy conservation. That is, using the fact that the net power flowing into the resonator from the waveguide must be equal to the rate of energy buildup added to the power dissipation,

$$|s^+|^2 - |s^-|^2 = \frac{d}{dt} |a_c|^2 + \kappa_i |a_c|^2. \quad (4.11)$$

On the other hand, from Eq. (4.8), we have

$$\begin{aligned} \frac{d}{dt} |a_c|^2 &= \frac{da_c}{dt} a_c^* + a_c \frac{da_c^*}{dt} \\ &= \left(i\omega_0 a_c - \frac{\kappa}{2} a_c + \sqrt{\kappa_e} s^+ \right) a_c^* + a_c \left(-i\omega_0 a_c^* - \frac{\kappa}{2} a_c^* + \sqrt{\kappa_e} s^{+*} \right) \\ &= -\kappa |a_c|^2 + \sqrt{\kappa_e} \left(a_c^* s^+ + a_c s^{+*} \right), \end{aligned} \quad (4.12)$$

and combining Eq. (4.11) and Eq. (4.12) leads to

$$|s^+|^2 - |s^-|^2 = -\kappa_e |a_c|^2 + \sqrt{\kappa_e} \left(a_c^* s^+ + a_c s^{+*} \right). \quad (4.13)$$

Likewise, with Eq. (4.10), we find that

$$|s^-|^2 = C_s^2 + |s^+|^2 + \kappa_e |a_c|^2 + C_s \sqrt{\kappa_e} \left(a_c^* s^+ + a_c s^{+*} \right). \quad (4.14)$$

By comparing Eq. (4.13) and Eq. (4.14), we finally obtain $C_s = -1$. Therefore, Eq. (4.10) becomes

$$s_- = -s_+ + \sqrt{\kappa_e} a_c. \quad (4.15)$$

Equation (4.9) and (4.15) are the fundamental equations describing a resonator system with one port (either in the form of waveguide or free-space mode). Now we can calculate the reflection coefficient as a function of driving frequency. Then, we can compute the reflection coefficient spectrum $r(\Delta)$ through the resonance system:

$$r(\Delta) \equiv \frac{s^-}{s^+} = \frac{-i\Delta + \frac{\kappa_e}{2} - \frac{\kappa_i}{2}}{i\Delta + \frac{\kappa_e}{2} + \frac{\kappa_i}{2}}, \quad (4.16)$$

where Δ is the frequency detuning defined as $\Delta \equiv \omega - \omega_0$. The graphical representation of complex plane $r(\Delta)$ is depicted in Fig. 4.3. Figure 4.2(b) shows the reflectivity spectra as well as their phase curves as a function of frequency detuning Δ , normalized by κ in two cases; over-coupled ($\kappa_e > \kappa_i$) and under-coupled ($\kappa_e < \kappa_i$) conditions. The power reflection loss at an on-resonance frequency is dependent on the decay rates of the resonator:

$$\Gamma_{\text{loss}} = \left(\frac{\kappa_e - \kappa_i}{\kappa_e + \kappa_i} \right)^2. \quad (4.17)$$

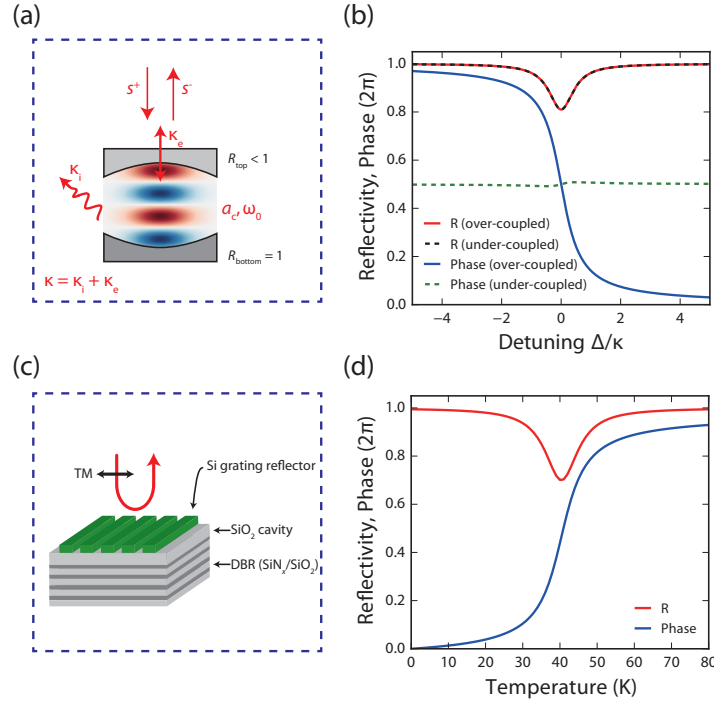


Figure 4.2: **Design of active resonant antenna using the temporal coupled-mode theory.** (a) Schematic of an optical resonator system coupled with one port. (b) Reflectivity spectra as well as phase curves as a function of frequency detuning Δ , normalized to the total decay rate κ , calculated using the temporal coupled-mode theory. The results for over-coupled ($\kappa_e/\kappa = 0.95$) and under-coupled ($\kappa_e/\kappa = 0.05$) are plotted. (c) Design of the over-coupled resonator realized by a silicon SWG layer on top of a DBR. (d) Simulated reflectivity change as well as phase response as a function of change in the temperature variation in the silicon bars, resulting in the refractive index modulation of silicon. The incident is assumed to be a continuous-wave laser light at a wavelength of 1550 nm. The simulation results were calculated by the RCWA technique [28].

The reflection loss can be minimized by decreasing κ_i , leading to phase modulation with small amplitude variation. The reflection phase spectrum exhibits nearly 2π rapid phase shift around the resonance frequency only when a resonator is over-coupled, whereas the phase shift is very small in the case of an under-coupled resonator. If the resonance frequency of the over-coupled resonator can be tuned by some means, the modulation of the resonance frequency will manifest itself as a phase-dominant modulation for the reflected light.

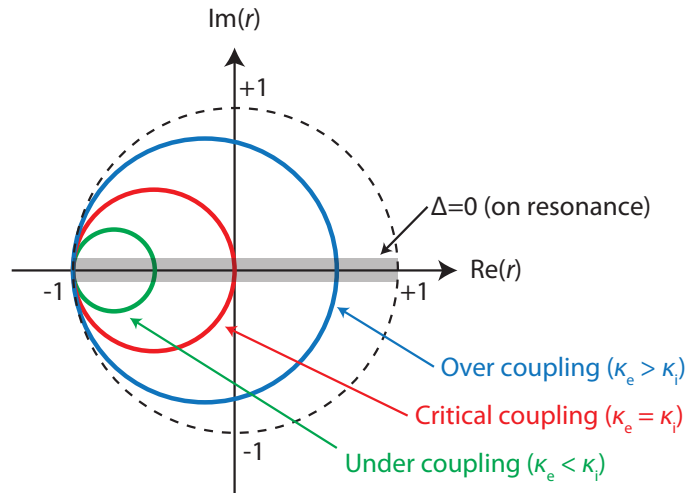


Figure 4.3: **Graphical representation of the reflection coefficient in a resonator system with one port.** The phase of reflection is the angle in the complex plane. Only in the over coupling condition, we can obtain a nearly 2π phase shift across the resonance.

Implementation of an Over-Coupled Resonator System

To implement such a phase-modulation scheme, we design a free-space coupled Fabry–Perot resonator comprising a high-contrast SWG reflector [1, 7, 11, 22, 23] made of high-index amorphous silicon (α -Si) bars located on a high reflectivity DBR made of a quarter-wave stack of silicon nitride (SiN_x) and silicon dioxide (SiO_2) (Fig. 4.2(c)). This is equivalent to a conventional Gires–Tournois interferometer, with a bottom mirror exhibiting nearly unity reflectivity and a less reflective top mirror, that is widely used for pulse compression because of its highly dispersive phase response. Owing to the high electric-field accumulation in the silicon SWG layer when used in a Fabry–Perot resonator [97], the resonance frequency can be efficiently tuned with respect to the wavelength of the incident light by modulating the refractive index of the silicon bars. The large thermo-optic coefficient of α -Si ($dn/dT \approx 2 \times 10^{-4} / \text{K}$) [98] can be practically used by integrating a microheater around the device but far enough from the area of the optical resonator to avoid absorption loss. Figure 4.2(d) shows the simulated phase modulation as well as the reflectivity change for a TM-polarized (i.e., electric field perpendicular to the grating bars) normally incident light as a function of the temperature change in the α -Si bars resulting in the refractive index modulation of α -Si. Using the temporal coupled-mode theory results, the coupling rate κ_e is related to the reflection coefficient

of the top SWG reflector. The intrinsic decay rate κ_i accounts for the losses of the resonator such as transmission through the bottom reflector, scattering loss due to the surface roughness, and lateral energy leakage due to the finite extent of the optical mode. It should be noted again that nearly 2π phase modulation is achieved under the over-coupled resonator condition $\kappa_e > \kappa_i$ (i.e., coupling rate of the antenna to the free-space mode has to be greater than the total intrinsic decay rate).

4.3 Phase-Dominant Modulation with a Single Antenna

Device Fabrication

For silicon-based active antenna fabrication, we started with a 675- μm -thick silicon substrate. We deposited the DBR structure with 12 pairs of $\text{SiN}_x/\text{SiO}_2$ quarter-wave stacks (195 nm and 258 nm in thicknesses, respectively) at 350°C using plasma-enhanced chemical vapor deposition (PECVD) method. Then, a 415-nm-thick SiO_2 and a 435-nm-thick α -Si layer were deposited at 200°C also by PECVD. The top α -Si layer was then patterned by electron beam lithography and dry etched in a mixture of SF_6 and C_4F_8 plasma, to form the top silicon SWG reflector (period: 675 nm, width: 430 nm, height: 435 nm). 100 nm-thick, 1 μm -wide NiCr heaters surrounding the antennas were then patterned using a lift-off process, and subsequently Au contact pads were fabricated. An scanning electron microscope (SEM) image of a single element of the fabricated active silicon antenna with the integrated microheater made of nichrome (NiCr) is shown in Fig. 4.4(a).

Optical Measurement Procedure

For optical measurements, including reflectivity spectra from single active antennas and far-field patterns, we used a custom-built confocal microscope setup illustrated in Fig. 4.6 in Appendix. A continuous-wave laser light emitted from a tunable external cavity laser diode (Photonetics, TUNICS-Plus) was collimated using a fiber collimation package (Thorlabs, F260FC-1550). A polarizing beamsplitter (PBS), a half waveplate (HWP), and a quarter waveplate (QWP) were inserted to set a desired polarization state of the incident light. The device was illuminated with a beam whose profile has a Gaussian beam waist of 75 μm on the device. The reflected field was imaged by a pair of a 20 \times infinity-corrected objective lens (Mitutoyo, M Plan Apo NIR) and a tube lens with a focal length of 200 mm onto a pinhole with a diameter of 400 μm to select a region of interest with diameter of 20 μm in the object plane. The spatially filtered light was either focused onto an InGaAs

detector (Thorlabs, PDA10CS) for the measurement of the reflectivity spectra by scanning the source wavelength, or imaged on an InGaAs SWIR camera (Goodrich, SU320HX-1.7RT) for both the near-field and the far-field measurements using relay optics. For the measurement of temporal responses, the bias voltages, both DC and AC, were applied with a function generator (Stanford Research System, DS345).

Phase Measurement in a Cross-Polarized Setup

For the reflection phase measurement, we inserted a QWP and a HWP between the PBS and the antenna (see Fig. 4.6 in Appendix). The waveplates were used to convert the linearly polarized beam into an elliptically polarized beam with electric-field components parallel and orthogonal to the resonance of the antenna. Only the parallel component (TM-polarization) can acquire a drastic phase shift due to the antenna resonance, while the orthogonal component (co-propagating TE-polarization) does not. The detected light intensities through the PBS are the results of interference between those two components:

$$I_{\text{out}}(\lambda, \theta) = |E_{\text{out}}(\lambda, \theta)|^2 = |A(\theta)[-r_c(\lambda) + B(\theta, r_0)]|^2, \quad (4.18)$$

where θ is the QWP angle, and r_c and r_0 are the reflection coefficients for TM- and TE-polarized light, respectively. The HWP angle is fixed at 22.5° relative to the vertical polarization of the PBS. We also have

$$A(\theta) = 1 + \cos(4\theta) + 2i \sin(2\theta), \quad (4.19)$$

$$B(\theta, r_0) = r_0 \left(\frac{1 + \cos(4\theta) - 2i \sin(2\theta)}{1 + \cos(4\theta) + 2i \sin(2\theta)} \right). \quad (4.20)$$

By measuring I_{out} for different θ and fitting the data with the equations, the reflection phase can be determined.

Characterization Results of a Single Antenna

We measured reflectivity spectra of the fabricated antenna for a normally incident TM-polarized beam using a custom-built confocal microscope setup by scanning a tunable laser (see Fig. 4.6 in Appendix for the detailed measurement setup) as shown in Fig. 4.4(b). By fitting the reflectivity spectra with Eq. (4.16), we found that the measured loaded Q -factor ($Q \equiv \omega_0/\kappa$) of the resonance was around 1.9×10^2 (the intrinsic Q_i was around 1.1×10^3) at 1525 nm and the maximum loss at resonance was approximately 58%. The over-coupled condition ($\kappa_e > \kappa_i \Leftrightarrow Q_e < Q_i$) was determined by the phase measurement later on. Passing a DC current through the integrated microheater, we confirmed the resonance wavelength tunability owing to

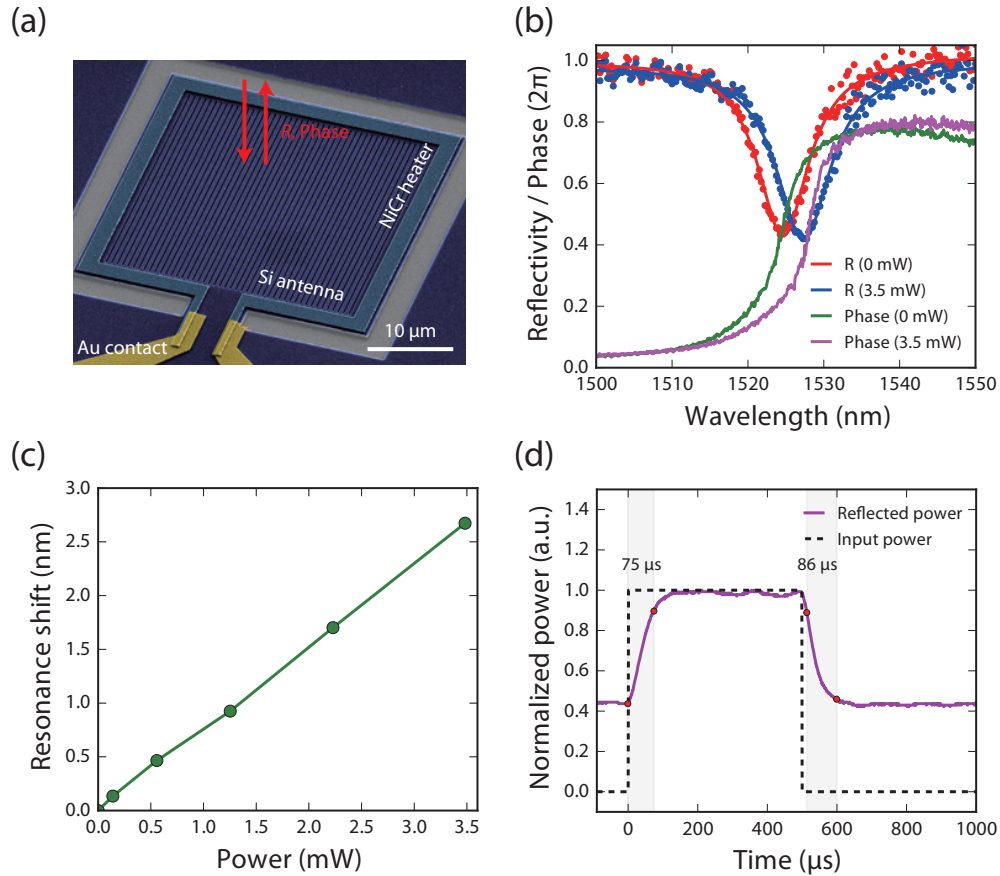


Figure 4.4: **Characterization results of a single active antenna.** (a) False-color SEM image of a fabricated single-pixel silicon antenna (pixel size: $20\ \mu\text{m}$) with a NiCr microheater as well as Au contacts. (b) Measured reflectivity spectra of the antenna and the extracted phase curves. The dispersive phase shift $\sim 1.6\pi$ indicates that the resonance satisfies the over-coupling condition. The required electrical power to introduce π phase shift P_π was found to be $3.5\ \text{mW}$. (c) Measured resonance wavelength tunability by means of silicon's thermo-optic effect, indicating high thermal efficiency of about $0.77\ \text{nm/mW}$. (d) Temporal response of the silicon active antenna, characterized by the modulated optical output power of the reflected light. The measured response time is about $70\ \mu\text{s}$. The dashed line indicates a $1\ \text{kHz}$ square-wave applied across the microheater with an input power of P_π .

the thermo-optic effect of α -Si without degrading the optical resonance. Figure 4.4(c) shows the resonance wavelength shift as a function of electrical power injected into the NiCr microheater with measured resistance of $\sim 7.2 \times 10^3 \Omega$, indicating high thermal efficiency of about 0.77 nm/mW, benefiting from the high thermo-optic coefficient of silicon. Next, we measured the reflected phase using a cross-polarization setup, in which the phase of reflected TM-polarized beam of interest was extracted by interfering it with a co-propagating TE-polarized beam, which does not couple to the antenna (see Methods as well as Fig. 4.7) in Appendix. After fitting the measured intensities with a theoretical model, the reflected phase curves were computed as shown in Fig. 4.4(b). A phase change $\sim 1.6\pi$ across the resonance wavelength was observed, implying the resonance was over-coupled as we intended. The required electrical power to introduce π phase change P_π was 3.5 mW. We also investigated response times of the phase modulation shown in Fig. 4.4(d) when 1 kHz square-wave electrical signal modulated the antenna with P_π . The rise and fall response times of 74 μ s and 66 μ s were observed, which are in good agreement with the simulated values (see Fig. 4.8 in Appendix for the simulated response times). The response time is defined as the time duration by which the normalized optical power rises (or falls) from 10% to 90% (or vice versa) of the steady-state when an input signal modulates the microheater.

4.4 Demonstration of Phased Array Beam Deflection

As a proof of concept for spatial light modulation, a 6×6 array of active silicon antennas was fabricated (Fig. 4.5(a)). Since the pixel pitch of the array is 26 μ m, while the pixel size of the antenna is 20 μ m, the fill factor of the phased array is $\sim 59\%$. For the sake of simplicity, the microheaters around the antennas were grouped in every other column and addressed by a single input, such that the entire phased array displays an alternating phase pattern between the neighboring pixels. From the reflectivity measurements, each of the fabricated antennas in the array exhibited relatively small fluctuations in the resonance wavelengths with standard deviation of 0.44 nm among the antennas that are negligible compared with the FWHM of the resonance. Figure 4.5(b) shows the simulated temperature distribution of the device surface when only the central pixel is active, indicating the designed microheaters can individually address the pixels with some thermal crosstalk of 8% measured by the temperature change in the center of the pixels. The far-field patterns of the phased array were measured by imaging the back focal plane of the objective

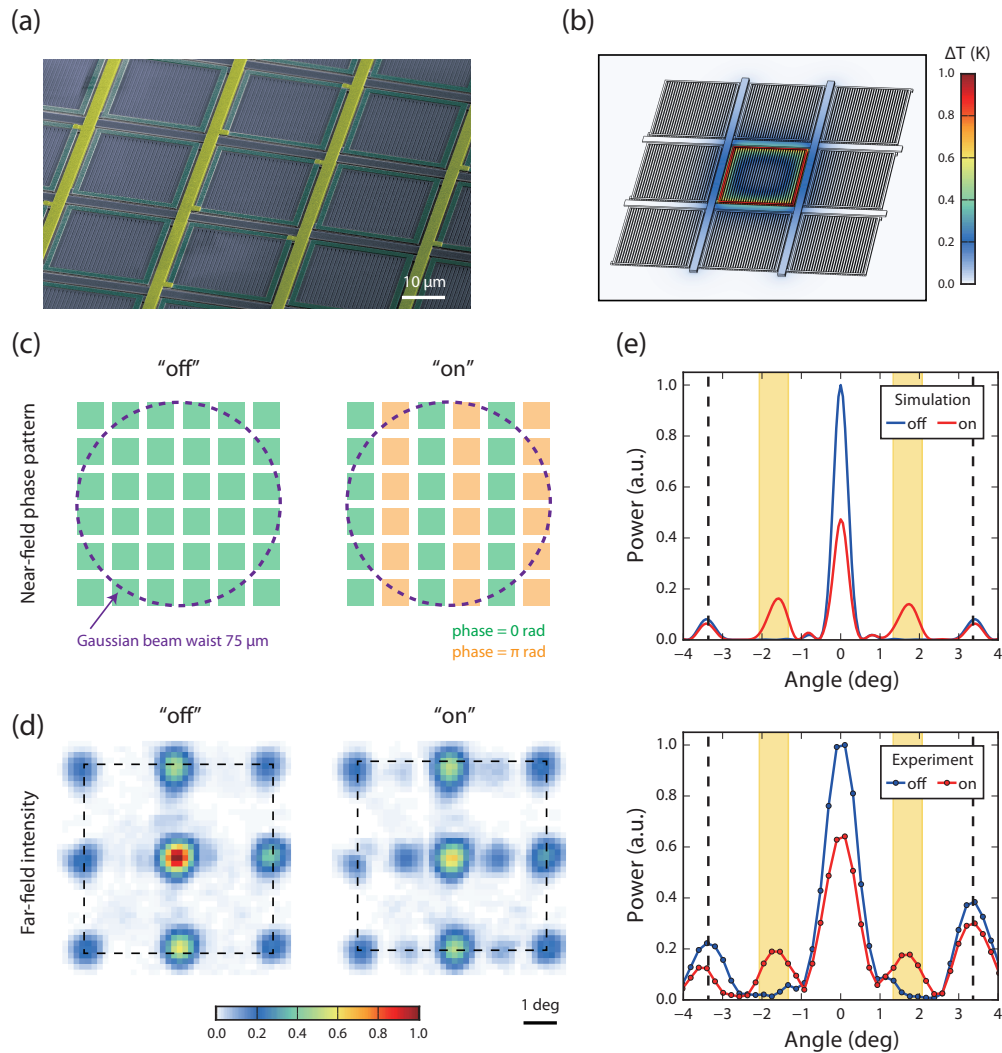


Figure 4.5: **Experimental demonstration of phased array beam deflection.** (a) SEM image of a fabricated phased array. (b) Temperature distribution of the surface of the silicon antenna array found using FEM simulation. (c) Intended near-field phase profile for two states: "off" and "on". The array is illuminated with an incident Gaussian beam profile with a beam waist of 75 μm. (d) Measured far-field patterns for the two states: "off" and "on". The dashed box indicates the ±1st order diffraction angles imposed by the pixel pitch. (e) Corresponding 1-D profiles of the far-field patterns along the deflection direction by the simulation (top) and the experiment (bottom). The deflected beam appeared at the angles $\theta = \pm\theta_{\max} = \pm 1.7^\circ$ as denoted by the yellow shades including the Gaussian divergence half angle of 0.37° . Again, the dashed line corresponds to the angles of the ±1st diffraction orders.

lens. The result of the beam deflection is shown in Fig. 4.5(c) together with the corresponding near-field phase patterns. The strong diffraction pattern can be seen in the far-field pattern when no voltage is applied (“off” state), due to the low fill factor of the phased array. When the voltage was tuned to introduce π phase shift in every column (“on” state; electrical power $P = 18P_\pi$ was applied), the phased array beam deflection was observed at the angle given by $\theta_{\max} = \sin^{-1}(\lambda/2p) \approx 1.7^\circ$, where λ is the wavelength of the light and p is the pixel pitch of the phased array, in reasonably good agreement with the measured angle. Figure 4.5(d) shows the 1-D profiles of the measured far-field patterns, in good agreement with simulated patterns, which confirms the robustness of the proposed device design. The beam deflection efficiency measured as the ratio between the total of ± 1 st order deflected beams and that of the undiffracted beam was about 40% at best, which wouldn’t be possible with amplitude-only modulation (see Fig. 4.9 in Appendix).

4.5 Discussion

The demonstrated response time in phase modulation is currently dominated by the large thermal resistance between the α -Si SWG layer and the silicon substrate, owing to the low thermal conductivities of the $\sim 6\text{-}\mu\text{m}$ -thick DBR layers. Substituting the material for a good thermal conductor (e.g. polycrystalline silicon or GaAs/AlGaAs-based DBR) or thinning the DBR layers should greatly improve the response time [99]. As a point of reference, sub-microseconds response was reported by means of direct heating of silicon waveguides in the context of an on-chip Mach–Zehnder interferometer, where the buried oxide layer in a silicon-on-insulator substrate was $1\text{ }\mu\text{m}$ [100]. Even further improvement of the modulation speed as fast as up to hundreds of MHz can be expected by deploying the same device design but comprising p-i-n structure along the silicon bars using the plasma dispersion effect [101–103] or the Kerr effect [104]. However, in this case, one would need an optical resonance with much higher Q -factor, as those modulation methods can practically achieve q refractive index change on the order of 10^{-4} , an order of magnitude smaller than the one achievable via thermo-optic effect. The pixel pitch and the fill factor are also important parameters in spatial light modulation. The former imposes a limit on the maximum spatial frequency or deflection angle [105], and the latter leads to beam deflection efficiency loss as it contributes to the undiffracted components. In our scheme, if we reduce the size of antenna, the number of SWG bars in a pixel will be lower, and additional loss will be induced due to the lack of lateral mode confinement

[106]. This can be circumvented by several approaches including the effective index method [58] and the phase gradient mirror approach [59], to further shrink the size of the antennas. Alternatively, even without having a smaller pixel pitch, one can think of enlarging the deflection angle limit using appropriate magnification optics to access a larger spatial frequency. The proposed phased array scheme can be immediately extended to use advanced electrical circuitry schemes such as an active matrix addressing to independently control the enormous number of pixels or vertical integration of wiring layers to maximize the fill factor of the pixels.

4.6 Summary and Outlook

In summary, we demonstrated a silicon-based active antenna based on an over-coupled optical resonator system, where the phase modulation for the light propagating in free space is achieved via the refractive index modulation of silicon. The fabricated active antenna exhibits phase-dominant thermo-optic modulation with a response time of $\sim 70 \mu\text{s}$, an order of magnitudes faster than the conventional liquid crystal based SLMs. A phased array beam deflection was demonstrated with a 6×6 array of such active antennas. The demonstrated design can be easily integrated in a scalable fashion using conventional complementary metal oxide transistor (CMOS) technology (e.g. silicon photonics [107, 108]), allowing large-scale phase-dominant SLMs to be implemented on inexpensive and compact photonic chips. As such, the presented spatial light modulation device will enable cost-effective beam steering solutions for LiDAR and *in-vivo* biomedical imaging applications.

Appendix

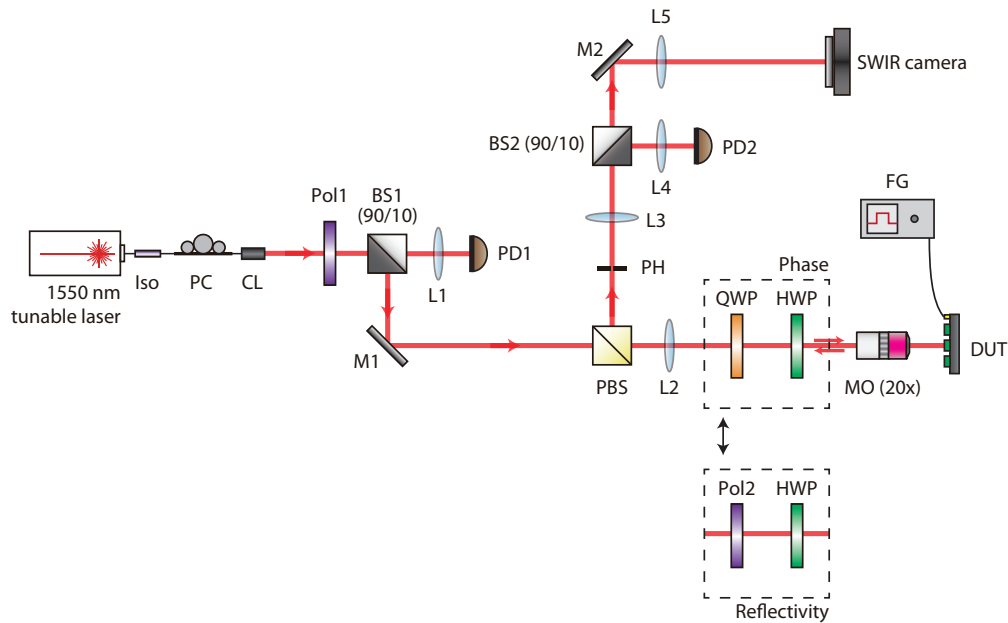


Figure 4.6: **Experimental setup to characterize an optical antenna as well as phased array.** A continuous-wave laser emitted from a tunable external cavity laser diode was used as a light source for the measurements. After transmitting through the PBS, the laser beam was demagnified by a lens (L2, focal length: 200 mm) and a 20× microscope objective (MO), resulting in a Gaussian beam waist of 75 μm on the object plane. The reflected light was then imaged by the same lenses onto a pinhole with diameter of 400 μm to select the region of interest with corresponding diameter of 20 μm in the object plane. After the PH, the intensity was measured onto PD2 using a lens pair of L3 and L4, while the image was monitored at a SWIR camera by a lens pair of L3 and L5. For the reflectivity measurement, a polarizer and a HWP were inserted in the path, where the angle of polarizer was set to 45° with respect to the axes of the PBS. For the phase extraction measurement, a QWP was inserted in place of the polarizer in order to make the incident polarization state being elliptical. Iso: optical isolator. PC: polarization controller. CL: collimation lens. Pol: polarizer. BS: beamsplitter. L: lens. PD: photodetector. M: mirror. PBS: polarizing beamsplitter. QWP: quarter waveplate. HWP: half waveplate. MO: microscope objective. DUT: device under test. FG: function generator. PH: pinhole. FG: function generator.

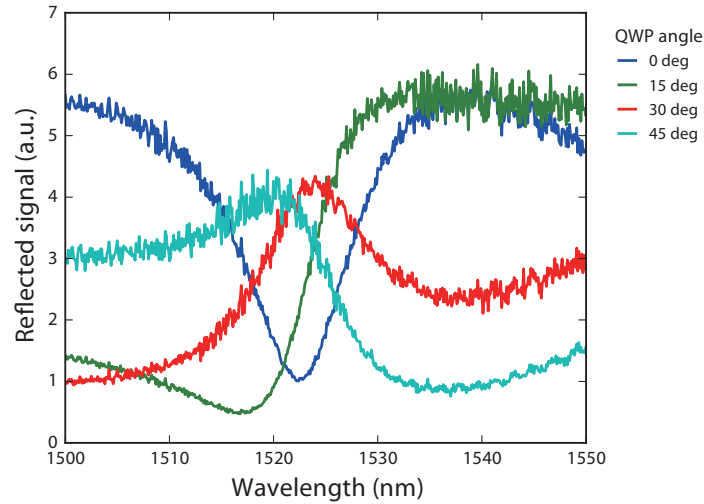


Figure 4.7: **Measured reflectivity spectra for different QWP angles in a cross-polarized setup.** These data were used to fit the model to extract the phase curve in Fig.4.4(b).

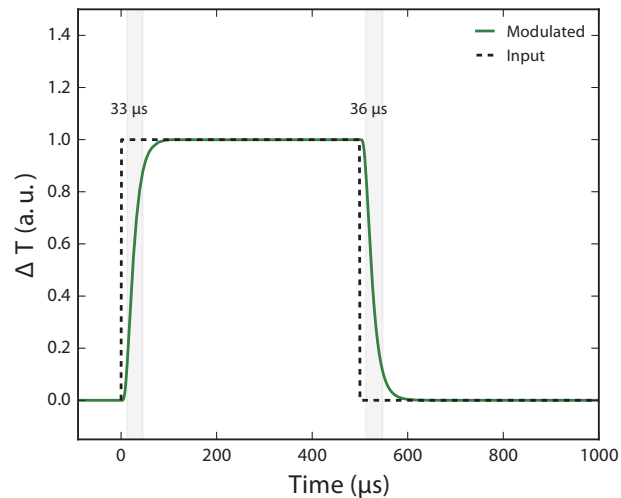


Figure 4.8: **Simulated response times in temperature modulation.** The time-dependent heat transfer simulations were performed by FEM. The rise and fall response times were found $33 \mu\text{s}$ and $36 \mu\text{s}$, respectively, in fair agreement with measured values. The difference between the simulation and the measurement should be attributed to the difference between thermal conductivities used in simulation and the actual values.

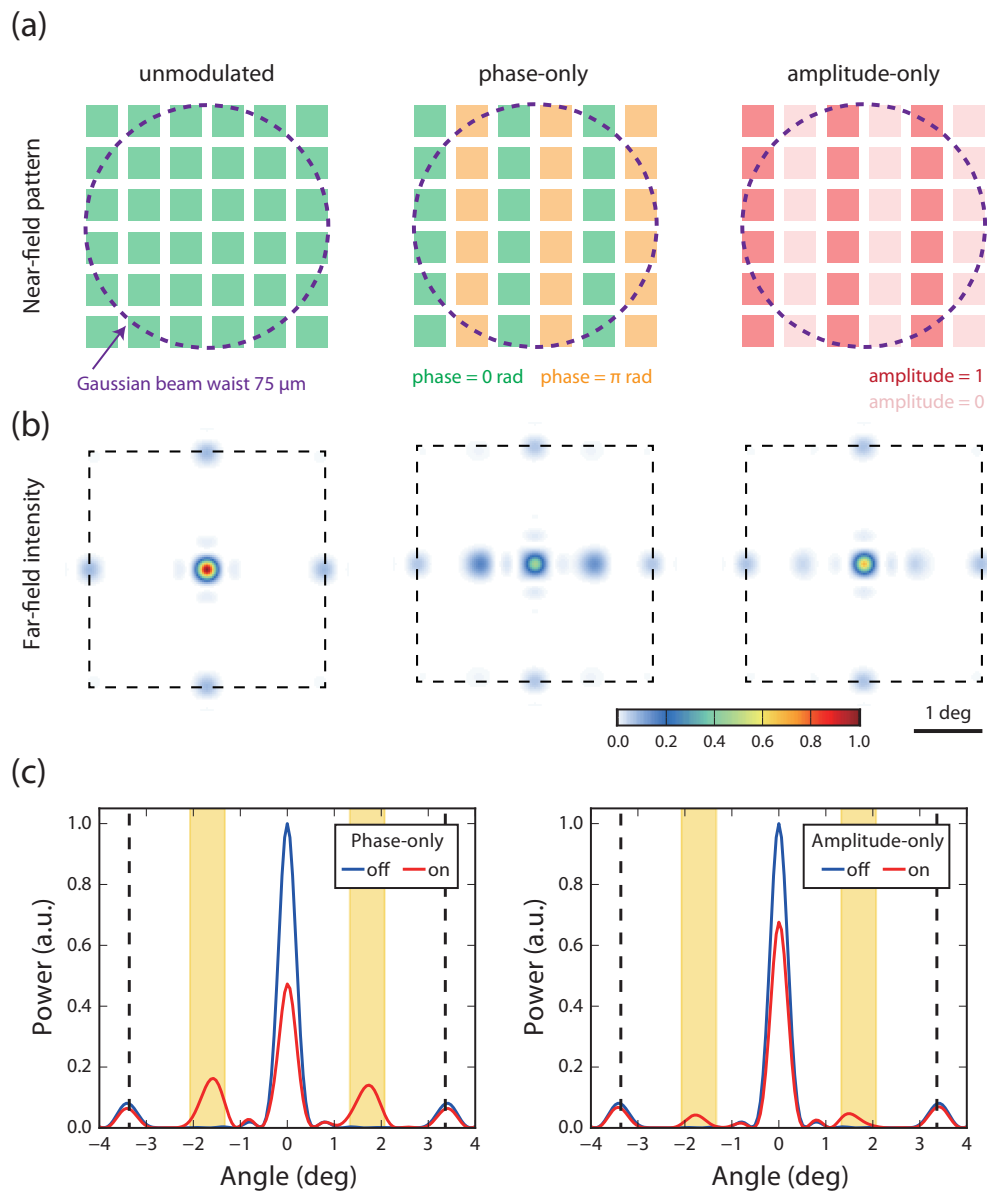


Figure 4.9: **Simulated phased array beam deflection.** (a) Simulated far-field patterns with corresponding near-field phase profile in the cases of amplitude-only and phase-only modulation. An incident Gaussian beam profile with a beam waist of $75\ \mu\text{m}$ was used. (b) Corresponding 1-D profiles of the simulated far-field patterns. We can find that phase modulation can perform a beam deflection with a higher efficiency. This also confirms that the silicon active antennas used in the experiments modulates the phase dominantly.

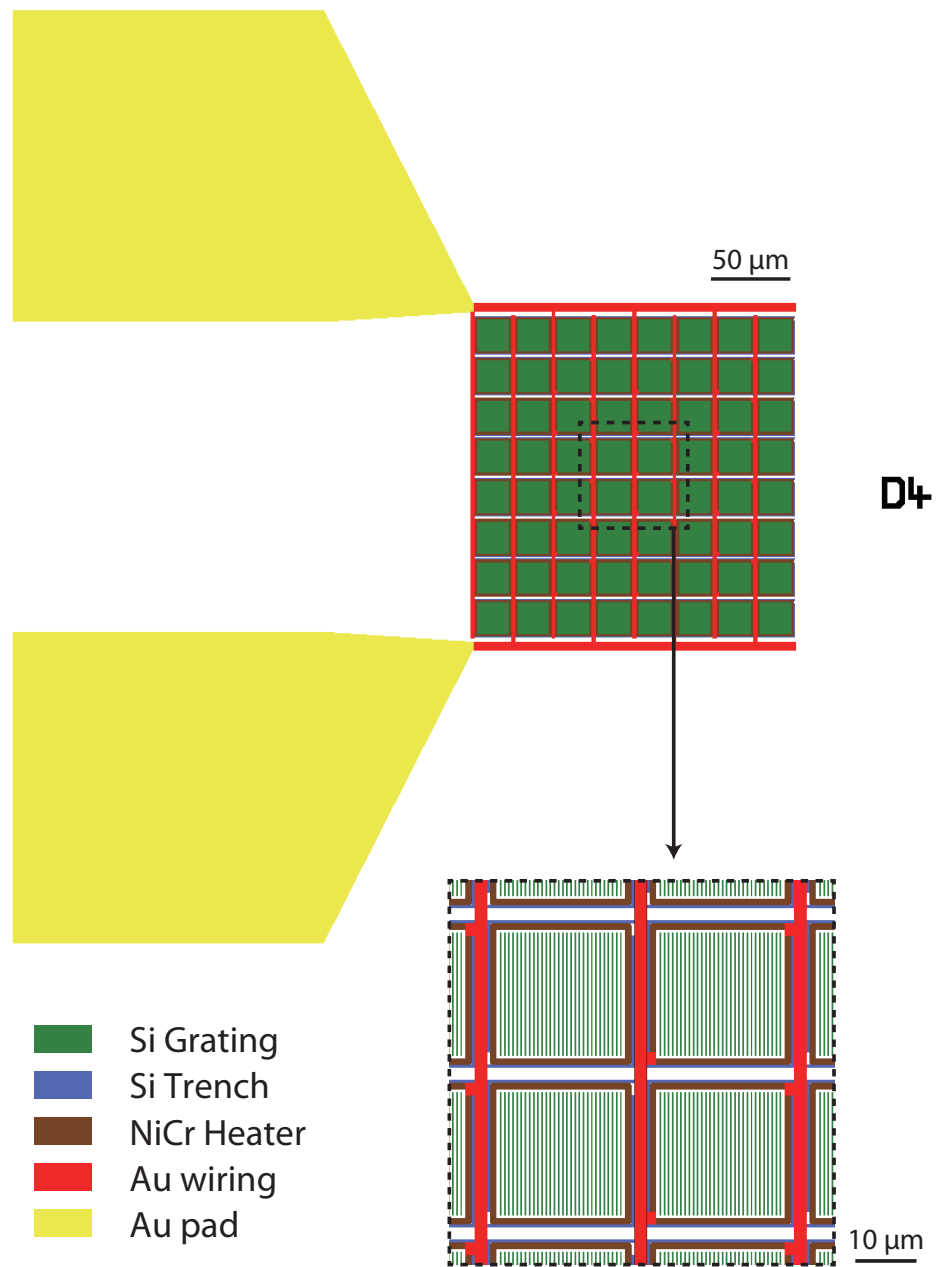


Figure 4.10: **CAD layout of the phased array used for electron beam lithography.** Only the 6×6 array in the 8×8 is an electrically active region in the beam deflection operation. The incident beam size also roughly equals the active region.

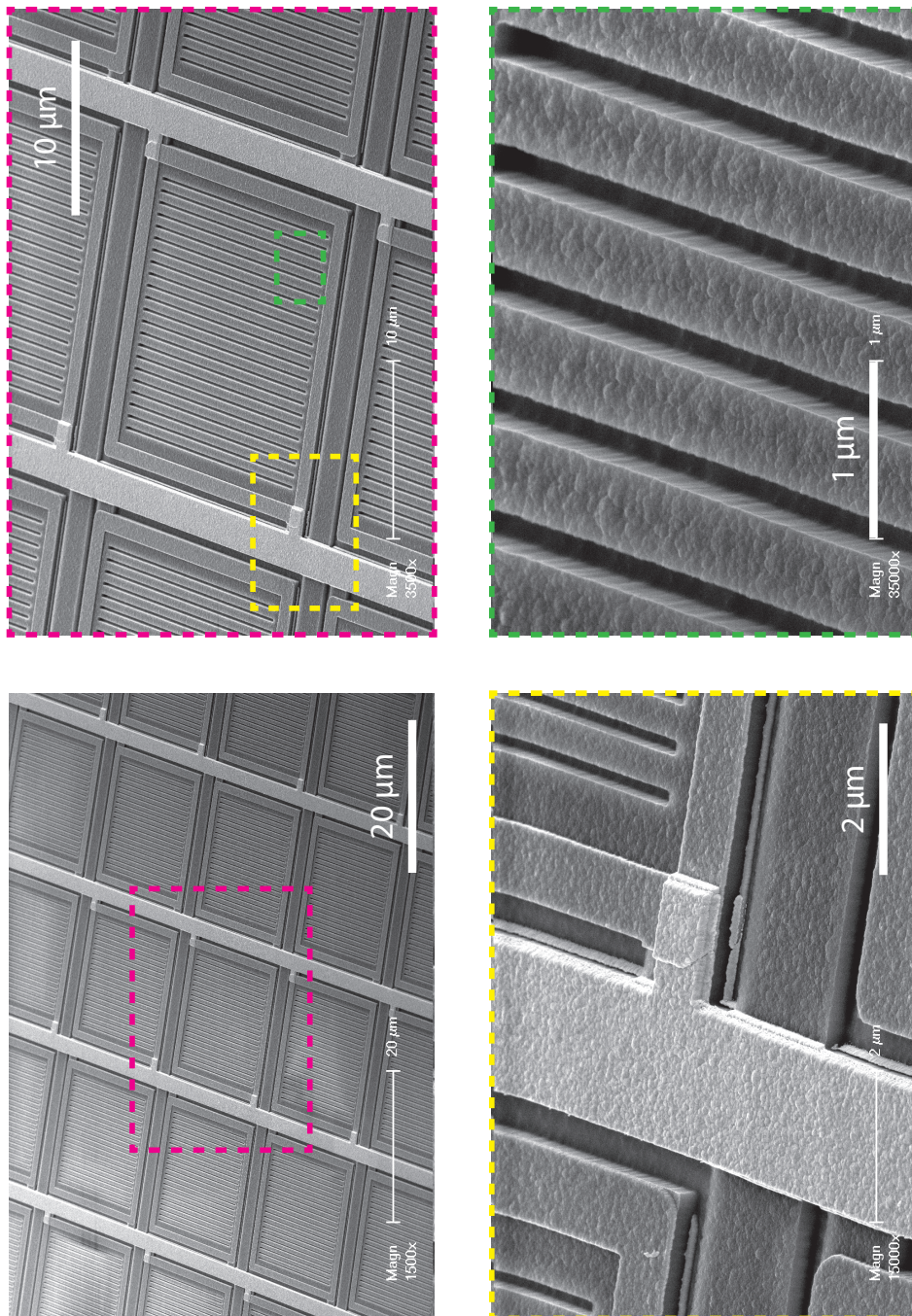


Figure 4.11: SEM images of the fabricated phased array.

DISORDER-ENGINEERED METASURFACES FOR WAVEFRONT SHAPING

The material in this chapter was presented in part in:

M. Jang*, Y. Horie*, A. Shibukawa*, J. Brake, Y. Liu, S. M. Kamali, A. Arbabi, H. Ruan, A. Faraon, and C. Yang, “Complex wavefront engineering with disorder-engineered metasurfaces”, (2017), arXiv:1706.08640, URL: <https://arxiv.org/abs/1706.08640>,

In the past decade, wavefront shaping with disordered media has demonstrated optical manipulation capabilities beyond those of conventional optics. These include extended volume, aberration-free focusing, and subwavelength focusing via evanescent mode coupling. However, translating these capabilities to useful applications has remained challenging as the input-output characteristics of the disordered media (P variables, to be defined in Section. 5.2) need to be exhaustively determined via $O(P)$ measurements. Here, we propose a paradigm shift where the disorder is specifically designed so that its exact characteristics are known, resulting in an *a priori* determined transmission matrix (TM) that can be utilized with only a few alignment steps. We implement this concept with a disorder-engineered metasurface, which exhibits additional unique features for wavefront shaping such as an unprecedented optical memory effect range, excellent stability, and a tailorable angular scattering profile. Using this designed metasurface with wavefront shaping, we demonstrate the ability to perform optical focusing with numerical apertures (NAs) as high as 0.95 within a lateral field of view (FOV) as wide as ~ 14 mm, and furthermore, perform fluorescence imaging that can resolve $\sim 2.2 \times 10^8$ points in a lateral FOV of ~ 8 mm.

5.1 Background

Wavefront shaping can be best described as a class of methods that allow control of a very large number of optical degrees of freedom, ranging up to hundreds of thousands [109]. This sets it apart from the regime of wavefront manipulation in adaptive optics where the corrections are typically performed for aberrations modeled

by a relatively small number of Zernike orders [110]. As a class of technologies, wavefront shaping is particularly well suited for applications involving disordered media. These applications can be broadly divided into two categories. In the first category, wavefront engineering works to overcome intrinsic limitations of the disordered media. Biological tissue is one such example where scattering is a problem, with wavefront shaping emerging as a solution to produce a shaped light beam that counteracts multiple scattering and enables imaging and focusing deep inside the tissue [111].

In the second category, disordered media are intentionally introduced in conjunction with wavefront engineering to unlock an optical space with spatial extent (x) and frequency content (ν) that is inaccessible using conventional optics [112–118]. One of the first demonstrations of this ability was reported by Vellekoop *et al.* [112], showing that the presence of a disordered medium (e.g. a scattering white paint layer) between a source and a desired focal plane can actually help render a sharper focus. In related efforts, researchers have also shown that wavefront shaping can make use of disordered media to couple propagating and evanescent modes, in turn enabling near-field focusing [114, 115]. Recently, there have been more extensive demonstrations combining disordered media with wavefront shaping to increase the flexibility of the optical system to, for example, significantly extend the volumetric range in which aberration-free focusing can be achieved [116–118].

Unfortunately, this class of methods is stymied by one overriding challenge – the optical input-output response of the disordered medium needs to be exhaustively characterized before use [118–122]. Fundamentally, characterizing P input-output relationships of a disordered medium requires $O(P)$ measurements. For most practical applications, P greater than 10^{12} is highly desired to enable high fidelity access to the expanded optical space enabled by the disordered media with wavefront engineering. Unfortunately, the time-consuming nature of the measurements and the intrinsic instability of the vast majority of disordered media have limited the ability to achieve high values of P . To date, the best P quantification that has been achieved is $\sim 10^8$ with a measurement time of 40 seconds [120].

In this chapter, we propose the use of a disorder-engineered metasurface (we call this a disordered metasurface for brevity) in place of a conventional disordered medium. The disordered metasurface, which is composed of a 2-D array of nano-scatterers that can be freely designed and fabricated, provides the optical “randomness” of conventional disordered media, but in a way that is fully known *a priori*. We note

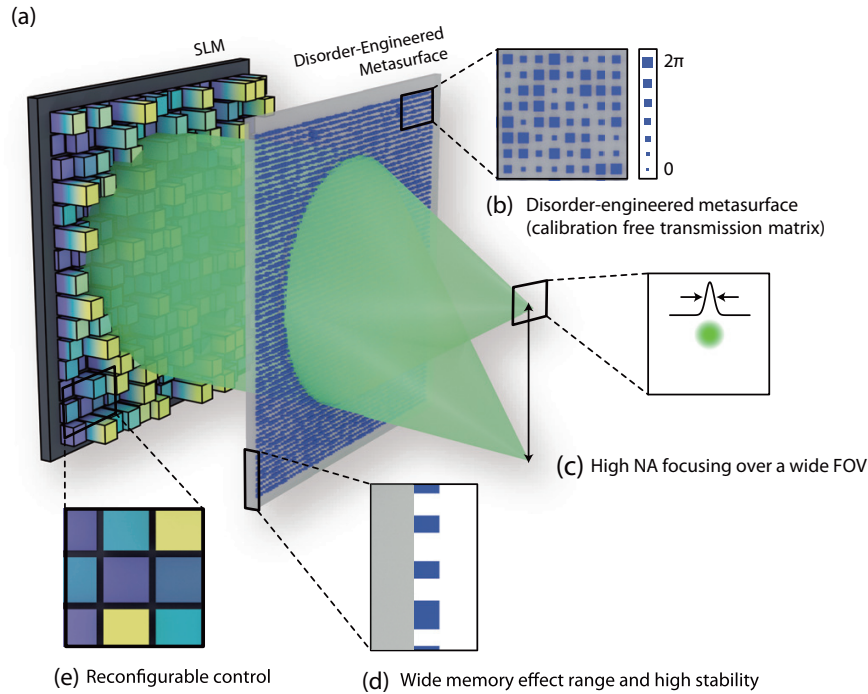


Figure 5.1: **Wavefront shaping assisted by a disorder-engineered metasurface.** (a) The system setup consists of two planar components, an SLM and a disorder-engineered metasurface. (b) The disorder-engineered metasurface is implemented by varying the size of nanoposts, which correspond to different phase delays $\phi(x, y)$ on the metasurface. (c) The wide angular scattering range enables high-NA focusing over a wide FOV. (d) The thin, planar nature of the disordered metasurface yields a large memory effect range and also makes the TM of the metasurface extraordinarily stable. (e) The SLM enables reconfigurable control of the expanded optical space available through the disordered metasurface.

that this approach is conceptually different from previous techniques with similar names [123–126] (e.g. Engineered Diffusers from RPC Photonics) since it enables the individual input-output responses rather than the statistical properties of the scattered light pattern to be engineered. Through this approach, we reduce the system characterization to a simple alignment problem. In addition to eliminating the need for extensive characterization measurements, the disordered metasurface platform exhibits a wide optical memory effect range, excellent stability, and a tailorable angular scattering profile – properties that are highly desirable for wavefront shaping but that are missing from conventional disordered media. Using this disorder-engineered metasurface platform, we demonstrate full control over $P = 1.1 \times 10^{13}$ input-output relationships after a simple alignment procedure. To demonstrate this

new paradigm for controllably exploiting optical “randomness”, we have implemented a disordered metasurface assisted focusing and imaging system that is capable of high-NA focusing ($\text{NA} \approx 0.5$) to $\sim 2.2 \times 10^8$ points in a FOV with a diameter of ~ 8 mm. In comparison, for the same FOV, a conventional optical system such as an objective lens can at most access one or two orders of magnitude fewer points.

5.2 Principles of Wavefront Shaping

Given any linear propagation medium, the wave propagation of an optical field is completely described by its Green function. For the sake of simplicity, we can consider a scalar field. Even though a disordered medium scrambles an incident beam of light, resulting in a speckle field, a seemingly “random” output field, modeling of such a system using the Green function formalism still holds, because the light scattering process involved here is linear [119]. The scalar Green function describes the causality of the input field at position \mathbf{r}' at time t' on the output field at \mathbf{r} at time t :

$$E(\mathbf{r}, t) = \iint_{S_i} d^2\mathbf{r}' \int_{-\infty}^{\infty} dt' G(\mathbf{r}, \mathbf{r}', t - t') E(\mathbf{r}', t'), \quad (5.1)$$

where S_i represents the surface containing sources of interest. Since we are interested in a monochromatic wave, we can rewrite this in the spectral domain using the time-domain Fourier transform of the fields at the oscillation of ω :

$$E(\mathbf{r}, \omega) = \iint_{S_i} d^2\mathbf{r}' G(\mathbf{r}, \mathbf{r}', \omega) E(\mathbf{r}', \omega). \quad (5.2)$$

In practice, the sources at \mathbf{r}' and receivers at \mathbf{r} correspond to the areas having a spatial extent (i.e., a pixel on the SLM and camera, respectively), and performing spatial averaging the fields within the pixel discretizes Eq. (5.2):

$$\begin{aligned} E_o &= T E_i \\ \Leftrightarrow E_o^m &= \sum_n^N t_{mn} E_i^n, \end{aligned} \quad (5.3)$$

where we omit the frequency term by considering a monochromatic wave, E_o is a column vector (with elements of E_o^m for $m = 1, \dots, M$, namely a desired focusing optical field), E_i is a column vector (with elements of E_i^n for $n = 1, \dots, N$, namely independent optical modes controlled by the SLM), and T is a matrix (i.e., the TM) where each element (t_{mn}) describes the amplitude and phase relationship between a given input mode and output focal spot. In this scenario, E_i has a dimension of

N , the number of degrees of freedom in the input field (i.e., the number of SLM pixels), E_o has a dimension of M given by the number of resolvable spots on the projection plane, and T is a matrix which connects the input and output fields with P elements, where $P \equiv M \times N$. This formalism applies to any wave propagation in a linear medium, even for a disordered medium, giving us the insights on wavefront shaping as well as its limitations.

One of the most prominent capabilities in wavefront shaping in conjunction with a disordered medium is to render a shaper focus than without the medium [112]. This counterintuitive ability can be understood using the time-reversal symmetry of the light propagation in a reciprocal system [127]. We consider a thought experiment using the time-reversed wave, where we place a point source emitter at the output plane of interest and record the fields propagated through a disordered medium at input plane. Owing to the reciprocity of the wave equation, this wave propagation can be time-reversed, in which the time-reversed signals emitted from an array of sources from the input plane should propagate through the disordered medium, and naturally converge toward the point where we placed the point source. Phase conjugation, which is the monochromatic equivalent of the time-reversal operation, is the best to deduce the optimal field to be emitted from the input and how the tight focusing is realized in wavefront shaping [128]. Using the concept of the phase conjugation, the optimal input field vector to generate a desired output focusing field is given by

$$E_i^{\text{opt}} = T^+ E_o^{\text{target}}, \quad (5.4)$$

where $+$ denotes the transpose conjugate of a matrix. Due to the imperfect realization of the phase-conjugated field[†], the actual output field does not correspond to the desired field,

$$E_o = T E_i^{\text{opt}} = T T^+ E_o^{\text{target}}. \quad (5.5)$$

In practice, it is challenging to generate a perfect phase-conjugated field as in our experiments. This is equivalent that T is not a unitary matrix, and thus $E_o \neq E_o^{\text{target}}$. Despite the imperfection of the phase conjugation, we would be able to create a sharp focusing on the output, owing to an enormous number of degrees of freedom on the input and will now show that the focusing performance depends on the input degree

[†]In our experiments as well as other demonstrations using an SLMs, we reconstruct only the low spatial frequency components of the phase-conjugated field, due to the large pixel size of SLMs. This is also known as the technique called the digital optical phase conjugation. It has also been demonstrated to perform a nearly perfect phase-conjugated field using the nonlinear optical phenomena such as Brillouin scattering and photorefractive media [128, 129].

of freedom N (presumably, $N \gg 1$), using Eq. (5.5). We consider the “intensity” of the output field on the j th receiver. If the phase-conjugated field is perfectly reconstructed, we have

$$|s_o^m|^2 = \left| \sum_l^N t_{ml} t_{jl}^* \right|^2, \quad (5.6)$$

where s_o^m is the complex amplitude in the m th pixel on the output used as the reference. For $m = j$, the output fields are coherently interfered and the ensemble average of the intensity becomes

$$\begin{aligned} \langle |s_o^{m=j}|^2 \rangle &= \left\langle \left(\sum_l^N |t_{jl}|^2 \right)^2 \right\rangle \\ &= \left\langle \left(\sum_l^N |t_{jl}|^4 \right) \right\rangle + \left\langle \sum_{l \neq l'}^{N,N} |t_{jl}|^2 |t_{jl'}|^2 \right\rangle \\ &= N(N-1) \langle |t|^2 \rangle^2 + N \langle |t|^4 \rangle \\ &\approx N^2 \langle |t|^2 \rangle^2. \end{aligned} \quad (5.7)$$

For $m \neq j$, the output fields are incoherently interfered and the ensemble average of the intensity becomes

$$\begin{aligned} \langle |s_o^{m \neq j}|^2 \rangle &= \left\langle \sum_{l, l'}^{N,N} t_{ml} t_{ml'}^* t_{jl}^* t_{jl'} \right\rangle \\ &= \left\langle \left(\sum_l^N |t_{ml}|^2 |t_{jl}|^2 \right) \right\rangle + \left\langle \sum_{l \neq l'}^{N,N} t_{ml} t_{ml'}^* t_{jl}^* t_{jl'} \right\rangle \\ &= N \langle |t|^2 \rangle^2. \end{aligned} \quad (5.8)$$

With the results of Eqs. (5.7) and (5.8), we can estimate the contrast η , the ratio between the intensity transmitted into the focal spot and the surrounding background, namely the energy signal-to-noise ratio (SNR), which is solely dependent on the number of input degrees of freedom N^\dagger as given by

$$\eta \equiv \frac{\langle |s_o^{m=j}|^2 \rangle}{\langle |s_o^{m \neq j}|^2 \rangle} \approx \frac{N^2 \langle |t|^2 \rangle^2}{N \langle |t|^2 \rangle^2} = N. \quad (5.9)$$

We note that these results can be generalized to arbitrary wavefronts (e.g. beam steering or optical vortex generation) simply by switching E_o to an appropriate basis set.

[†]In the case of phase-only and amplitude-only reconstruction of the phase conjugation, the contrast is given by $\eta = (\pi/4)N$ and $\eta = (1/2\pi)N$, respectively [130].

One of the unique and most useful aspects of wavefront shaping with disordered media is that it allows access to a broader optical space in both spatial extent (x) and frequency content (ν) than the input optical field can conventionally access. For example, when an SLM is used alone, the generated optical field E_i contains a limited range of spatial frequencies due to the large pixel pitch of the SLM (ν_x or $\nu_y \leq 1/(2d_{\text{SLM}})$, where d_{SLM} is the pixel pitch; typically $\sim 10\ \mu\text{m}$). As a consequence, the number of resolvable spots M is identical to the number of controllable degrees of freedom N . In contrast, when a disordered medium is placed in the optical path, its strongly scattering nature generates an output field E_o with much higher spatial frequencies given by $\sqrt{\nu_x^2 + \nu_y^2} \leq 1/\lambda$, where λ is the wavelength of the light. According to the space–bandwidth product formalism [131], this means that the number of addressable focal spots M within a given modulation area S , is maximally improved to

$$M = S \times \frac{\pi}{\lambda^2}. \quad (5.10)$$

The scheme for focusing with disordered medium assisted wavefront shaping can be understood as the process of combining N independent optical modes to constructively interfere at a desired position on the projection plane [112, 132, 133]. In general, due to the increased spatial frequency range of the output field, the number of addressable spots M is much larger than the number of degrees of freedom in the input, N , and therefore the accessible focal points on the output plane are not independent optical modes. This will be discussed in detail in Sec. 5.A in Appendix by performing singular value decomposition (SVD) of the TM. Instead, each focal spot exists on top of a background which contains the contributions from the unoptimized optical modes in the output field. Here the contrast η , the ratio between the intensity transmitted into the focal spot and the surrounding background, is dictated by the number of controlled optical modes in the input, N [132]. In practical situations where, for instance, the addressed spots are used for imaging or photo-switching, the contrast η needs to be sufficiently high to ensure the energy leakage does not harmfully compromise the system performance.

To maximize performance, we can see it is desirable to have as many resolvable spots as possible, each with high contrast. This means that both M and N , and in turn P , should be as high as possible. Practically, there are two ways to measure the elements – orthogonal input probing and output phase conjugation. Refer to Sec. 5.B in Appendix for the conventional method to measure the TM. In each case, an individual measurement corresponds to a single element in the TM and is

accomplished by determining the field relationship between an input mode and a location on the projection plane. Both still necessitate $O(P)$ measurements which, when P is large, leads to a prohibitively long measurement time. As a point of reference, if the fast TM characterization method reported in Ref. [120] could be extended without complications, it would still require a measurement time of over 40 days to characterize a TM with $P = 10^{13}$ elements. In comparison, the stability associated with most conventional disordered media can last only several hours [132, 134, 135].

In contrast, our disorder-engineered metasurface avoids the measurement problem altogether since all elements of the TM are known *a priori*. This means that now the procedure to calibrate the system is simplified from the $O(P)$ measurements needed to determine the TM to the small number of alignment steps for the disorder-engineered metasurface and the SLM.

A schematic illustration of the technique is presented in Fig. 5.1 with the omission of a $4-f$ imaging system optically conjugating the SLM plane to the disordered metasurface. An SLM structures a collimated incident beam into an optimal wavefront which in turn generates a desired complex output wavefront through the disordered metasurface. Since the TM is known *a priori*, the process to focus to a desired location is a simple computation. The optimal incident pattern E_i^{opt} that encodes the information for a target field E_o^{target} is calculated using the concept of phase conjugation. This approach enables us to access the maximum possible number of resolvable spots for wavefront shaping for a given modulation area S with the added benefit of control over the scattering properties of the metasurface.

5.3 Disorder-Engineered Metasurfaces

Design of Disordered Metasurfaces

The disordered metasurface platform demonstrated in this study shares the same design principles as the conventional metasurfaces that have been previously reported to implement planar optical components [2, 14, 15, 136–138]: rationally designed subwavelength scatterers or meta-atoms are arranged on a 2-D lattice to purposefully shape optical wavefronts with subwavelength resolution as illustrated in Fig. 5.2(a). The disordered metasurface, consisting of silicon nitride (SiN_x) nanoposts sitting on a fused silica substrate, imparts local and space-variant phase delays with high transmission for the designed wavelength of 532 nm. The disordered metasurface consists of SiN_x nanoposts arranged on a subwavelength square lattice with a

periodicity of 350 nm as shown in Fig. 5.2(b). The width of each SiN_x nanopost is precisely controlled within a range from 60 nm to 275 nm, correspondingly imparting local and space-variant phase delays covering a full range of 2π with close to unity transmittance for an incident wavefront at the design wavelength of 532 nm. The widths of the nanoposts corresponding to the grayed regions in Fig. 5.2(b) correspond to high quality factor (Q -factor) resonances and are excluded in the design of the disordered metasurface. The phase profile $\phi(x, y)$ of the disordered metasurface is designed to yield an isotropic scattering profile over the maximal possible spatial bandwidth of $1/\lambda$ or the desired angular range using the Gerchberg–Saxton algorithm. The initial phase profile of the far-field is randomly chosen from a uniform distribution between 0 and 2π radians. After several iterations, the phase profile converges such that the far-field pattern has isotropic scattering over the target angular ranges. This approach helps to minimize undiffracted light and evenly distribute the input energy over the whole angular range.

Fabrication of Disordered Metasurfaces

A SiN_x thin film of 630 nm is deposited using plasma-enhanced chemical vapor deposition (PECVD) on a fused silica substrate. The metasurface pattern is first defined in ZEP520A positive resist using an electron beam lithography system. After developing the resist, the pattern is transferred onto a 60 nm-thick Al₂O₃ layer deposited by electron beam evaporation using the lift-off technique. The patterned Al₂O₃ serves as a hard mask for the dry etching of the 630 nm-thick SiN_x layer in a mixture of SF₆ and C₄F₈ plasma and is finally removed by a mixture of NH₄OH and H₂O₂ at 80°C. Diagrammatic representation of the RGB visible color filter fabrication is illustrated in Fig. 5.3.

Characterization of Disordered Metasurfaces

The experimentally measured scattering profile confirms the nearly isotropic scattering property of the disordered metasurface, presenting a scattering profile that fully extends to the spatial frequency of $1/\lambda$ as shown in Fig. 5.2(c). This platform also allows tailoring of the scattering profile, which can be potentially useful in conjunction with angle-selective optical behaviors such as total internal reflection. Figure 5.2(d) presents the measured scattering profiles of disordered metasurfaces designed to have different angular scattering ranges, corresponding to NAs of 0.3, 0.6, and 0.9 (see Fig. 5.8 in Appendix for 2-D angular scattering profiles). In addition to a highly isotropic scattering profile, the disordered metasurface also exhibits a very large

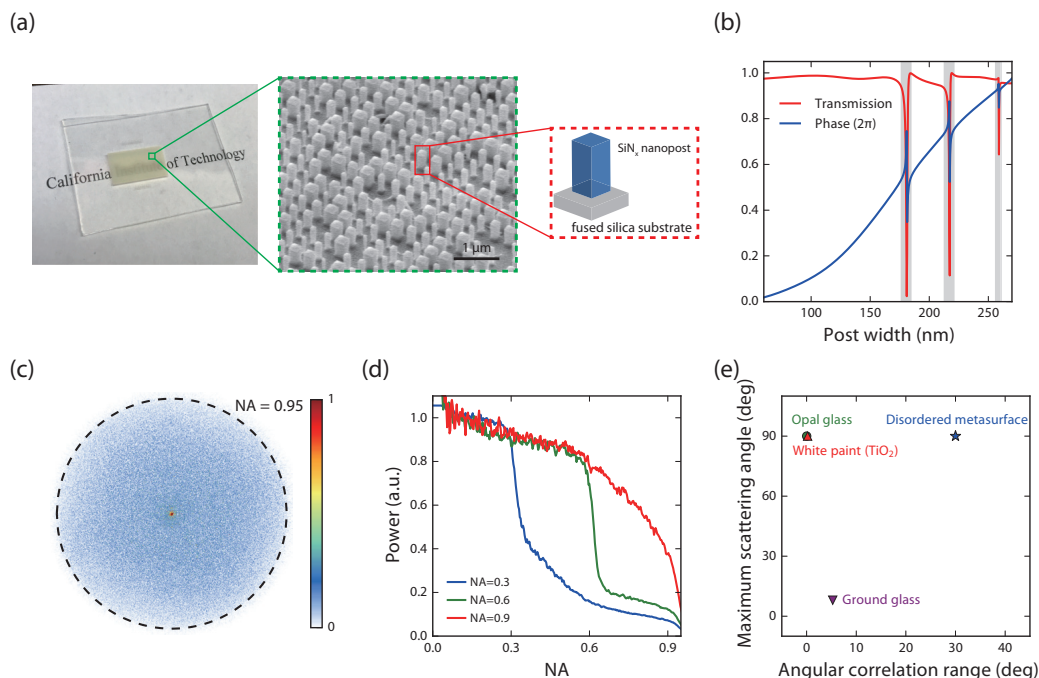


Figure 5.2: **Disorder-engineered metasurface.** (a) Photograph and SEM image of a fabricated disorder-engineered metasurface. (b) Simulated transmission and phase of the SiN_x nanoposts as a function of their width at a wavelength of 532 nm. These data are used as a look-up table for the metasurface design. (c) Measured 2-D angular scattering profile of the disordered metasurface, normalized to the strongest scattered field component. (d) Measured 1-D angular scattering profile of the disordered metasurfaces that were specifically designed to scatter the incident light to certain angular ranges (NA = 0.3, 0.6, 0.9). (e) Memory effect range and angular scattering range of the disordered metasurface compared with conventional random media such as white paint, opal glass, and ground glass diffusers.

angular (tilt/tilt) correlation range (also known as the optical memory effect [139]). The correlation is larger than 0.5 even up to a tilting angle of 30 degrees (Fig. 5.2(e)). In comparison, conventional scattering media commonly used for scattering lenses, such as opal glass and several micron-thick titanium dioxide (TiO₂) white paint layers, exhibit much narrower correlation ranges of less than 1 degree (Fig. 5.2(e) [140]). Although ground glass diffusers present a relatively wider correlation range of ~5 degrees, their limited angular scattering range makes them less attractive for wavefront shaping. Moreover, the disordered metasurface is extraordinarily stable. We were able to retain the ability to generate a high quality optical focus from the same metasurface without observable efficiency loss over a period of 75 days by making only minor corrections to the system alignment to compensate for mechanical

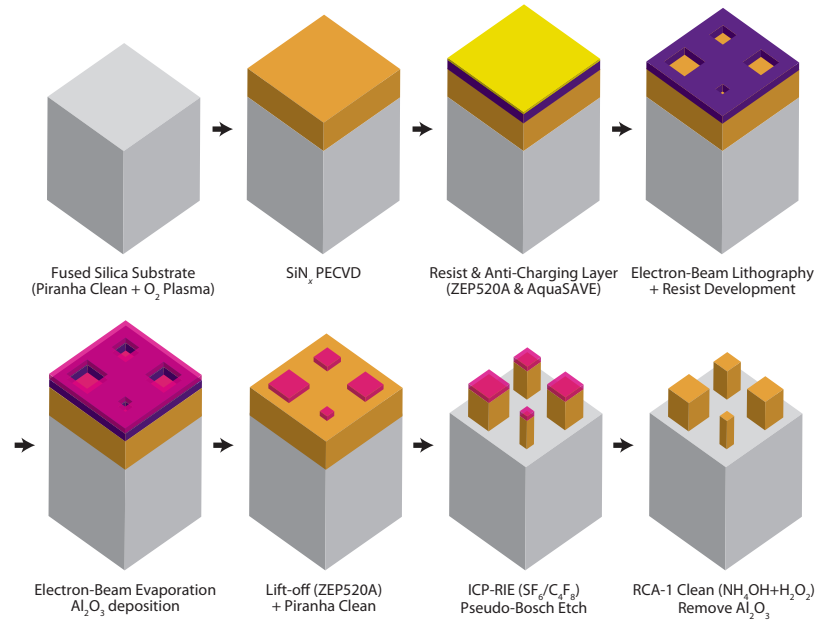


Figure 5.3: **Disordered metasurface fabrication.** Diagrammatic representation of the disordered metasurface fabrication.

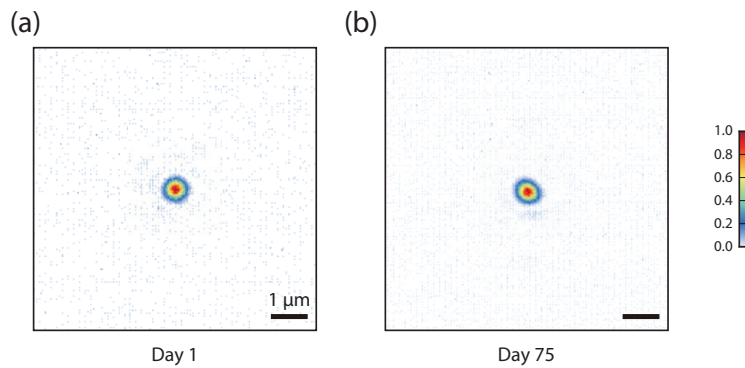


Figure 5.4: **Extraordinary stability of a disordered metasurface.** Over a period of 75 days, a high quality optical focus was obtained from the same metasurface without observable efficiency loss by small system alignments to compensate for mechanical drift. (a) Reconstructed focus on the 1st day. The measured contrast was 19,800. (b) Reconstructed focus on the 75th day. The measured contrast was 21,500. Scale bar: 1 μm.

drift as shown in Fig. 5.4.

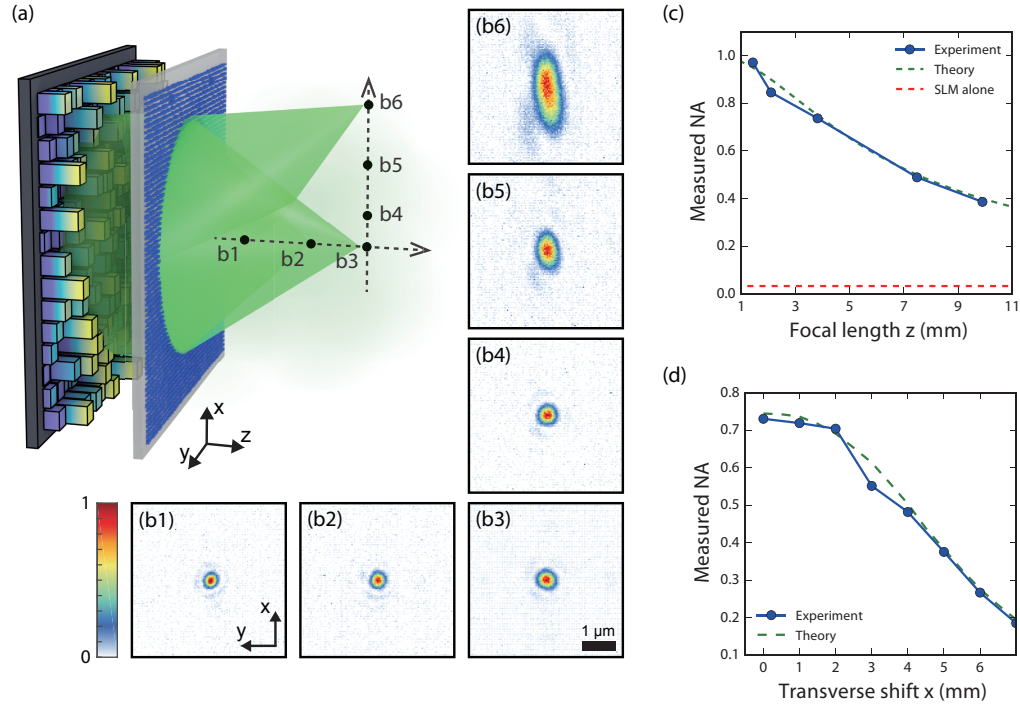


Figure 5.5: **Experimental demonstration of diffraction-limited focusing over an extended volume.** (a) Schematic of optical focusing assisted by the disordered metasurface. (b1-6) Measured 2-D intensity profiles for the foci reconstructed at the positions indicated in (a). (b1-3) are the foci along the optical axis at $z = 1.4, 2.1,$ and 3.8 mm, respectively, corresponding to NAs of $0.95, 0.9,$ and 0.75 . (b1-3) are the foci at $x = 0, 1, 4,$ and 7 mm scanned on the fixed focal plane of $z = 3.8$ mm. Scale bar: $1 \mu\text{m}$. (c) Measured NA (along the x -axis) of the foci created along the optical axis (red solid line) compared with theoretical values (black dashed line). When the SLM is used alone, the maximum accessible NA is 0.033 (orange dashed line). (d) Measured NA (along the x -axis) of the foci created along x -axis at $z = 3.8$ mm (red solid line) compared with theoretical values (black dashed line). The number of addressable focusing points within the 14 -mm diameter FOV was estimated to be 4.3×10^8 .

5.4 High-NA Optical Focusing over an Extended Volume

Alignment Procedure

We experimentally tested our wavefront shaping scheme in the context of disordered medium assisted focusing and imaging. First, we aligned the disordered metasurface to the SLM. The alignment procedure consists of two steps to ensure the proper mapping of the SLM pixels onto the intended coordinates of the disordered metasurface. Cross-shaped markers engraved at the four corners of the metasurface are used

to guide rough alignment. Then, the marginal misalignments (e.g. translation and tip-tilt) and aberrations induced by the $4-f$ system are corrected. For this purpose, a collimated laser beam (Spectra-Physics, Excelsior 532) is tuned to be incident on the metasurface and the resulting field is measured with phase shifting holography. The residual misalignments and aberrations are then calibrated by comparing the measured complex field with the calculated one and digitally compensating for the misalignment by adding appropriate correction patterns on the SLM.

Procedure for Optical Focusing Using Transmission Matrix

Next, to demonstrate the flexibility of this approach, we reconstructed a converging spherical wave for a wide range of lateral and axial focus positions. Figure 5.5(a) presents the simplified schematic for optical focusing (see Fig. 5.9 for the complete optical setup). The transmission matrix model in our experiments describes the amplitude and phase relationship between each controllable input mode, given as each SLM pixel, and each desired focusing optical field. The calculation of T was carried out in a row-by-row manner, based on the intrinsic phase profile of the disordered metasurface $\phi(x, y)$. Setting the position of the focal spot corresponding to m -th row vector in T as $\mathbf{r}'_m = (x'_m, y'_m, z')$ for $m = 1, \dots, M$, the converging spherical wavefront on the plane of metasurface is given as

$$S_m(x, y) = \exp \left[-i \frac{2\pi}{\lambda} \sqrt{(x - x'_m)^2 + (y - y'_m)^2 + z'^2} \right], \quad (5.11)$$

where z' is the focal length. Then, the corresponding input field on the plane of metasurface is simply given as the product of the spherical wavefront $S_m(x, y)$ and the transmission phase profile of the disordered metasurface:

$$E_m^{\text{meta}}(x, y) = S_m(x, y) \times \exp(i\phi(x, y)). \quad (5.12)$$

Next, to calculate the input field on the plane of SLM that corresponds to the input field on the plane of metasurface $E_m^{\text{meta}}(x, y)$, a low-pass spatial frequency filter \mathcal{L} is applied to $E_m^{\text{meta}}(x, y)$ using a fast Fourier transform algorithm:

$$E_m^{\text{SLM}}(x, y) = \mathcal{L} [E_m^{\text{meta}}(x, y)] \quad (5.13)$$

Finally, the $E_m^{\text{SLM}}(x, y)$ is sampled at positions corresponding to N SLM pixels for discretization, yielding N matrix elements. That is, the discretized complex field composes the m -th row of transmission matrix T (or the m -th column of T^+ for the conjugate) that relates all controllable input modes to a given focal spot on

the projection plane. In the actual experiment, we use an SLM (Pluto, Holoeye) for phase-only reconstruction of the optimal field E_i^{opt} within a circular aperture with a 4.3 mm radius. In order to measure the focal spot, we use a custom-built microscope setup consisting of 100× objective lens (Olympus, UMPlanFl) with an NA of 0.95, a tube lens (Nikon, 2×, Plan Apo), and a CCD camera (Imaging Source, DFK 23UP031).

Demonstration of High-NA Focusing in an Extended Volume

Figure 5.5(b1-3) shows the 2-D intensity profiles for the foci reconstructed along the optical axis at $z' = 1.4, 2.1,$ and 3.8 mm, measured at their focal planes. The corresponding NAs are 0.95, 0.9, and 0.75, respectively. The full width at half maximum (FWHM) spot sizes of the reconstructed foci were 280, 330, 370 nm, which are nearly diffraction-limited as shown in Fig. 5.5(c). The intensity profiles are highly symmetric, implying that the converging spherical wavefronts were reconstructed with high fidelity through the disordered metasurface. It is also remarkable that this technique can reliably control the high transverse wavevector components corresponding to an NA of 0.95, while the SLM used alone can control only those transverse wavevectors associated with an NA of 0.033.

Figure 5.5(b4-6) shows the 2-D intensity profiles at $x' = 0, 1, 4,$ and 7 mm on the fixed focal plane of $z' = 3.8$ mm (corresponding to the on-axis NA of 0.75). Because the disordered metasurface based scattering lens is a singlet lens scheme, the spot size along the x -axis increased from 370 to 1500 nm as the focus was shifted (summarized in Fig. 5.5(d)).

The total number of resolvable spots achievable with the disordered metasurface, M , was experimentally determined to be $\sim 4.3 \times 10^8$ based on the plot in Fig. 5.5(d), exceeding the number of controlled degrees of freedom on the SLM ($N \sim 10^5$) by over 3 orders of magnitude. The NA of ~ 0.5 was also maintained in a lateral FOV with a diameter of ~ 8 mm, resulting in 2.2×10^8 resolvable focal spots. For the sake of comparison, a high-quality objective lens with an NA of 0.5 typically has $\sim 10^7$ resolvable spots, an order of magnitude smaller than the number of the spots demonstrated with the disordered metasurface.

With our disordered metasurface platform we control a TM with a number of elements P given by the product of the number of resolvable focal spots on the output plane and the number of controllable modes in the input. The P we achieved with our system was 1.1×10^{13} which allowed us to address $\sim 4.3 \times 10^8$ focus spots with a contrast

factor η of $\sim 2.5 \times 10^4$. This value of P is 5 orders of magnitude higher than what has previously been reported [120]. These findings testify to the paradigm-shifting advantage that this engineered “randomness” approach brings.

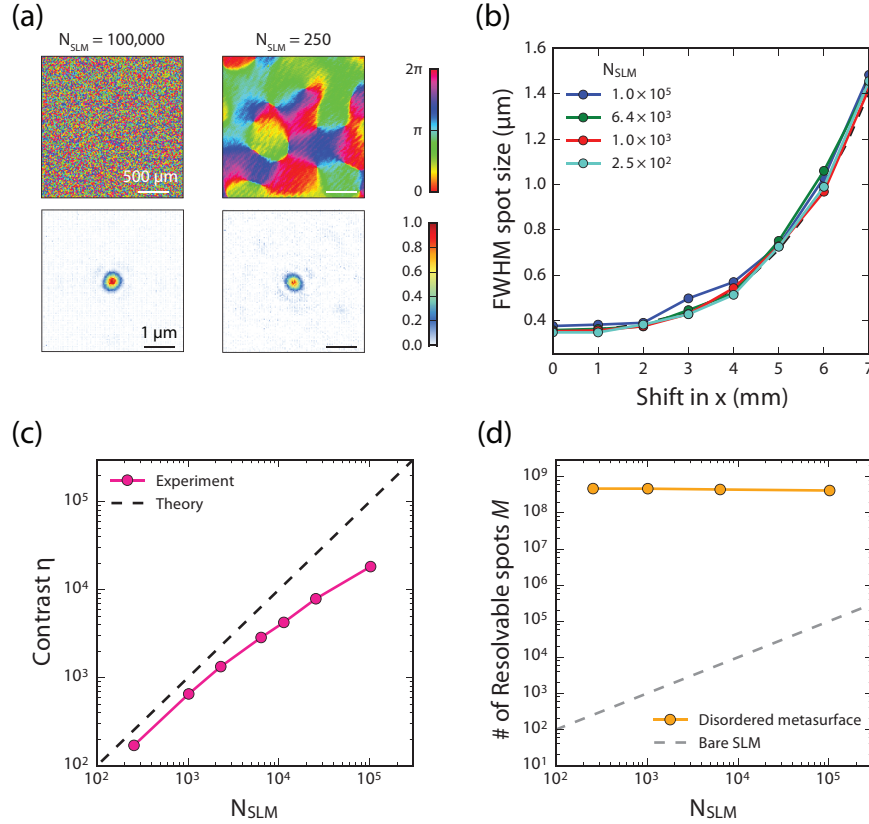


Figure 5.6: **Demonstration of ultra-high number of resolvable spots even with a handful of physically controlled degrees of freedom as inputs.** (a) Cropped phase images displayed on the SLM (top panels) as well as the corresponding 2-D intensity profiles (bottom panels) of the foci reconstructed at $z' = 3.8$ mm on axis (NA = 0.75). The controlled number of input optical modes displayed SLM was 1.0×10^5 (left) and 2.5×10^2 (right), respectively. Scale bars for the phase images and the 2-D intensity profiles are $500 \mu\text{m}$ and $1 \mu\text{m}$, respectively. (b) Measured FWHM spotsizes of the foci created along the x -axis. The measured spotsize shows a good agreement with the theoretical one, regardless of the number of input modes controlled on the SLM. (c) Dependence of contrast factor η on the number of optical modes controlled on the SLM N_{SLM} . (d) Measured number of resolvable spots M as a function of the number of optical modes controlled on the SLM N_{SLM} .

We also experimentally confirmed that even with reduced control over the number of input modes, we can still access the same number of resolvable spots on the output plane, albeit with a reduced contrast. By binning pixels on the SLM, we reduced the number of controlled degrees of freedom on the SLM by up to three orders of

magnitude, from $\sim 10^5$ to $\sim 10^2$, and verified that the capability of diffraction-limited focusing over a wide FOV is maintained as shown in Fig. 5.6. Although the same number of focal spots can be addressed, the contrast factor η is sacrificed when the number of degrees of control is reduced. Using $\sim 10^2$ degrees of freedom in the input, we achieved a contrast factor of ~ 70 . This validates that the wavefront shaping scheme assisted by the disordered metasurface can greatly improve the number of addressable focal spots for wavefront shaping regardless of the number of degrees of freedom in the input.

5.5 Wide FOV, High-Resolution Fluorescence Imaging

Procedure for Scanning Fluorescence Imaging

Finally, we implemented a scanning fluorescence microscope for high-resolution wide FOV fluorescence imaging. The setup of our scanning microscope is shown in Fig. 5.9(c) in Appendix. For the collection of the scanned fluorescent signal, an imaging system consisting of a 4 \times objective lens (Olympus, 0.1NA, Plan N) and tube lens (Thorlabs, AC508-100-A-ML) is used to cover most of the FOV of the scanning microscope. We scan the focal spot created behind the metasurface across the region of interest with a 10 ms pixel dwell time. A pair of galvanometric mirrors are used to scan $2 \times 2 \mu\text{m}^2$ patches with a step size of 200 nm, and the neighboring patches are successively scanned by adding a compensation map on the SLM to correct coma aberrations, instead of exhaustively calculating and refreshing the E_i^{opt} for every spot. The fluorescent signal is detected by the sCMOS camera (PCO, PCO.edge 5.5) with an exposure time of 7 ms. The fluorescence signal is extracted from the camera pixels corresponding to the scanned focus position. The imaging time for a $30 \times 30 \mu\text{m}^2$ area is 5 min, which can be easily improved by two orders of magnitude using a high-power laser and resonant scanning mirrors.

Fluorescence Imaging of *Giardia Lamblia* Cysts

Figure 5.7(a) presents the wide FOV low-resolution fluorescence image of immunofluorescence-labeled parasites (*Giardia lamblia* cysts; see Sec. 5.C in Appendix for sample preparation procedures) captured through the 4 \times objective lens. As shown in the magnified view in Fig. 5.7(b3), a typical fluorescent image directly captured with a 4 \times objective lens was significantly blurred, so that the shape and number of parasites was not discernible from the image. Figure 5.7, (b1, c, and d) presents the fluorescence images obtained with our scanning microscope. The scanned images

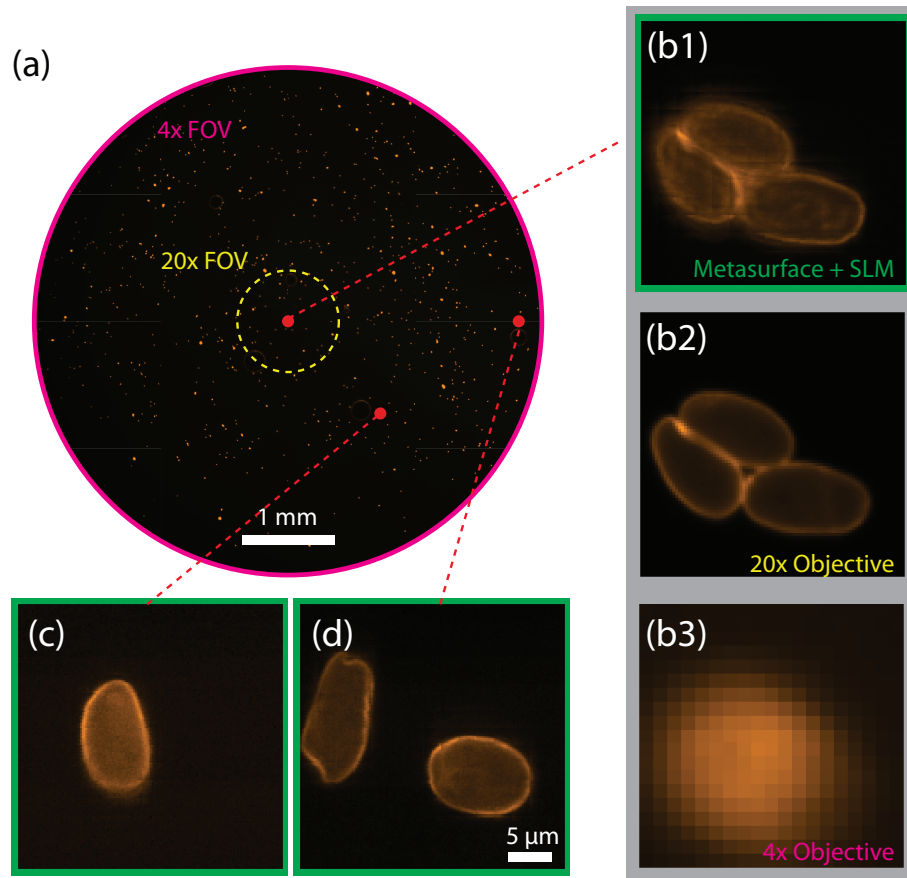


Figure 5.7: **Demonstration of disordered metasurface assisted microscope for high resolution wide-FOV fluorescence imaging of *giardia lamblia* cysts.** (a) Low resolution bright field image captured by a conventional fluorescence microscope with a 4× objective lens (NA = 0.1). Scale bar: 1 mm. (b1-3) Fluorescence images captured at the center of the FOV. (b1) Images obtained with a disordered metasurface lens. (b2) Ground truth fluorescence image captured with a 20× objective lens (NA = 0.5). (b3) Magnified low-resolution fluorescence image captured with the 4× objective. (c,d) Images obtained with the disorder metasurface-assisted microscope at $(x, y) = (1, 1)$ and $(2.5, 0)$ mm, respectively. This demonstrates that we can indeed use the system for high resolution and wide FOV imaging.

resolve the fine features of parasites both near the center and the boundary of the 5-mm wide FOV (Fig. 5.7(d)). Our platform provides the capability for high-NA focusing ($\text{NA} \approx 0.5$) within a FOV with a diameter of ~ 8 mm, as shown in Fig. 5.5. To validate the performance of our imaging system, we compare it to conventional $20\times$ and $4\times$ objectives. The captured images in Fig. 5.7 demonstrate that we can achieve the resolution of the $20\times$ objective over the FOV of the $4\times$ objective.

5.6 Summary and Outlook

Here we have implemented a disorder-engineered medium using a metasurface platform and demonstrated the benefit of using it for wavefront shaping. Our study is the first to propose engineering the entire input-output response of an optical disordered medium, presenting a new approach to disordered media in optics. Allowing complete control of the TM *a priori*, the disorder-engineered metasurface fundamentally changes the way we can employ disordered media for wavefront shaping. Prior to this study, to control P input-output relationships through a disordered medium, $O(P)$ calibration measurements were required. In contrast, the disorder-engineered metasurface allows for a TM with P elements to be fully employed with only a simple alignment procedure.

Although we only demonstrate the reconstruction of spherical wavefronts in this study, our method is generally applicable to produce arbitrary wavefronts for applications such as beam steering, vector beam generation, multiple foci, or even random pattern generation. We anticipate that the large gain in the number of addressable optical focal spots (or equivalently angles or patterns) enabled by our method will substantially improve existing optical techniques such as fluorescence imaging, optical stimulation/lithography [141, 142], free space coupling among photonic chips/optical networks [143, 144], and optical encryption/decryption [145].

In the specific application of focal spot scanning, our basic system consisting of two planar components, a metasurface phase mask and a conventional SLM, offers several advantages. The system is highly scalable and versatile, bypassing the limitations and complexities of using conventional objective lenses. The scalability of the metasurface can be especially useful in achieving ultra-long working distances for high-NA focusing. The scheme can also be implemented as a vertically integrated optical device together with electronics [146] (e.g. a metasurface phase mask on top of a transmissive LCD), providing a compact and robust solution to render a large number of diffraction-limited spots. Furthermore, the concept is applicable

over a wide range of the electromagnetic spectrum with the proper choice of low-loss materials for the meta-atoms (e.g. SiN_x or TiO_2 for entire visible [137, 147] and Si for near infrared wavelengths [11, 13, 15, 148]), which allows for multiplexing different colors, useful for multicolor fluorescence microscopy and multiphoton excitation microscopy. Finally, the planar design provides a platform to achieve ultra-high NA solid-immersion lenses [149] or total internal reflection fluorescence (TIRF) excitation [150], suitable for super-resolution imaging and single-molecule biophysics experiments.

More broadly speaking, we anticipate the ability to customize the design of the disordered metasurface for a particular application will prove highly useful. For example, we can tailor the scattering profile of the disordered metasurface to act as an efficient spatial frequency mixer or to be exploited for novel optical detection strategies [125, 151, 152]. The disordered metasurface can serve as a collection lens, analogous to the results obtained for light manipulation, providing an enhanced resolving power and extended view field. Additionally, the metasurface platform can be designed independently for orthogonal polarization states, which provides additional avenues for control in wavefront shaping [16]. Together, the engineering flexibility provided by these parameters offers unprecedented control over complex patterned illumination, which can directly benefit emerging imaging methods that rely on complex structured illumination [153, 154].

To conclude, we explored the use of a disorder-engineered metasurface in wavefront shaping, challenging a prevailing view of the “randomness” of disordered media by programmatically designing its “randomness”. The presented technology has the potential to provide a game-changing shift that unlocks the benefits of wavefront shaping, opening new avenues for the design of optical systems and enabling new techniques for exploring complex biological systems.

Appendix

5.A Degrees of Freedom in a Disordered Metasurface Assisted Wavefront Engineering System

In this supplementary section, we describe the disorder-engineered metasurface and phase-only SLM optical system from the main text in a general mathematical framework. This framework is based on the SVD of the linear operator (e.g. the TM), which allows us to rigorously characterize the degrees of freedom of the optical system [133, 155]. We show that the linear operator connecting the input and output optical modes always has a full rank of N (the number of pixels in the SLM), and thus the degrees of freedom for the output modes is also equal to N . However, even though we are limited to N degrees of freedom for the output modes, it is still possible to have a large number of resolvable focal spots within a field of view. Finally, we explain why our system has more degrees of freedom than conventional disordered media.

Any linear optical device can be described by a linear operator D which takes an input function $|\psi_o\rangle$ and generates a linear combination of modes $|\psi_i\rangle$, given as

$$|\psi_o\rangle = D |\psi_i\rangle. \quad (5.14)$$

We can always perform the SVD of D which yields

$$D = U\Sigma V^+, \quad (5.15)$$

where U and V are unitary matrices, and Σ is a diagonal matrix with complex values that describe the transmission coefficients for independent channels between the input and output modes. By multiplying U^+ from the left-hand side, we have

$$U^+ |\psi_o\rangle = \Sigma (V^+ |\psi_i\rangle). \quad (5.16)$$

The set of modes $U^+ |\psi_o\rangle$ and $V^+ |\psi_i\rangle$ that correspond with nonzero singular values in Σ form the orthogonal sets of basis modes in the output and input spaces.

Next, we consider the case where the linear device operator D represents a general phase mask, the input mode is a wavefront shaped by the SLM, and the output is the field at an arbitrary plane after passing through the phase mask. If the response of the phase mask is insensitive to input angle, the mask can be thought of as a device

which simply multiplies the input field $\psi_i(x, y)$ by a position-dependent transmission function $T(x, y)$ to obtain the output field $\psi_o(x, y)$ on the device output plane:

$$\psi_o(x, y) = T(x, y)\psi_i(x, y). \quad (5.17)$$

Writing this in matrix form yields

$$|\psi_o^p\rangle = D_{\text{mask}} |\psi_i^p\rangle, \quad (5.18)$$

where we can choose the orthogonal set of input modes as the SLM's pixels. No spatial overlap ensures the orthogonality of the modes. This orthogonality for the N modes holds only if the SLM has a pixel pitch larger than $\lambda/2$. If the pixel pitch is smaller than $\lambda/2$, we cannot count each pixel as an independent mode.

Since the transmission function of the phase mask is local, (i.e., the phase mask device operation connects an input at a given transverse position on the input plane with an output at the same transverse location on the output plane), the mask operator D_{mask} should be diagonal and full-rank in general. This “local” effect is not applicable in the case of volumetric scattering media, where an input mode can diffuse inside the media and form a speckle field as an output mode. We will come back to this point later on to compare the two cases. For the corresponding set of output modes $|\psi_o^p\rangle$, the mode orthogonality still holds because the locally transmitted output modes do not spatially overlap right after they are transmitted through the mask.

Describing the optical system of the phase mask and phase-only SLM in this fashion, we return to the SVD analysis for the system where D_{mask} is a diagonal matrix with the elements corresponding to the local transmission coefficients (or, transmission coefficients for the eigenchannels) and $|\psi_i^p\rangle$ and $|\psi_o^p\rangle$ are the pairs of the orthogonal input and output modes respectively. From this SVD analysis, we can see that the device operator (or TM) describing our proposed optical system is always full-rank and we have N degrees of freedom for the output modes as well. This statement is true however one designs the phase mask and however the bases are chosen.

For example, for our disordered metasurface phase mask, we know that plane wave illumination as an input mode can excite all the possible output plane waves nearly isotropically, as experimentally verified in Fig. 5.2(c). If we describe the system using plane waves as the bases and discretize the angle of the plane waves into M and N values for the output and input modes, where M is greater than N , we can describe the system in the form

$$|\psi_o'\rangle = D'_{\text{mask}} |\psi_i'\rangle, \quad (5.19)$$

where $|\psi'_i\rangle$ and $|\psi'_o\rangle$ are input and output plane wave modes, and D'_{mask} is another representation of the device operator D_{mask} . However, since the description of the system with the operator D_{mask} and the input and output sets of orthogonal modes $|\psi_i^P\rangle$ and $|\psi_o^P\rangle$ is a unique and complete characterization of the system, performing the SVD of D'_{mask} will result in the same full-rank diagonal matrix D_{mask} described above.

So far, we have considered only the linear system describing the field transformation before and after the phase mask. In our experimental scheme, light also propagates from the phase mask to the focal plane. However, free-space propagation can be considered by incorporating the free-space propagation operator, which does not degrade the full-rank operation since it is always full-rank as well.

Now we know that through the metasurface we can control N output modes because we have N degrees of freedom in the input. On the other hand, we also know that we can focus light to a large number of diffraction-limited spots using wavefront engineering (i.e., choosing the optimum phase for the N input modes in order to form constructive interference peaks at locations of interest). When a disordered medium is used in this way, it is called a “scattering lens”. If each resolvable focal spot in the output space is treated as one mode (the total number of which is defined as M according to the space–bandwidth product formalism in the main text), we would seemingly be able to achieve a number of degrees of freedom larger than the rank of our linear system. However, it is not valid to count each resolvable focal spot as an independent mode, because the focal spots created by the scattering lens have correlated, speckle-like backgrounds. Although the number of resolvable focal spots is not equivalent to the number of degrees of freedom, it is an important and useful parameter in many applications. In our focus-scanning scattering lens microscope, since the intensity of an achieved focal spot is significantly higher ($> 10^4$) than the background intensity, we can count the number of resolvable focal spots.

It is also worthwhile to analyze the number of degrees of freedom (or eigenchannels) supported by our disordered metasurface phase mask compared to conventional disordered media. For a conventional random medium, multiple scattering processes completely scramble the input modes and generate spatially extended speckle-fields as output modes. In contrast to the mask-based device, the device operator D_s (or TM, with $P = M \times N$ entries) of such a scattering medium is fully populated with complex entries. Similarly, performing the SVD of the TM reveals the number of independent channels for the disordered medium. The TM is generally not

full-rank ($\text{rank}(D_s) \leq \min(N, M)$), and it is well-known that the singular value distributions of volumetric disordered media statistically follow the “quarter-circle law”, experimentally confirmed by Popoff *et al.* [119]. Therefore, conventional disordered media deteriorate some degrees of freedom for the output modes, degrading the SNR and the focal contrast η . This means the advantage of replacing conventional disordered media with a disordered metasurface for wavefront shaping is not only that we can operate a scattering lens without characterizing the entire TM of the system, but also that the device operator does not deteriorate the supported degrees of freedom.

5.B Conventional Measurement of the Transmission Matrix

In previous reports, measurements of the TM have been performed in one of two ways. The first method can be implemented by displaying N orthogonal patterns on the SLM and recording the output field for each pattern [119, 120]. This approach can be understood as measuring the TM one column at a time, where each column corresponds to one SLM pattern, and each element in the column represents the output field contribution at a unique focal point on the projection plane. To focus to a given point on the projection plane, the pattern displayed on the SLM is selected as a linear combination of the SLM patterns such that the output field constructively interferes at the desired focal point. In the context of phase-only modulation, this means that the phase of each field vector, controlled by their respective pixels on the SLM, is aligned so as to maximize the sum over all the field vectors at that location. In order to enable focusing at all M focal spots, the output field for each SLM pattern must be measured at each of the M focal spot locations.

An alternate way to measure the TM is using optical phase conjugation [156]. This scheme is typically implemented by creating a calibration light focus from an external lens positioned at the desired focus location and recording the optical field transmitted in the reverse direction through the disordered medium toward the SLM. Then this procedure is repeated by scanning the focus to all M desired focal spots on the output plane. Mathematically, this approach can be interpreted as measuring the TM one row at a time, where the elements in each row describe the phase and amplitude relationship between a pixel on the SLM and the desired focal point.

While both of these approaches provide a way to characterize the TM of a disordered medium, they each suffer from practical limitations that prevent them from being practically useful for achieving control over large TMs ($P > 10^{12}$). These stem

from the sheer number of measurements and time required to characterize the TM. The first method is infeasible for large M due to the lack of commercially available camera sensors with the required number of pixels. Thus far, to the best of our knowledge, the largest reported TM measured using this method contained $P = 10^8$ elements. While the second method is not limited by the availability of the requisite technology, it requires mechanically scanning the focus to each spot. Assuming the relevant measurement technology existed for both cases, with a measurement speed of 10^8 measurements (i.e., TM elements) per second (equivalent to 5 megapixels at 100 frames per second), the measurement for all $P = 10^{13}$ elements in our demonstrated TM would require a measurement time of over 24 hours. To make matters worse, conventional disordered media used with wavefront engineering such as white paint made of TiO_2 or ZnO nanoparticles have a stability of only several hours [120, 132, 157], so the measured TM would be invalid by the time the measurement was complete.

5.C Immunofluorescence-Labeled Sample Preparation

As a biological sample, we use microscopic parasites, *Giardia lamblia* cysts (Waterborne, Inc.). Before labeling the Giardia, we first prepare (a) the sample of 10^5 Giardia in 10 μL phosphate buffered solution (PBS) in a centrifuge tube, (b) 1 μg of Giardia lamblia cysts antibody (Invitrogen, MA1-7441) in 100 μL PBS, and (c) 2 μg of Goat anti-Mouse IgG (H+L) Secondary Antibody conjugated with Alexa Fluor 532 fluorescent dye (Life Technologies, A-11002) in 100 μL of PBS. The sample (a) is incubated with a blocking buffer. After the blocking buffer is removed, the sample is again incubated with the Giardia antibody solution (b). The sample is rinsed twice with PBS to remove the Giardia antibody solution. The sample is then incubated with the secondary antibody solution with fluorescent dye (c). Finally, the sample is rinsed twice with PBS to remove the secondary antibody solution. All incubations are carried out for 30 min at 37°C . The sample in 10 μL PBS is prepared on a slide with Prolong Gold antifade reagent with DAPI (Life Technologies, P36935) to protect the labeled sample from fading and covered with a coverslip.

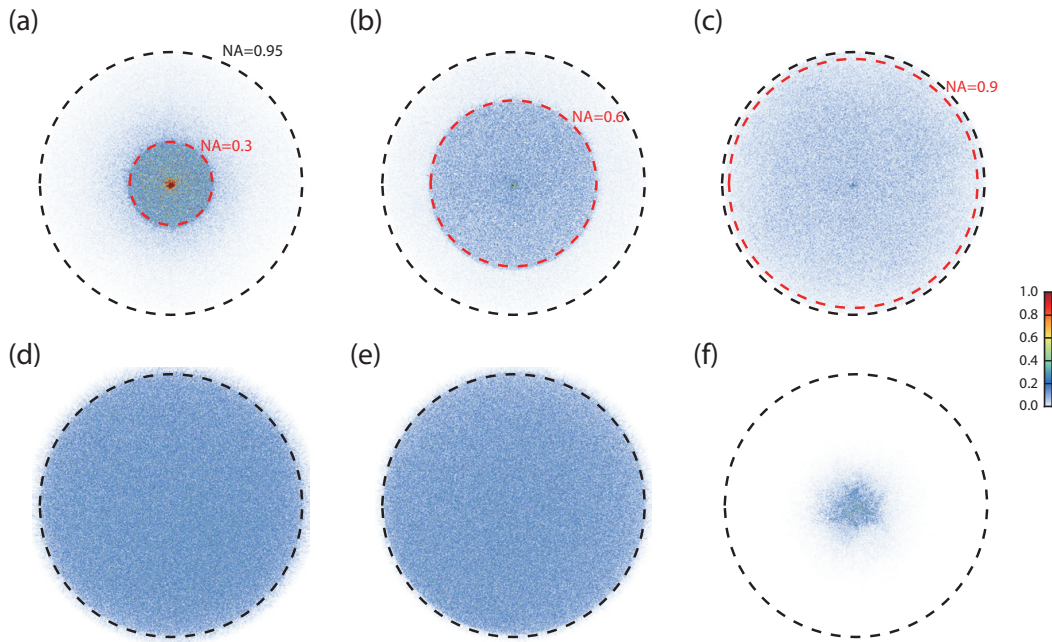


Figure 5.8: **Measured angular scattering profiles of disordered metasurfaces as well as those of conventional disordered media.** A collimated laser beam illuminated the scattering media and a $4-f$ system imaged the back focal plane of an objective lens ($NA = 0.95$) to a camera. (a-c) Angular scattering profiles of disordered metasurfaces with different designs, normalized to strongest scattered field component. The disordered metasurfaces were specifically designed such that they scatter the incident light to certain angular ranges of (a) $NA = 0.3$, (b) 0.6 , (c) 0.9 , which are denoted with red dotted lines. See also Fig. 5.2(c) for the scattering profiles of the disordered metasurface used in the experiment. (d-f) Angular scattering profiles of conventional scattering media. (d) The $20\text{-}\mu\text{m}$ -thick white paint (made of TiO_2 nanoparticles) and (e) opal glass diffuser (10DIFF-VIS, Newport) show isotropic scattering over the wide angular ranges, while (f) the ground glass diffuser (DG10-120, Thorlabs) has a very limited angular range for scattering. The black dotted lines correspond to the cutoff frequencies of the objective lens ($NA = 0.95$), which is the limit in our measurement setup.

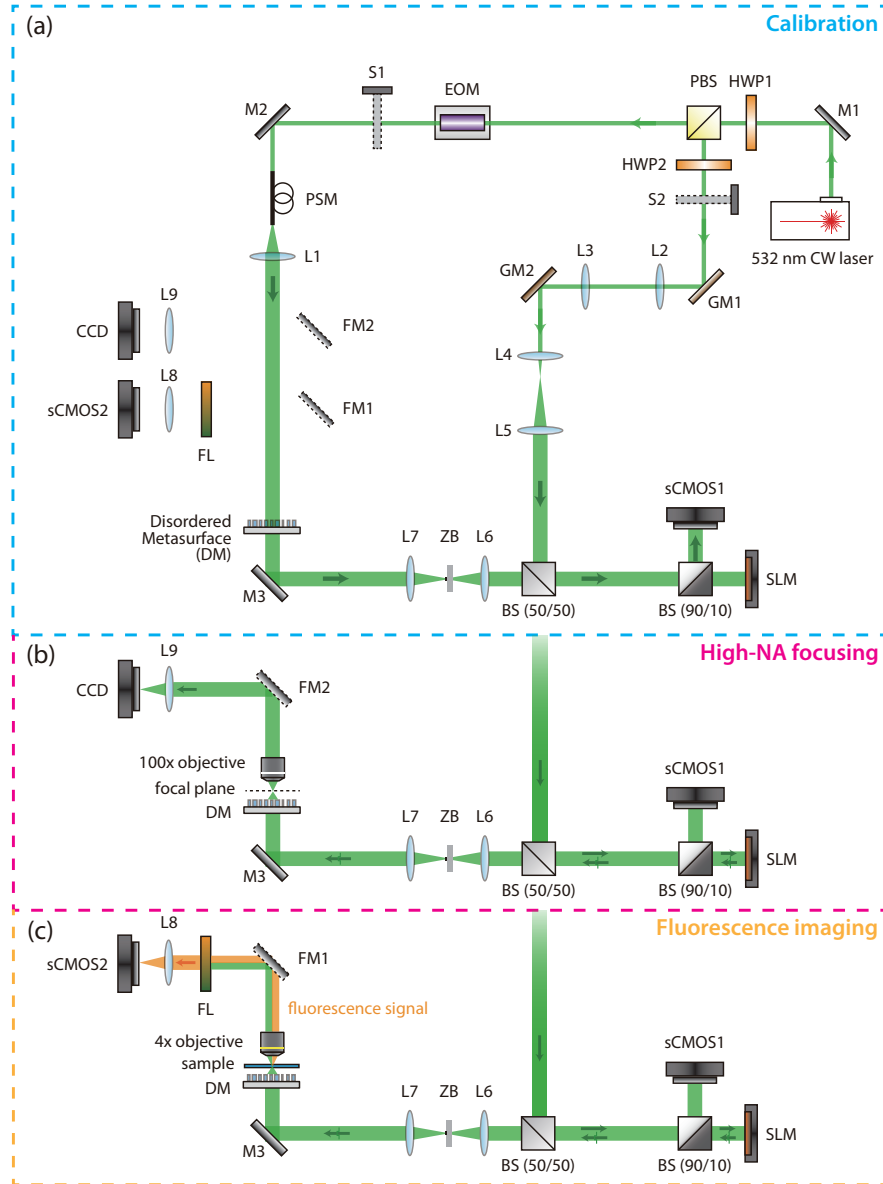


Figure 5.9: **Experimental setup for wavefront shaping with a disordered metasurface.** (a) Phase-shifting holography setup used for calibrating the alignment for the disordered metasurface and the SLM. (b) Custom-built microscope setup used for characterizing high-NA focusing over a wide-FOV. (c) Focus-scanning fluorescence imaging setup. M: mirror, L: lens, HWP: half-wave plate, PBS: polarizing beam splitter, S: shutter, EOM: electro-optic modulator, GM: galvanometric mirror, BS: beam splitter, sCMOS: scientific CMOS camera, CCD: CCD camera, SLM: spatial light modulator, ZB: zeroth-order block, DM: disordered metasurface, FM: flip mirror, PSM: polarization-maintaining single-mode fiber, FL: fluorescence filter.

CONCLUSION

6.1 Summary of Accomplishments

In this thesis, we explored the technological opportunities using high-contrast metastructures and their potential advantages over the conventionally existing optical components. In Chapter 1, we first elucidated the underlying physical principles of high-contrast metastructures, specifically in the form of a high-contrast subwavelength grating (SWG) that exhibits a broad reflection/transmission spectrum and an optical metasurface that allows for flexible wavefront engineering with subwavelength resolution. Despite their seemingly straightforward structure, high-contrast metastructures exhibit unique optical responses, benefitting from the interference effect due to the “multimode” nature in the waveguide geometry and the high refractive index contrast. We also studied that high-contrast structure allows us to think of each of high-index structures (e.g. high-index bars or posts) as local scatterers, enabling wavefront engineering by the structural modifications, namely an optical metasurface. In Chapter 2, we demonstrated a novel method to spatially vary the pass-bands of a Fabry–Perot filter set on a single substrate by the design of the high-contrast metastructures inside relatively high Q -factor resonators. We experimentally showed that the wavelength range that the filter set can cover was as large as $\Delta\lambda/\lambda = 16\%$ whereas measured Q -factor were greater than 10^3 . In Chapter 3, we designed a set of transmissive visible color filters toward miniaturizing on-chip RGB color filters used in complementary metal oxide transistor (CMOS) image sensors. We demonstrated that visible wavelength color filters based on high-contrast SWG can maintain its color filtering performance even when the pixel size becomes near a micron-size. In Chapter 4, we proposed a novel device concept of a phase-dominant modulator toward high-speed, phase-only spatial light modulator. Our concept relies on one-sided optical resonance, in which a high-contrast SWG is used to form a compact and highly reflective mirror. We formulated the condition for the dispersive phase response using the temporal coupled-mode theory. Active phase-dominant modulation was experimentally achieved by the refractive index modulation of silicon using thermo-optic effect. We also demonstrated a spatial light modulation capability by deploying a phased array using phase-dominant modulators on a silicon chip.

In Chapter 5, we proposed the concept of a disorder-engineered metasurface in the context of wavefront shaping. We exploited an engineered optical “randomness” using a metasurface platform, as an enabling technology to translate unprecedented wavefront manipulation capabilities in wavefront shaping into practical applications. We highlighted the unique optical properties of the disordered metasurfaces in contrast with conventional disordered media. We experimentally demonstrated the ability to perform high-NA optical focusing in a volumetric range. We furthermore applied this technique for wide-field high-resolution imaging of fluorescence samples.

6.2 Concluding Remarks

Looking forward, the works presented in this thesis represents merely a small portion of the potentials that high-contrast metastructures can demonstrate. As we see in Chapter 2, the inclusion of high-contrast metastructures in a high- Q resonator system may have an opportunity to design a new optical functionality in optical resonators or laser systems. Another direction in this field is a large-scale fabrication of such high-contrast structures. Even though high-contrast metastructures have a great potential for large-scale integration due to its compatibility with conventional wafer-scale fabrication techniques, most of the demonstrations so far still rely on an expensive electron beam lithography, rather than conventional photolithography. The adaption of a variety of lithographic techniques toward large-scale fabrication, such as deep-UV lithography, nanoimprint lithography and soft lithography, is highly anticipated. Lastly, the holy grail in wavefront engineering is the realization of a spatial light modulation device with a subwavelength pixel size. Metasurfaces are very promising in that they have shown to allow for arbitrary control for phase, amplitude, and polarization of the light with subwavelength resolution and high efficiency, but their functionalities are generally fixed at the moment of fabrication. As we discussed in Chapter 4, we can consider using varieties of exotic modulation scheme available in other physical systems, such as thermo-optic effect, electro-optic effect, microelectromechanical systems (MEMS) actuated structure, coupling with surface acoustic wave (SAW), and the use of liquid crystals.

BIBLIOGRAPHY

- [1] C. J. Chang-Hasnain and W. Yang, “High-contrast gratings for integrated optoelectronics”, *Adv. Opt. Photonics* **4**, 379–440 (2012) DOI: [10.1364/AOP.4.000379](https://doi.org/10.1364/AOP.4.000379) (cited on pp. 1, 3, 47).
- [2] N. Yu and F. Capasso, “Flat optics with designer metasurfaces”, *Nat. Mater.* **13**, 139–150 (2014) DOI: [10.1038/nmat3839](https://doi.org/10.1038/nmat3839) (cited on pp. 1, 15, 67).
- [3] M. L. Brongersma, Y. Cui, and S. Fan, “Light management for photovoltaics using high-index nanostructures”, *Nat. Mater.* **13**, 451–460 (2014) DOI: [10.1038/nmat3921](https://doi.org/10.1038/nmat3921) (cited on pp. 1, 29).
- [4] S. Jahani and Z. Jacob, “All-dielectric metamaterials”, *Nat. Nanotechnol.* **11**, 23–36 (2016) DOI: [10.1038/nnano.2015.304](https://doi.org/10.1038/nnano.2015.304) (cited on pp. 1, 15, 37).
- [5] I. Staude and J. Schilling, “Metamaterial-inspired silicon nanophotonics”, *Nat. Photon.* **11**, 274–284 (2017) DOI: [10.1038/nphoton.2017.39](https://doi.org/10.1038/nphoton.2017.39) (cited on p. 1).
- [6] P. Lalanne and P. Chavel, “Metalenses at visible wavelengths: past, present, perspectives”, *Laser Photonics Rev.* **11**, 1600295 (2017) DOI: [10.1002/lpor.201600295](https://doi.org/10.1002/lpor.201600295) (cited on p. 1).
- [7] C. F. R. Mateus, M. C. Y. Huang, Y. Deng, A. R. Neureuther, and C. J. Chang-Hasnain, “Ultrabroadband mirror using low-index cladded subwavelength grating”, *IEEE Photon. Technol. Lett.* **16**, 518–520 (2004) DOI: [10.1109/LPT.2003.821258](https://doi.org/10.1109/LPT.2003.821258) (cited on pp. 1, 7, 14, 17, 47).
- [8] C. F. Mateus, M. C. Huang, L. Chen, C. J. Chang-Hasnain, and Y. Suzuki, “Broad-band mirror (1.12–1.62 μm) using a subwavelength grating”, *IEEE Photon. Technol. Lett.* **16**, 1676–1678 (2004) DOI: [10.1109/LPT.2004.828514](https://doi.org/10.1109/LPT.2004.828514) (cited on p. 1).
- [9] Y. Kanamori, K. Hane, H. Sai, and H. Yugami, “100 nm period silicon antireflection structures fabricated using a porous alumina membrane mask”, *Appl. Phys. Lett.* **78**, 142–143 (2001) DOI: [10.1063/1.1339845](https://doi.org/10.1063/1.1339845) (cited on p. 1).
- [10] S. Astilean, P. Lalanne, P. Chavel, E. Cambril, and H. Launois, “High-efficiency subwavelength diffractive element patterned in a high-refractive-index material for 633 nm”, *Opt. Lett.* **23**, 552–554 (1998) DOI: [10.1364/OL.23.000552](https://doi.org/10.1364/OL.23.000552) (cited on p. 1).
- [11] D. Fattal, J. Li, Z. Peng, M. Fiorentino, and R. G. Beausoleil, “Flat dielectric grating reflectors with focusing abilities”, *Nat. Photon.* **4**, 466–470 (2010) DOI: [10.1038/nphoton.2010.116](https://doi.org/10.1038/nphoton.2010.116) (cited on pp. 1, 8, 14, 17, 27, 37, 47, 78).

- [12] F. Lu, F. G. Sedgwick, V. Karagodsky, C. Chase, and C. J. Chang-Hasnain, “Planar high-numerical-aperture low-loss focusing reflectors and lenses using subwavelength high contrast gratings.”, *Opt. Express* **18**, 12606–12614 (2010) DOI: [10.1364/OE.18.012606](https://doi.org/10.1364/OE.18.012606) (cited on pp. 1, 37).
- [13] S. Vo, D. Fattal, W. V. Sorin, Z. Peng, T. Tran, M. Fiorentino, and R. G. Beausoleil, “Sub-wavelength grating lenses with a twist”, *IEEE Photon. Technol. Lett.* **26**, 1375–1378 (2014) DOI: [10.1109/LPT.2014.2325947](https://doi.org/10.1109/LPT.2014.2325947) (cited on pp. 1, 16, 17, 78).
- [14] D. Lin, P. Fan, E. Hasman, and M. L. Brongersma, “Dielectric gradient metasurface optical elements”, *Science* **345**, 298–302 (2014) DOI: [10.1126/science.1253213](https://doi.org/10.1126/science.1253213) (cited on pp. 1, 16, 67).
- [15] A. Arbabi, Y. Horie, A. J. Ball, M. Bagheri, and A. Faraon, “Subwavelength-thick lenses with high numerical apertures and large efficiency based on high contrast transmitarrays”, *Nat. Commun.* **6**, 7069 (2015) DOI: [10.1038/ncomms8069](https://doi.org/10.1038/ncomms8069) (cited on pp. 1, 9, 16, 17, 37, 67, 78).
- [16] A. Arbabi, Y. Horie, M. Bagheri, and A. Faraon, “Dielectric metasurfaces for complete control of phase and polarization with subwavelength spatial resolution and high transmission”, *Nat. Nanotechnol.* **10**, 937–943 (2015) DOI: [10.1038/nnano.2015.186](https://doi.org/10.1038/nnano.2015.186) (cited on pp. 1, 9, 16, 37, 78).
- [17] E. Hecht, *Optics, 5th Edition* (Pearson, 2016) (cited on p. 1).
- [18] D. L. Brundrett, E. N. Glytsis, and T. K. Gaylord, “Homogeneous layer models for high-spatial-frequency dielectric surface-relief gratings: conical diffraction and antireflection designs”, *Appl. Opt.* **33**, 2695–2706 (1994) DOI: [10.1364/AO.33.002695](https://doi.org/10.1364/AO.33.002695) (cited on pp. 1, 17).
- [19] P. Lalanne and D. Lemerrier-Lalanne, “On the effective medium theory of subwavelength periodic structures”, *J. Mod. Opt.* **43**, 2063–2086 (1996) DOI: [10.1080/09500349608232871](https://doi.org/10.1080/09500349608232871) (cited on p. 1).
- [20] A. A. Krokhin, P. Halevi, and J. Arriaga, “Long-wavelength limit (homogenization) for two-dimensional photonic crystals”, *Phys. Rev. B* **65**, 115208 (2002) DOI: [10.1103/PhysRevB.65.115208](https://doi.org/10.1103/PhysRevB.65.115208) (cited on p. 1).
- [21] H. Kikuta, Y. Ohira, and K. Iwata, “Achromatic quarter-wave plates using the dispersion of form birefringence”, *Appl. Opt.* **36**, 1566–1572 (1997) DOI: [10.1364/AO.36.001566](https://doi.org/10.1364/AO.36.001566) (cited on p. 3).
- [22] P. Lalanne, J. P. Hugonin, and P. Chavel, “Optical properties of deep lamellar gratings: a coupled Bloch-mode insight”, *J. Light. Technol.* **24**, 2442–2449 (2006) DOI: [10.1109/JLT.2006.874555](https://doi.org/10.1109/JLT.2006.874555) (cited on pp. 3, 14, 17, 47).
- [23] V. Karagodsky, F. G. Sedgwick, and C. J. Chang-Hasnain, “Theoretical analysis of subwavelength high contrast grating reflectors”, *Opt. Express* **18**, 16973–16988 (2010) DOI: [10.1364/OE.18.016973](https://doi.org/10.1364/OE.18.016973) (cited on pp. 3, 17, 47).

- [24] V. Karagodsky and C. J. Chang-Hasnain, “Physics of near-wavelength high contrast gratings”, *Opt. Express* **20**, 10888–10895 (2012) DOI: [10.1364/OE.20.010888](https://doi.org/10.1364/OE.20.010888) (cited on pp. 3, 17).
- [25] H. A. Haus, *Waves and Fields in Optoelectronics* (Prentice-Hall, 1983) (cited on pp. 3, 4, 43).
- [26] A. Yariv and P. Yeh, *Photonics: Optical Electronics in Modern Communications* (Oxford University Press, 2007) (cited on pp. 3, 27, 43).
- [27] W. Suh, Z. Wang, and S. Fan, “Temporal coupled-mode theory and the presence of non-orthogonal modes in lossless multimode cavities”, *IEEE J. Quant. Electron.* **40**, 1511–1518 (2004) DOI: [10.1109/JQE.2004.834773](https://doi.org/10.1109/JQE.2004.834773) (cited on p. 4).
- [28] V. Liu and S. Fan, “S4: A free electromagnetic solver for layered periodic structures”, *Comput. Phys. Commun.* **183**, 2233–2244 (2012) DOI: [10.1016/j.cpc.2012.04.026](https://doi.org/10.1016/j.cpc.2012.04.026) (cited on pp. 5, 17, 46).
- [29] M. C. Huang, Y. Zhou, and C. J. Chang-Hasnain, “A surface-emitting laser incorporating a high-index-contrast subwavelength grating”, *Nat. Photon.* **1**, 119–122 (2007) DOI: [10.1038/nphoton.2006.80](https://doi.org/10.1038/nphoton.2006.80) (cited on p. 7).
- [30] M. C. Y. Huang, Y. Zhou, and C. J. Chang-Hasnain, “A nanoelectromechanical tunable laser”, *Nat. Photon.* **2**, 180–184 (2008) DOI: [10.1038/nphoton.2008.3](https://doi.org/10.1038/nphoton.2008.3) (cited on p. 7).
- [31] B.-W. Yoo, M. Megens, T. Chan, T. Sun, W. Yang, C. J. Chang-Hasnain, D. A. Horsley, and M. C. Wu, “Optical phased array using high contrast gratings for two dimensional beamforming and beamsteering”, *Opt. Express* **21**, 12238–12248 (2013) DOI: [10.1364/OE.21.012238](https://doi.org/10.1364/OE.21.012238) (cited on p. 7).
- [32] T. K. Chan, M. Megens, B.-W. Yoo, J. Wyras, C. J. Chang-Hasnain, M. C. Wu, and D. A. Horsley, “Optical beamsteering using an 8×8 MEMS phased array with closed-loop interferometric phase control”, *Opt. Express* **21**, 2807–2815 (2013) DOI: [10.1364/OE.21.002807](https://doi.org/10.1364/OE.21.002807) (cited on p. 7).
- [33] B.-W. Yoo, M. Megens, T. Sun, W. Yang, C. J. Chang-Hasnain, D. A. Horsley, and M. C. Wu, “A 32×32 optical phased array using polysilicon sub-wavelength high-contrast-grating mirrors”, *Opt. Express* **22**, 19029–19039 (2014) DOI: [10.1364/OE.22.019029](https://doi.org/10.1364/OE.22.019029) (cited on p. 7).
- [34] W. Yang, T. Sun, Y. Rao, M. Megens, T. Chan, B.-W. Yoo, D. A. Horsley, M. C. Wu, and C. J. Chang-Hasnain, “High speed optical phased array using high contrast grating all-pass filters”, *Opt. Express* **22**, 20038–20044 (2014) DOI: [10.1364/OE.22.020038](https://doi.org/10.1364/OE.22.020038) (cited on pp. 7, 42).
- [35] W. Yang, S. A. Gerke, K. W. Ng, Y. Rao, C. Chase, and C. J. Chang-Hasnain, “Laser optomechanics”, *Sci. Rep.* **5**, 13700 (2015) DOI: [10.1038/srep13700](https://doi.org/10.1038/srep13700) (cited on p. 7).

- [36] J. D. Joannopoulos, S. G. Johnson, J. N. Winn, and R. D. Meade, *Photonic Crystals: Molding the Flow of Light* (Princeton University Press, 2008) (cited on p. 7).
- [37] D. D. O'Shea, T. J. Suleski, A. D. Kathman, and D. W. Praather, *Diffraction Optics: Design, Fabrication, and Test* (SPIE Press, 2003) (cited on p. 9).
- [38] G. Minas, R. F. Wolffenbuttel, and J. H. Correia, "A lab-on-a-chip for spectrophotometric analysis of biological fluids", *Lab Chip* **5**, 1303–1209 (2005) DOI: [10.1039/b506817g](https://doi.org/10.1039/b506817g) (cited on p. 13).
- [39] C. P. Bacon, Y. Mattley, and R. DeFrece, "Miniature spectroscopic instrumentation: Applications to biology and chemistry", *Rev. Sci. Instrum.* **75**, 1–16 (2004) DOI: [10.1063/1.1633025](https://doi.org/10.1063/1.1633025) (cited on p. 13).
- [40] R. F. Wolffenbuttel, "MEMS-based optical mini- and microspectrometers for the visible and infrared spectral range", *J. Micromech. Microeng.* **15**, S145–S152 (2005) DOI: [10.1088/0960-1317/15/7/021](https://doi.org/10.1088/0960-1317/15/7/021) (cited on p. 13).
- [41] Z. Xia, A. A. Eftekhari, M. Soltani, B. Momeni, Q. Li, M. Chamanzar, S. Yegnanarayanan, and A. Adibi, "High resolution on-chip spectroscopy based on miniaturized microdonut resonators", *Opt. Express* **19**, 12356–12364 (2011) DOI: [10.1364/OE.19.012356](https://doi.org/10.1364/OE.19.012356) (cited on p. 13).
- [42] B. Kyotoku, L. Chen, and M. Lipson, "Sub-nm resolution cavity enhanced microspectrometer", *Opt. Express* **18**, 102–107 (2010) DOI: [10.1364/OE.18.000102](https://doi.org/10.1364/OE.18.000102) (cited on p. 13).
- [43] P. Cheben, J. H. Schmid, A. Delâge, A. Densmore, S. Janz, B. Lamontagne, J. Lapointe, E. Post, P. Waldron, and D.-X. Xu, "A high-resolution silicon-on-insulator arrayed waveguide grating microspectrometer with sub-micrometer aperture waveguides", *Opt. Express* **15**, 2299–2306 (2007) DOI: [10.1364/OE.15.002299](https://doi.org/10.1364/OE.15.002299) (cited on p. 13).
- [44] S.-W. Wang, C. Xia, X. Chen, W. Lu, M. Li, H. Wang, W. Zheng, and T. Zhang, "Concept of a high-resolution miniature spectrometer using an integrated filter array", *Opt. Lett.* **32**, 632–634 (2007) DOI: [10.1364/OL.32.000632](https://doi.org/10.1364/OL.32.000632) (cited on p. 13).
- [45] J. H. Correia, M. Bartek, and R. F. Wolffenbuttel, "High-selectivity single-chip spectrometer in silicon for operation at visible part of the spectrum", *IEEE Trans. Electron Dev.* **47**, 553–559 (2000) DOI: [10.1109/16.824727](https://doi.org/10.1109/16.824727) (cited on p. 13).
- [46] A. Emadi, H. Wu, G. de Graaf, and R. Wolffenbuttel, "Design and implementation of a sub-nm resolution microspectrometer based on a Linear-Variable Optical Filter", *Opt. Express* **20**, 489–507 (2012) DOI: [10.1364/OE.20.000489](https://doi.org/10.1364/OE.20.000489) (cited on p. 13).

- [47] N. A. O'Brien, C. A. Hulse, D. M. Friedrich, F. J. Van Milligen, M. K. von Gunten, F. Pfeifer, and H. W. Siesler, "Miniature near-infrared (NIR) spectrometer engine for handheld applications", in *Proc. SPIE*, Vol. 8374 (2012), p. 837404, DOI: [10.1117/12.917983](https://doi.org/10.1117/12.917983) (cited on pp. 13, 14).
- [48] *MicroNIR Spectrometer, Viavi Solutions Inc.* URL: <https://www.viavisolutions.com/en-us/osp/products/micronir-spectrometers> (visited on 07/14/2017) (cited on pp. 13, 14).
- [49] J. Xiao, F. Song, K. Han, and S.-W. Seo, "Fabrication of CMOS-compatible optical filter arrays using gray-scale lithography", *J. Micromechanics Micro-engineering* **22**, 025006 (2012) DOI: [10.1088/0960-1317/22/2/025006](https://doi.org/10.1088/0960-1317/22/2/025006) (cited on p. 13).
- [50] C. Sciancalepore, B. Ben Bakir, S. Menezo, X. Letartre, D. Bordel, and P. Viktorovitch, "III-V-on-Si photonic crystal vertical-cavity surface-emitting laser arrays for wavelength division multiplexing", *IEEE Photon. Technol. Lett.* **25**, 1111–1113 (2013) DOI: [10.1109/LPT.2013.2260140](https://doi.org/10.1109/LPT.2013.2260140) (cited on p. 15).
- [51] J. B. Khurgin, "How to deal with the loss in plasmonics and metamaterials", *Nat. Nanotechnol.* **10**, 2–6 (2015) DOI: [10.1038/nnano.2014.310](https://doi.org/10.1038/nnano.2014.310) (cited on p. 16).
- [52] K. Walls, Q. Chen, J. Grant, S. Collins, D.R.S. Cumming, and T.D. Drysdale, "Narrowband multispectral filter set for visible band", *Opt. Express* **20**, 21917–21923 (2012) DOI: [10.1364/OE.20.021917](https://doi.org/10.1364/OE.20.021917) (cited on p. 16).
- [53] S. Kaushik and B. R. Stallard, "Two-dimensional array of optical interference filters produced by lithographic alterations of the index of refraction", in *Proc. SPIE*, Vol. 2532 (1995), p. 276, DOI: [10.1117/12.221254](https://doi.org/10.1117/12.221254) (cited on p. 16).
- [54] S. Boutami, B. Benbakir, X. Letartre, J. L. Leclercq, P. Regreny, and P. Viktorovitch, "Ultimate vertical Fabry-Perot cavity based on single-layer photonic crystal mirrors", *Opt. Express* **15**, 12443–12449 (2007) DOI: [10.1364/OE.15.012443](https://doi.org/10.1364/OE.15.012443) (cited on p. 18).
- [55] A. Ricciardi, S. Campopiano, A. Cusano, T. F. Krauss, and L. O'Faolain, "Broadband mirrors in the near-infrared based on subwavelength gratings in SOI", *IEEE Photonics J.* **2**, 696–702 (2010) DOI: [10.1109/JPHOT.2010.2059003](https://doi.org/10.1109/JPHOT.2010.2059003) (cited on p. 20).
- [56] Z. Qiang, H. Yang, S. Chuwongin, D. Zhao, Z. Ma, and W. Zhou, "Design of Fano broadband reflectors on SOI", *IEEE Photon. Technol. Lett.* **22**, 1108–1110 (2010) DOI: [10.1109/LPT.2010.2050471](https://doi.org/10.1109/LPT.2010.2050471) (cited on p. 20).
- [57] M. Shokooh-Saremi and R. Magnusson, "Properties of two-dimensional resonant reflectors with zero-contrast gratings", *Opt. Lett.* **39**, 6958–6961 (2014) DOI: [10.1364/OL.39.006958](https://doi.org/10.1364/OL.39.006958) (cited on p. 20).

- [58] C. Sciancalepore, B. B. Bakir, X. Letartre, J. M. Fedeli, N. Olivier, D. Bordel, C. Seassal, P. Rojo-Romeo, P. Regreny, and P. Viktorovitch, “Quasi-3D light confinement in double photonic crystal reflectors VCSELs for CMOS-compatible integration”, *J. Light. Technol.* **29**, 2015–2024 (2011) DOI: [10.1109/JLT.2011.2157303](https://doi.org/10.1109/JLT.2011.2157303) (cited on pp. 20, 54).
- [59] J. Li, D. Fattal, M. Fiorentino, and R. G. Beausoleil, “Strong optical confinement between nonperiodic flat dielectric gratings”, *Phys. Rev. Lett.* **106**, 193901 (2011) DOI: [10.1103/PhysRevLett.106.193901](https://doi.org/10.1103/PhysRevLett.106.193901) (cited on pp. 20, 27, 54).
- [60] Z. Wang, B. Zhang, and H. Deng, “Dispersion engineering for vertical microcavities using subwavelength gratings”, *Phys. Rev. Lett.* **114**, 073601 (2015) DOI: [10.1103/PhysRevLett.114.073601](https://doi.org/10.1103/PhysRevLett.114.073601) (cited on p. 27).
- [61] E. Arbabi, A. Arbabi, S. M. Kamali, Y. Horie, and A. Faraon, “Controlling the sign of chromatic dispersion in diffractive optics”, *Optica* **4**, 625–632 (2017) DOI: [10.1364/OPTICA.4.000625](https://doi.org/10.1364/OPTICA.4.000625) (cited on p. 27).
- [62] H. Lin, X. Sun, J. Liu, and J. Hu, “Diffractive broadband coupling into high-Q resonant cavities”, *Opt. Lett.* **40**, 2377–2380 (2015) DOI: [10.1364/OL.40.002377](https://doi.org/10.1364/OL.40.002377) (cited on p. 27).
- [63] J. Ahn, C.-R. Moon, B. Kim, K. Lee, Y. Kim, M. Lim, W. Lee, H. Park, K. Moon, J. Yoo, Y. Y. Y. Lee, B. Park, S. Jung, J. Lee, T.-H. Lee, Y. Y. Y. Lee, J. Jung, J.-H. Kim, T.-C. Kim, H. Cho, D. Lee, and Y. Y. Y. Lee, “Advanced image sensor technology for pixel scaling down toward 1.0 μm ”, in *IEEE International Electron Devices Meeting* (2008), pp. 1–4, DOI: [10.1109/IEDM.2008.4796671](https://doi.org/10.1109/IEDM.2008.4796671) (cited on p. 28).
- [64] P. B. Catrysse, “Roadmap for CMOS image sensors: Moore meets Planck and Sommerfeld”, in *Proc. SPIE*, Vol. 5678 (2005), pp. 1–13, DOI: [10.1117/12.592483](https://doi.org/10.1117/12.592483) (cited on p. 29).
- [65] M. Kriss, *Handbook of Digital Imaging* (Wiley, 2015), DOI: [10.1002/9781118798706](https://doi.org/10.1002/9781118798706) (cited on p. 29).
- [66] Y. Yu, L. Wen, S. Song, and Q. Chen, “Transmissive/reflective structural color filters: Theory and applications”, *J. Nanomater.* **2014**, 1–17 (2014) DOI: [10.1155/2014/212637](https://doi.org/10.1155/2014/212637) (cited on p. 29).
- [67] S. Yokogawa, S. P. Burgos, and H. A. Atwater, “Plasmonic color filters for CMOS image sensor applications”, *Nano Lett.* **12**, 4349–4354 (2012) DOI: [10.1021/nl302110z](https://doi.org/10.1021/nl302110z) (cited on p. 29).
- [68] H. Park, Y. Dan, K. Seo, Y. J. Yu, P. K. Duane, M. Wober, and K. B. Crozier, “Filter-free image sensor pixels comprising silicon nanowires with selective color absorption”, *Nano Lett.* **14**, 1804–1809 (2014) DOI: [10.1021/nl404379w](https://doi.org/10.1021/nl404379w) (cited on p. 29).

- [69] Y. Huo, C. C. Fesenmaier, and P. B. Catrysse, “Microlens performance limits in sub-2 μm pixel CMOS image sensors”, *Opt. Express* **18**, 5861–5872 (2010) DOI: [10.1364/OE.18.005861](https://doi.org/10.1364/OE.18.005861) (cited on p. 29).
- [70] L. Frey, P. Parrein, J. Raby, C. Pellé, D. Hérault, M. Marty, and J. Michailos, “Color filters including infrared cut-off integrated on CMOS image sensor”, *Opt. Express* **19**, 13073–13080 (2011) DOI: [10.1364/OE.19.013073](https://doi.org/10.1364/OE.19.013073) (cited on p. 29).
- [71] Q. Chen, D. Chitnis, K. Walls, T. D. Drysdale, S. Collins, and D. R. S. Cumming, “CMOS photodetectors integrated with plasmonic color filters”, *IEEE Photonics Technol. Lett.* **24**, 197–199 (2012) DOI: [10.1109/LPT.2011.2176333](https://doi.org/10.1109/LPT.2011.2176333) (cited on p. 29).
- [72] S. P. Burgos, S. Yokogawa, and H. A. Atwater, “Color imaging via nearest neighbor hole coupling in plasmonic color filters integrated onto a complementary metal-oxide semiconductor image sensor”, *ACS Nano* **7**, 10038–10047 (2013) DOI: [10.1021/nm403991d](https://doi.org/10.1021/nm403991d) (cited on p. 29).
- [73] L. Cao, P. Fan, E. S. Barnard, A. M. Brown, and M. L. Brongersma, “Tuning the color of silicon nanostructures”, *Nano Lett.* **10**, 2649–2654 (2010) DOI: [10.1021/nl1013794](https://doi.org/10.1021/nl1013794) (cited on p. 29).
- [74] J. Proust, F. Bedu, B. Gallas, I. Ozerov, and N. Bonod, “All-dielectric colored metasurfaces with silicon mie resonators”, *ACS Nano* **10**, 7761–7767 (2016) DOI: [10.1021/acsnano.6b03207](https://doi.org/10.1021/acsnano.6b03207) (cited on p. 29).
- [75] V. Vashistha, G. Vaidya, P. Gruszecki, A. E. Serebryannikov, and M. Krawczyk, “All-dielectric metasurfaces based on cross-shaped resonators for color pixels with extended gamut”, *ACS Photonics* **4**, 1076–1082 (2017) DOI: [10.1021/acsp Photonics.6b00853](https://doi.org/10.1021/acsp Photonics.6b00853) (cited on p. 29).
- [76] Y. Kanamori, M. Shimono, and K. Hane, “Fabrication of transmission color filters using silicon subwavelength gratings on quartz substrates”, *IEEE Photon. Technol. Lett.* **18**, 2126–2128 (2006) DOI: [10.1109/LPT.2006.883208](https://doi.org/10.1109/LPT.2006.883208) (cited on p. 29).
- [77] Y. Kanamori, T. Ozaki, and K. Hane, “Reflection color filters of the three primary colors with wide viewing angles using common-thickness silicon subwavelength gratings”, *Opt. Express* **2122**, 25663–25672 (2014) DOI: [10.1364/OE.22.025663](https://doi.org/10.1364/OE.22.025663) (cited on p. 29).
- [78] Y. Kanamori, M. Sasaki, and K. Hane, “Broadband antireflection gratings fabricated upon silicon substrates”, *Opt. Lett.* **24**, 1422–1424 (1999) DOI: [10.1364/OL.24.001422](https://doi.org/10.1364/OL.24.001422) (cited on p. 29).
- [79] J. Proust, A.-L. Fehrembach, F. Bedu, I. Ozerov, and N. Bonod, “Optimized 2D array of thin silicon pillars for efficient antireflective coatings in the visible spectrum”, *Sci. Rep.* **6**, 24947 (2016) DOI: [10.1038/srep24947](https://doi.org/10.1038/srep24947) (cited on p. 29).

- [80] E. C. Regan, Y. Shen, A. Massuda, O. D. Miller, and M. Soljacic, “Silicon color filters for light-recycling displays”, (2016), [arXiv:1611.00681](https://arxiv.org/abs/1611.00681), URL: <http://arxiv.org/abs/1611.00681> (cited on p. 29).
- [81] J. Alakarhu, “Image sensors and image quality in mobile phones”, in Proc. International Image Sensor Workshop (2007), pp. 1–4 (cited on p. 30).
- [82] R. H. Buitrago, G. A. Risso, M. Cutrera, M. Battioni, L. D. Bernardez, J. A. Schmidt, R. D. Arce, and R. R. Koropecski, “Polycrystalline silicon thin film solar cells prepared by PECVD-SPC”, *Int. J. Hydrogen Energy* **33**, 3522–3525 (2008) DOI: [10.1016/j.ijhydene.2008.03.040](https://doi.org/10.1016/j.ijhydene.2008.03.040) (cited on p. 32).
- [83] R. Ruther, J. Livingstone, and N. Dytlewski, “Large-grain polycrystalline silicon thin films obtained by low-temperature stepwise annealing of hydrogenated amorphous silicon”, *Thin Solid Films* **310**, 67–74 (1997) DOI: [10.1016/S0040-6090\(97\)00362-3](https://doi.org/10.1016/S0040-6090(97)00362-3) (cited on p. 32).
- [84] K. Preston, B. Schmidt, and M. Lipson, “Polysilicon photonic resonators for large-scale 3D integration of optical networks”, *Opt. Express* **15**, 17283–17290 (2007) DOI: [10.1364/OE.15.017283](https://doi.org/10.1364/OE.15.017283) (cited on p. 32).
- [85] S. Zhu, Q. Fang, M. B. Yu, G. Q. Lo, and D. L. Kwong, “Propagation losses in undoped and n-doped polycrystalline silicon wire waveguides”, *Opt. Express* **17**, 20891–20899 (2009) DOI: [10.1364/OE.17.020891](https://doi.org/10.1364/OE.17.020891) (cited on p. 32).
- [86] J. Lee, B. Song, J. Kim, C.-W. Lee, S. Han, C.-W. Baik, H. Jeong, Y. Kim, and C. S. Lee, “Nanofabrication of low extinction coefficient and high-aspect-ratio Si structures for metaphotonic applications”, in Proc. SPIE, Vol. 9927 (2016), p. 992708, DOI: [10.1117/12.2235523](https://doi.org/10.1117/12.2235523) (cited on p. 37).
- [87] M. A. Green, “Self-consistent optical parameters of intrinsic silicon at 300K including temperature coefficients”, *Sol. Energ. Mat. Sol. Cells* **92**, 1305–1310 (2008) DOI: [10.1016/j.solmat.2008.06.009](https://doi.org/10.1016/j.solmat.2008.06.009) (cited on p. 40).
- [88] U. Efron, *Spatial Light Modulator Technology: Materials, Devices and Applications* (Marcel Dekker, 1994) (cited on p. 41).
- [89] B. Schwarz, “LIDAR: Mapping the world in 3D”, *Nat. Photon.* **4**, 429–430 (2010) DOI: [10.1038/nphoton.2010.148](https://doi.org/10.1038/nphoton.2010.148) (cited on p. 41).
- [90] V. Ntziachristos, “Going deeper than microscopy: the optical imaging frontier in biology”, *Nat. Methods* **7**, 603–614 (2010) DOI: [10.1038/nmeth.1483](https://doi.org/10.1038/nmeth.1483) (cited on p. 41).
- [91] Z. Zhang, Z. You, and D. Chu, “Fundamentals of phase-only liquid crystal on silicon (LCOS) devices”, *Light Sci. Appl.* **3**, e213 (2014) DOI: [10.1038/lssa.2014.94](https://doi.org/10.1038/lssa.2014.94) (cited on p. 42).
- [92] D. Engström, M. J. O’Callaghan, C. Walker, and M. A. Handschy, “Fast beam steering with a ferroelectric-liquid-crystal optical phased array”, *Appl. Opt.* **48**, 1721 (2009) DOI: [10.1364/AO.48.001721](https://doi.org/10.1364/AO.48.001721) (cited on p. 42).

- [93] B. Wang, G. Zhang, A. Glushchenko, J. L. West, P. J. Bos, and P. F. McManamon, “Stressed liquid-crystal optical phased array for fast tip-tilt wavefront correction”, *Appl. Opt.* **44**, 7754–7759 (2005) DOI: [10.1364/AO.44.007754](https://doi.org/10.1364/AO.44.007754) (cited on p. 42).
- [94] D. Dudley, W. M. Duncan, and J. Slaughter, “Emerging digital micromirror device (DMD) applications”, in *Proc. SPIE*, Vol. 4985 (2003), pp. 14–25, DOI: [10.1117/12.480761](https://doi.org/10.1117/12.480761) (cited on p. 42).
- [95] V. Shrauger and C. Warde, “Development of a high-speed high-fill-factor phase-only spatial light modulator”, *Proc. SPIE* **4291**, 101–108 (2001) DOI: [10.1117/12.424843](https://doi.org/10.1117/12.424843) (cited on p. 42).
- [96] R. A. Soref and B. R. Bennett, “Electro-optic Fabry-Perot pixels for phase-dominant spatial light modulators”, *Appl. Opt.* **31**, 675–680 (1992) DOI: [10.1364/AO.31.000675](https://doi.org/10.1364/AO.31.000675) (cited on p. 43).
- [97] D. Zhao, Z. Ma, and W. Zhou, “Field penetrations in photonic crystal Fano reflectors”, *Opt. Express* **18**, 14152–14158 (2010) DOI: [10.1364/OE.18.014152](https://doi.org/10.1364/OE.18.014152) (cited on p. 47).
- [98] B. J. Frey, D. B. Leviton, and T. J. Madison, “Temperature-dependent refractive index of silicon and germanium”, in *Proc. SPIE*, Vol. 6273 (2006), 62732J, DOI: [10.1117/12.672850](https://doi.org/10.1117/12.672850) (cited on p. 47).
- [99] A. H. Atabaki, E. Shah Hosseini, A. A. Eftekhar, S. Yegnanarayanan, and A. Adibi, “Optimization of metallic microheaters for high-speed reconfigurable silicon photonics”, *Opt. Express* **18**, 18312–18323 (2010) DOI: [10.1364/OE.18.018312](https://doi.org/10.1364/OE.18.018312) (cited on p. 53).
- [100] M. W. Geis, S. J. Spector, R. C. Williamson, and T. M. Lyszczarz, “Submicrosecond submilliwatt silicon-on-insulator thermo-optic switch”, *IEEE Photon. Technol. Lett.* **16**, 2514–2516 (2004) DOI: [10.1109/LPT.2004.835194](https://doi.org/10.1109/LPT.2004.835194) (cited on p. 53).
- [101] R. A. Soref and B. R. Bennett, “Electro-optical effects in silicon”, *IEEE J. Quant. Electron.* **23**, 123–129 (1987) DOI: [10.1109/JQE.1987.1073206](https://doi.org/10.1109/JQE.1987.1073206) (cited on p. 53).
- [102] G. T. Reed, G. Mashanovich, F. Y. Gardes, and D. J. Thomson, “Silicon optical modulators”, *Nat. Photon.* **4**, 518–526 (2010) DOI: [10.1038/nphoton.2010.179](https://doi.org/10.1038/nphoton.2010.179) (cited on p. 53).
- [103] C. Qiu, J. Chen, Y. Xia, and Q. Xu, “Active dielectric antenna on chip for spatial light modulation”, *Sci. Rep.* **2**, 855 (2012) DOI: [10.1038/srep00855](https://doi.org/10.1038/srep00855) (cited on p. 53).
- [104] E. Timurdogan, C. V. Poulton, M. J. Byrd, and M. R. Watts, “Electric field-induced second-order nonlinear optical effects in silicon waveguides”, *Nat. Photon.* **11**, 200–206 (2017) DOI: [10.1038/nphoton.2017.14](https://doi.org/10.1038/nphoton.2017.14) (cited on p. 53).

- [105] J. W. Goodman, *Introduction to Fourier Optics* (McGraw-Hill, 2004) (cited on p. 53).
- [106] C. Chase, Y. Zhou, and C. J. Chang-Hasnain, “Size effect of high contrast gratings in VCSELs”, *Opt. Express* **17**, 24002–24007 (2009) DOI: [10.1364/OE.17.024002](https://doi.org/10.1364/OE.17.024002) (cited on p. 54).
- [107] R. Soref, “The past, present, and future of silicon photonics”, *IEEE J. Sel. Top. Quantum Electron.* **12**, 1678–1687 (2006) DOI: [10.1109/JSTQE.2006.883151](https://doi.org/10.1109/JSTQE.2006.883151) (cited on p. 54).
- [108] J. Sun, E. Timurdogan, A. Yaacobi, E. S. Hosseini, and M. R. Watts, “Large-scale nanophotonic phased array”, *Nature* **493**, 195–199 (2013) DOI: [10.1038/nature11727](https://doi.org/10.1038/nature11727) (cited on p. 54).
- [109] A. P. Mosk, A. Lagendijk, G. Lerosey, and M. Fink, “Controlling waves in space and time for imaging and focusing in complex media”, *Nat. Photon.* **6**, 283–292 (2012) DOI: [10.1038/nphoton.2012.88](https://doi.org/10.1038/nphoton.2012.88) (cited on p. 60).
- [110] R. K. Tyson, “Wavefront Correction”, in *Principles of Adaptive Optics*, 3rd ed. (CRC Press, 2010) Chap. 6, pp. 177–196 (cited on p. 61).
- [111] R. Horstmeyer, H. Ruan, and C. Yang, “Guidestar-assisted wavefront-shaping methods for focusing light into biological tissue”, *Nat. Photon.* **9**, 563–571 (2015) DOI: [10.1038/nphoton.2015.140](https://doi.org/10.1038/nphoton.2015.140) (cited on p. 61).
- [112] I. M. Vellekoop, A. Lagendijk, and A. P. Mosk, “Exploiting disorder for perfect focusing”, *Nat. Photon.* **4**, 320–322 (2010) DOI: [10.1038/nphoton.2010.3](https://doi.org/10.1038/nphoton.2010.3) (cited on pp. 61, 64, 66).
- [113] I. M. Vellekoop and C. M. Aegerter, “Scattered light fluorescence microscopy: imaging through turbid layers”, *Opt. Lett.* **35**, 1245–1247 (2010) DOI: [10.1364/OL.35.001245](https://doi.org/10.1364/OL.35.001245) (cited on p. 61).
- [114] E. G. Van Putten, D. Akbulut, J. Bertolotti, W. L. Vos, A. Lagendijk, and A. P. Mosk, “Scattering lens resolves sub-100 nm structures with visible light”, *Phys. Rev. Lett.* **106**, 193905 (2011) DOI: [10.1103/PhysRevLett.106.193905](https://doi.org/10.1103/PhysRevLett.106.193905) (cited on p. 61).
- [115] J.-H. Park, C. Park, H. Yu, J. Park, S. Han, J. Shin, S. H. Ko, K. T. Nam, Y.-H. Cho, and Y. Park, “Subwavelength light focusing using random nanoparticles”, *Nat. Photon.* **7**, 454–458 (2013) DOI: [10.1038/nphoton.2013.95](https://doi.org/10.1038/nphoton.2013.95) (cited on p. 61).
- [116] J. Ryu, M. Jang, T. J. Eom, C. Yang, and E. Chung, “Optical phase conjugation assisted scattering lens: variable focusing and 3D patterning”, *Sci. Rep.* **6**, 23494 (2016) DOI: [10.1038/srep23494](https://doi.org/10.1038/srep23494) (cited on p. 61).
- [117] A. Boniface, M. Mounaix, B. Blochet, R. Piestun, and S. Gigan, “Transmission-matrix-based point-spread-function engineering through a complex medium”, *Optica* **4**, 54–59 (2016) DOI: [10.1364/OPTICA.4.000054](https://doi.org/10.1364/OPTICA.4.000054) (cited on p. 61).

- [118] H. Yu, K. Lee, J. Park, and Y. Park, “Ultrahigh-definition dynamic 3D holographic display by active control of volume speckle fields”, *Nat. Photon.* **11**, 186–192 (2017) DOI: [10.1038/nphoton.2016.272](https://doi.org/10.1038/nphoton.2016.272) (cited on p. 61).
- [119] S. M. Popoff, G. Lerosey, R. Carminati, M. Fink, A. C. Boccara, and S. Gigan, “Measuring the transmission matrix in optics: An approach to the study and control of light propagation in disordered media”, *Phys. Rev. Lett.* **104**, 100601 (2010) DOI: [10.1103/PhysRevLett.104.100601](https://doi.org/10.1103/PhysRevLett.104.100601) (cited on pp. 61, 63, 82).
- [120] Y. Choi, T. D. Yang, C. Fang-Yen, P. Kang, K. J. Lee, R. R. Dasari, M. S. Feld, and W. Choi, “Overcoming the diffraction limit using multiple light scattering in a highly disordered medium”, *Phys. Rev. Lett.* **107**, 023902 (2011) DOI: [10.1103/PhysRevLett.107.023902](https://doi.org/10.1103/PhysRevLett.107.023902) (cited on pp. 61, 67, 74, 82, 83).
- [121] S. M. Popoff, G. Lerosey, M. Fink, A. C. Boccara, and S. Gigan, “Controlling light through optical disordered media: transmission matrix approach”, *New J. Phys.* **13**, 123021 (2011) DOI: [10.1088/1367-2630/13/12/123021](https://doi.org/10.1088/1367-2630/13/12/123021) (cited on p. 61).
- [122] M. Kim, W. Choi, Y. Choi, C. Yoon, and W. Choi, “Transmission matrix of a scattering medium and its applications in biophotonics”, *Opt. Express* **23**, 12648–12668 (2015) DOI: [10.1364/OE.23.012648](https://doi.org/10.1364/OE.23.012648) (cited on p. 61).
- [123] A. Pors, F. Ding, Y. Chen, I. P. Radko, and S. I. Bozhevolnyi, “Random-phase metasurfaces at optical wavelengths”, *Sci. Rep.* **6**, 28448 (2016) DOI: [10.1038/srep28448](https://doi.org/10.1038/srep28448) (cited on p. 62).
- [124] D. D. Battista, D. Ancora, H. Zhang, K. Lemonaki, E. Marakis, E. Liapis, S. Tzortzakis, and G. Zacharakis, “Tailored light sheets through opaque cylindrical lenses”, *Optica* **3**, 1237–1240 (2016) DOI: [10.1364/OPTICA.3.001237](https://doi.org/10.1364/OPTICA.3.001237) (cited on p. 62).
- [125] B. Redding, S. F. Liew, R. Sarma, and H. Cao, “Compact spectrometer based on a disordered photonic chip”, *Nat. Photon.* **7**, 746–751 (2013) DOI: [10.1038/nphoton.2013.190](https://doi.org/10.1038/nphoton.2013.190) (cited on pp. 62, 78).
- [126] H. H. Sheinfux, Y. Lumer, G. Ankonina, A. Z. Genack, G. Bartal, and M. Segev, “Observation of Anderson localization in disordered nanophotonic structures”, *Science* **356**, 953–956 (2017) DOI: [10.1126/science.aah6822](https://doi.org/10.1126/science.aah6822) (cited on p. 62).
- [127] D. Jalas, A. Petrov, M. Eich, W. Freude, S. Fan, Z. Yu, R. Baets, M. Popović, A. Melloni, J. D. Joannopoulos, M. Vanwolleghem, C. R. Doerr, and H. Renner, “What is – and what is not – an optical isolator”, *Nat. Photon.* **7**, 579–582 (2013) DOI: [10.1038/nphoton.2013.185](https://doi.org/10.1038/nphoton.2013.185) (cited on p. 64).
- [128] A. Yariv, “Phase Conjugate Optics and Realtime Holography”, *IEEE J. Quant. Electron.* **14**, 650–660 (1978) DOI: [10.1109/JQE.1978.1069870](https://doi.org/10.1109/JQE.1978.1069870) (cited on p. 64).

- [129] M. D. Levenson, “High-resolution imaging by wave-front conjugation”, *Opt. Lett.* **5**, 182–184 (1980) DOI: [10.1364/ol.5.000182](https://doi.org/10.1364/ol.5.000182) (cited on p. 64).
- [130] D. Akbulut, T. J. Huisman, E. G. V. Putten, and W. L. Vos, “Focusing light through random photonic media by binary amplitude modulation”, *Opt. Express* **19**, 4017–4029 (2011) DOI: [10.1364/OE.19.004017](https://doi.org/10.1364/OE.19.004017) (cited on p. 65).
- [131] A. W. Lohmann, R. G. Dorsch, D. Mendlovic, C. Ferreira, and Z. Zalevsky, “Space–bandwidth product of optical signals and systems”, *J. Opt. Soc. Am. A* **13**, 470–473 (1996) DOI: [10.1364/JOSAA.13.000470](https://doi.org/10.1364/JOSAA.13.000470) (cited on p. 66).
- [132] I. M. Vellekoop and A. P. Mosk, “Focusing coherent light through opaque strongly scattering media”, *Opt. Lett.* **32**, 2309–2311 (2007) DOI: [10.1364/OL.32.002309](https://doi.org/10.1364/OL.32.002309) (cited on pp. 66, 67, 83).
- [133] D. A. B. Miller, “Sorting out light”, *Science* **347**, 1423–1424 (2015) DOI: [10.1126/science.aaa6801](https://doi.org/10.1126/science.aaa6801) (cited on pp. 66, 79).
- [134] Y. Choi, C. Yoon, M. Kim, W. Choi, and W. Choi, “Optical imaging with the use of a scattering lens”, *IEEE J. Sel. Top. Quantum Electron.* **20**, 61–73 (2014) DOI: [10.1109/JSTQE.2013.2275942](https://doi.org/10.1109/JSTQE.2013.2275942) (cited on p. 67).
- [135] J. Park, J.-H. Park, H. Yu, and Y. Park, “Focusing through turbid media by polarization modulation”, *Opt. Lett.* **40**, 1667–1670 (2015) DOI: [10.1364/OL.40.001667](https://doi.org/10.1364/OL.40.001667) (cited on p. 67).
- [136] M. P. Backlund, A. Arbabi, P. N. Petrov, E. Arbabi, S. Saurabh, A. Faraon, and W. E. Moerner, “Removing orientation-induced localization biases in single-molecule microscopy using a broadband metasurface mask”, *Nat. Photon.* **10**, 459–463 (2016) DOI: [10.1038/nphoton.2016.93](https://doi.org/10.1038/nphoton.2016.93) (cited on p. 67).
- [137] M. Khorasaninejad, W. T. Chen, R. C. Devlin, J. Oh, A. Y. Zhu, and F. Capasso, “Metalenses at visible wavelengths: diffraction-limited focusing and subwavelength resolution imaging”, *Science* **352**, 1190–1194 (2016) DOI: [10.1126/science.aaf6644](https://doi.org/10.1126/science.aaf6644) (cited on pp. 67, 78).
- [138] P. Genevet, F. Capasso, F. Aieta, M. Khorasaninejad, and R. Devlin, “Recent advances in planar optics: from plasmonic to dielectric metasurfaces”, *Optica* **4**, 139–152 (2017) DOI: [10.1364/OPTICA.4.000139](https://doi.org/10.1364/OPTICA.4.000139) (cited on p. 67).
- [139] S. Feng, C. Kane, P. A. Lee, and A. D. Stone, “Correlations and fluctuations of coherent wave transmission through disordered media”, *Phys. Rev. Lett.* **61**, 834–837 (1988) DOI: [10.1103/PhysRevLett.61.834](https://doi.org/10.1103/PhysRevLett.61.834) (cited on p. 69).
- [140] S. Schott, J. Bertolotti, J.-F. Léger, L. Bourdieu, and S. Gigan, “Characterization of the angular memory effect of scattered light in biological tissues”, *Opt. Express* **23**, 13505–13516 (2015) DOI: [10.1364/OE.23.013505](https://doi.org/10.1364/OE.23.013505) (cited on p. 69).

- [141] V. Nikolenko, “SLM microscopy: scanless two-photon imaging and photo-stimulation using spatial light modulators”, *Front. Neural Circuits* **2**, 1–14 (2008) DOI: [10.3389/neuro.04.005.2008](https://doi.org/10.3389/neuro.04.005.2008) (cited on p. 77).
- [142] C. K. Kim, A. Adhikari, and K. Deisseroth, “Integration of optogenetics with complementary methodologies in systems neuroscience”, *Nat. Rev. Neurosci.* **18**, 222–235 (2017) DOI: [10.1038/nrn.2017.15](https://doi.org/10.1038/nrn.2017.15) (cited on p. 77).
- [143] J. E. Curtis, B. A. Koss, and D. G. Grier, “Dynamic holographic optical tweezers”, *Opt. Commun.* **217**, 169–175 (2012) DOI: [10.1016/S0030-4018\(02\)01524-9](https://doi.org/10.1016/S0030-4018(02)01524-9) (cited on p. 77).
- [144] R. Bruck, K. Vynck, P. Lalanne, B. Mills, D. J. Thomson, G. Z. Mashanovich, G. T. Reed, and O. L. Muskens, “All-optical spatial light modulator for reconfigurable silicon photonic circuits”, *Optica* **3**, 396–402 (2016) DOI: [10.1364/OPTICA.3.000396](https://doi.org/10.1364/OPTICA.3.000396) (cited on p. 77).
- [145] R. Pappu, B. Recht, J. Taylor, and N. Gershenfeld, “Physical one-way functions”, *Science* **297**, 2026–2030 (2002) DOI: [10.1126/science.1074376](https://doi.org/10.1126/science.1074376) (cited on p. 77).
- [146] A. Arbabi, E. Arbabi, S. M. Kamali, Y. Horie, S. Han, and A. Faraon, “Miniature optical planar camera based on a wide-angle metasurface doublet corrected for monochromatic aberrations”, *Nat. Commun.* **7**, 13682 (2016) DOI: [10.1038/ncomms13682](https://doi.org/10.1038/ncomms13682) (cited on p. 77).
- [147] A. Zhan, S. Colburn, R. Trivedi, T. K. Fryett, C. M. Dodson, and A. Majumdar, “Low-contrast dielectric metasurface optics”, *ACS Photonics* **3**, 209–214 (2016) DOI: [10.1021/acsp Photonics.5b00660](https://doi.org/10.1021/acsp Photonics.5b00660) (cited on p. 78).
- [148] E. Arbabi, A. Arbabi, S. M. Kamali, Y. Horie, and A. Faraon, “Multiwavelength polarization-insensitive lenses based on dielectric metasurfaces with”, *Optica* **3**, 628–633 (2016) DOI: [10.1364/OPTICA.3.000628](https://doi.org/10.1364/OPTICA.3.000628) (cited on p. 78).
- [149] J. S. Ho, B. Qiu, Y. Tanabe, A. J. Yeh, S. Fan, and A. S. Y. Poon, “Planar immersion lens with metasurfaces”, *Phys. Rev. B* **91**, 125145 (2015) DOI: [10.1103/PhysRevB.91.125145](https://doi.org/10.1103/PhysRevB.91.125145) (cited on p. 78).
- [150] E. Ambrose, “A surface contact microscope for the study of cell movements”, *Nature* **178**, 1194 (1956) DOI: [10.1038/1781194a0](https://doi.org/10.1038/1781194a0) (cited on p. 78).
- [151] J. Bertolotti, E. G. van Putten, C. Blum, A. Lagendijk, W. L. Vos, and A. P. Mosk, “Non-invasive imaging through opaque scattering layers”, *Nature* **491**, 232–234 (2012) DOI: [10.1038/nature11578](https://doi.org/10.1038/nature11578) (cited on p. 78).
- [152] O. Katz, P. Heidmann, M. Fink, and S. Gigan, “Non-invasive real-time imaging through scattering layers and around corners via speckle correlations”, *Nat. Photon.* **8**, 784–790 (2014) DOI: [10.1038/nphoton.2014.189](https://doi.org/10.1038/nphoton.2014.189) (cited on p. 78).

- [153] E. Mudry, K. Belkebir, J. Girard, J. Savatier, E. Le Moal, C. Nicoletti, M. Allain, and A. Sentenac, “Structured illumination microscopy using unknown speckle patterns”, *Nat. Photon.* **6**, 312–315 (2012) DOI: [10.1038/nphoton.2012.83](https://doi.org/10.1038/nphoton.2012.83) (cited on p. 78).
- [154] D. Li, L. Shao, B.-C. Chen, X. Zhang, M. Zhang, B. Moses, D. E. Milkie, J. R. Beach, J. A. Hammer, M. Pasham, T. Kirchhausen, M. A. Baird, M. W. Davidson, P. Xu, and E. Betzig, “Extended-resolution structured illumination imaging of endocytic and cytoskeletal dynamics”, *Science* **349**, aab3500 (2015) DOI: [10.1126/science.aab3500](https://doi.org/10.1126/science.aab3500) (cited on p. 78).
- [155] D. A. B. Miller, “All linear optical devices are mode converters”, *Opt. Express* **20**, 23985–23993 (2012) DOI: [10.1364/OE.20.023985](https://doi.org/10.1364/OE.20.023985) (cited on p. 79).
- [156] Z. Yaqoob, D. Psaltis, M. S. Feld, and C. Yang, “Optical phase conjugation for turbidity suppression in biological samples”, *Nat. Photon.* **2**, 110–115 (2008) DOI: [10.1038/nphoton.2007.297](https://doi.org/10.1038/nphoton.2007.297) (cited on p. 82).
- [157] J. Yoon, K. Lee, J. Park, and Y. Park, “Measuring optical transmission matrices by wavefront shaping”, *Opt. Express* **23**, 10158–10167 (2015) DOI: [10.1364/OE.23.010158](https://doi.org/10.1364/OE.23.010158) (cited on p. 83).
- [158] M. D. Henry, S. Walavalkar, A. Homyk, and A. Scherer, “Alumina etch masks for fabrication of high-aspect-ratio silicon micropillars and nanopillars”, *Nanotechnology* **20**, 255305 (2009) DOI: [10.1088/0957-4484/20/25/255305](https://doi.org/10.1088/0957-4484/20/25/255305) (cited on pp. 102, 103).
- [159] M. D. Henry, “ICP etching of silicon for micro and nanoscale devices”, Ph.D. Thesis (California Institute of Technology, 2010) (cited on p. 102).
- [160] C. C. Welch, A. L. Goodyear, T. Wahlbrink, M. C. Lemme, and T. Mollenhauer, “Silicon etch process options for micro- and nanotechnology using inductively coupled plasmas”, *Microelectron. Eng.* **83**, 1170–1173 (2006) DOI: [10.1016/j.mee.2006.01.079](https://doi.org/10.1016/j.mee.2006.01.079) (cited on p. 102).

FABRICATION

A.1 Lab Procedure

The devices presented in this thesis shares the fabrication recipes and the procedure are enumerated in each chapter. In thi appendix section, we will describe the detailed procedure in each step.

Silicon Subwavelength Grating Reflector Fabrication

This fabrication recipe is used for the double SWG filters (Chapter 1) and the silicon active antenna (Chapter 4). The process mainly consists of patterning a resist with an electron beam lithography (EBL) and dry etching of the silicon layer using Pseudo-Bosch etch termed by Henry *et al.* [158, 159] at Caltech. The Pseudo-Bosch etch involves a mixture of SF₆ and C₄F₈, which simultaneously etches the horizontal surface and passivates the vertical sidewalls, respectively, and thus enables high-aspect ratio structure with smooth sidewalls and controllable sidewall angles [160].

- (a) The diced chips typically with <1 cm in side width are cleaned with Nano-Strip (Cyantek, stabilized formulation of H₂SO₄ and H₂O₂), followed by acetone, methanol, isopropyl alcohol (IPA), and rinsing with deionized water (DI water).
- (b) After dehydrating the chip (180°C, 5 min), a positive electron beam resist of ZEP520A[†] (Zeon Chemicals) is spun onto the chip (5000 rpm, 60 sec), and then baked (180°C, 3 min), resulting in ~300 nm-thick resist. If the substrate is a fused silica, to avoid charging effects, a charge dissipation polymer, AquaSAVE (Mitsubishi Rayon) is spun on the resist (2000 rpm, 60 sec) , and then baked (70°C, 5 min).
- (c) The SWG mask pattern (line & space pattern) is defined by EBL using a 100 kV electron beam (EBPG5000+ or EBPG5200, Raith).

[†]We find that hydrogen-terminated silicon (Si-H) surface makes the adhesion of an electron beam resist, ZEP520A worse. Hydroxyl-terminated silicon (Si-OH) surface is formed due to a very thin layer of oxide (<1 nm) during the Nano-Strip cleaning process, making the adhesion better.

- (d) AquaSAVE is removed by dissolving it in DI water. The patterns are developed using ZED-N50 (Zeon Chemicals) (150 sec) and rinsed with methyl isobutyl ketone (MIBK) (30 sec).
- (e) The pattern in ZEP520A is transferred into the silicon layer by inductively coupled plasma reactive ion etching (ICP-RIE) process using $\text{SF}_6/\text{C}_4\text{F}_8$ mixed plasma chemistry (Pseudo-Bosch etch).
- (f) Remover PG (MicroChem) is used to strip the residual resist layer (80°C, a few hours).

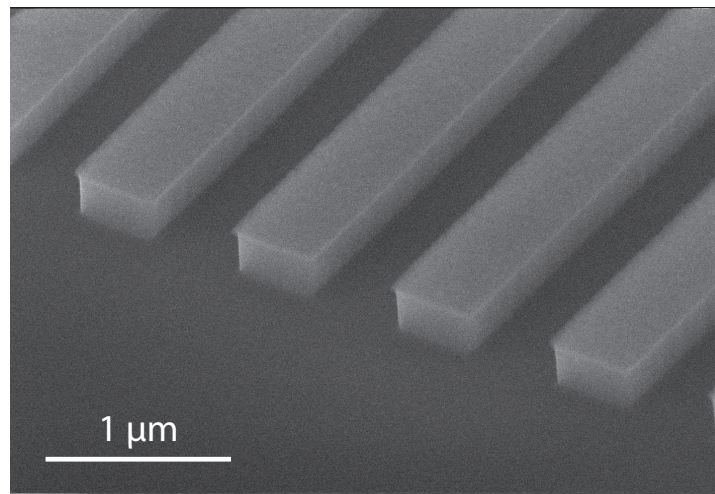


Figure A.1: **SEM image of a subwavelength grating reflector.**

Silicon/Silicon Nitride Metasurface Fabrication

This fabrication recipe is used for the silicon metasurface fabrication (Chapter 1). The process mainly consists of patterning a resist with an EBL, transferring the pattern into a hard mask of Al_2O_3 by means of a lift-off, and dry etching of the silicon (or SiN_x) layer using Pseudo-Bosch etch. Al_2O_3 hard mask shows a substantial selectivity, typically >1000 [158], with respect to silicon when used in the Pseudo-Bosch etch.

- (a) The diced fused silica chips are cleaned with Nano-Strip, followed by acetone, methanol, IPA, and rinsing with DI water.
- (b) After dehydrating the chip (180°C, 5 min), a positive electron beam resist of ZEP520A is spun onto the chip (5000 rpm, 60 sec), and then baked (180°C,

3 min), resulting in ~ 300 nm-thick resist. To avoid charging effects, a charge dissipation polymer, AquaSAVE is spun on the resist (2000 rpm, 60 sec) , and then baked (70°C , 5 min).

- (c) The metasurface mask pattern (2-D array of rectangles) is defined by EBL.
- (d) AquaSAVE is removed by dissolving it in DI water. The patterns are developed using ZED-N50 (150 sec) and rised with MIBK (30 sec).
- (e) 80 nm-thick Al_2O_3 is deposited by electron beam evaporation and the pattern is transferred into Al_2O_3 layer by a lift-off technique, by stripping ZEP520A in Remover PG (80°C , a few hours). Subsequently, cleaning with Nano-Strip ensures the removal of any residual resist.
- (f) The amorphous silicon (α -Si) layer or SiN_x layer is patterned by ICP-RIE process using Pseudo-Bosch etch, where Al_2O_3 serves as a hard mask.
- (g) Finally, Al_2O_3 hard mask is selectively etched by a mixture of NH_4OH and H_2O_2 at 80°C .

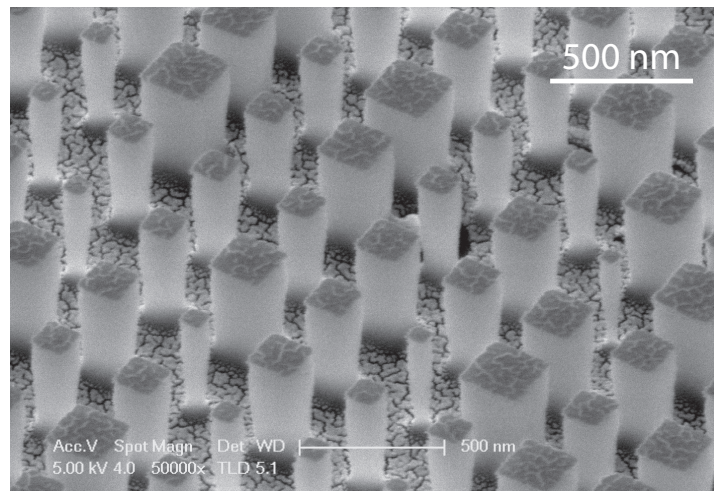


Figure A.2: **SEM image of a silicon nitride disordered metasurface.** A thin Au layer is deposited for anti-charging purpose.

A.2 Optical Properties of Materials

It is important to characterize the refractive indices of the materials. We measured complex refractive indices by means of ellipsometry. The complex refractive index

of α -Si is plotted in Fig. A.3(a,b). The measured refractive index of silicon dioxide (SiO_2) as shown in Fig. A.3(c) is fitted well with Sellmeier equation:

$$n^2(\lambda) = \epsilon + \frac{A\lambda^2}{\lambda^2 - B^2} - E\lambda^2, \quad (\text{A.1})$$

where $\epsilon = 1.870$, $A = 0.34$, $B = 0.16$ (μm^2), and $E = 0.01382$ (μm^{-2}). The measured refractive index of SiN_x as shown in Fig. A.3(d)) is fitted well with Cauchy's equation:

$$n(\lambda) = A + \frac{B}{\lambda^2} + \frac{C}{\lambda^4}, \quad (\text{A.2})$$

where $A = 1.868$, $B = 0.0879$ (μm^2), and $C = -0.00492$ (μm^4).

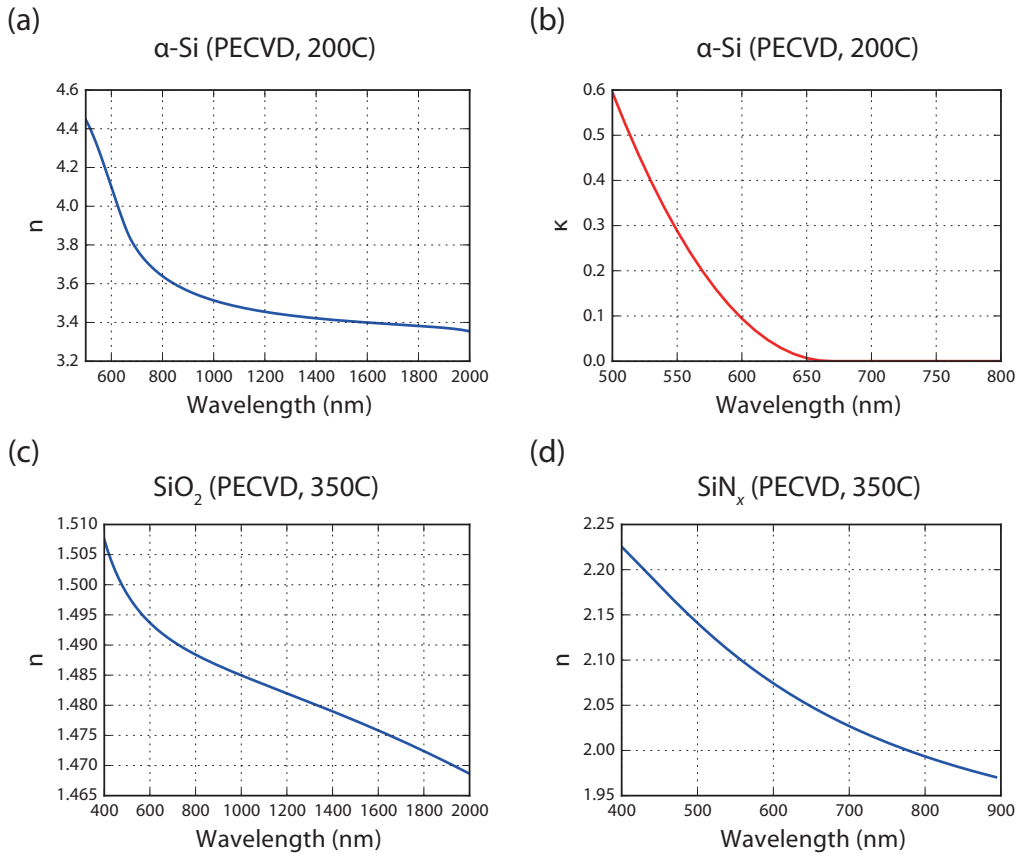


Figure A.3: **Measured refractive indices by ellipsometry.** (a) Refractive index of α -Si grown with PECVD at 200°C. (b) Extinction coefficient of α -Si grown with PECVD at 200°C. (c) Refractive index of SiO_2 grown with PECVD at 350°C. (d) Refractive index of SiN_x grown with PECVD at 350°C. All the films are grown using the KNI standard recipe.